

AD-A071 094

HONEYWELL ELECTRO-OPTICS CENTER LEXINGTON MA
MINORITY CARRIER LIFETIME AND DIFFUSION LENGTH IN P-TYPE MERCUR--ETC(U)
FEB 79 J L SCHMIT, S P TOBIN, T J TREDWELL

F/G 20/12

F33615-77-C-5142

UNCLASSIFIED

AFML -TR-79-4036

NL

1 of 2

AD
A071094



AD A071094

LEVEL

11

AFML-TR-79-4036

MINORITY CARRIER LIFETIME AND DIFFUSION LENGTH
IN P-TYPE MERCURY CADMIUM TELLURIDE

Joseph L. Schmit
Honeywell, Inc.
Corporate Material Sciences Center
Bloomington, Minnesota 55420

and

Stephen P. Tobin and Timothy J. Tredwell
Honeywell, Inc.
Electro-Optics Center
Lexington, Massachusetts 02173

February 1979

Technical Report AFML-TR-79-4036 for period
August 1977 - January 1979

Approved for public release; distribution unlimited.

AIR FORCE MATERIALS LABORATORY
AIR FORCE WRIGHT AERONAUTICAL LABORATORIES
AIR FORCE SYSTEMS COMMAND
WRIGHT-PATTERSON AIR FORCE BASE, OHIO 45433

DDC
RECEIVED
JUL 12 1979
RECEIVED
C

DDC FILE COPY

79 07 11 054

NOTICE

When Government drawings, specifications, or other data are used for any purpose other than in connection with a definitely related Government procurement operation, the United States Government thereby incurs no responsibility nor any obligation whatsoever; and the fact that the government may have formulated, furnished, or in any way supplied the said drawings, specifications, or other data, is not to be regarded by implication or otherwise as in any manner licensing the holder or any other person or corporation, or conveying any rights or permission to manufacture, use, or sell any patented invention that may in any way be related thereto.

This report has been reviewed by the Information Office (IO) and is releasable to the National Technical Information Service (NTIS). At NTIS, it will be available to the general public, including foreign nations.

This technical report has been reviewed and is approved for publication.

ROBERT L. HICKMOTT, Project Engineer
Laser and Optical Materials Branch
Electromagnetic Materials Division
Air Force Materials Laboratory

FOR THE COMMANDER

WILLIAM G. D. FREDERICK, Chief
Laser and Optical Materials Branch
Electromagnetic Materials Division
Air Force Materials Laboratory

"If your address has changed, if you wish to be removed from our mailing list, or if the addressee is no longer employed by your organization please notify AFML/LOP, W-PAFB, OH 45433 to help us maintain a current mailing list."

Copies of this report should not be returned unless return is required by security considerations, contractual obligations, or notice on a specific document.

UNCLASSIFIED

SECURITY CLASSIFICATION OF THIS PAGE (WHEN DATA ENTERED)

REPORT DOCUMENTATION PAGE		READ INSTRUCTIONS BEFORE COMPLETING FORM
1. REPORT NUMBER AFML TR-79-4036	2. GOV'T ACCESSION NUMBER	3. RECIPIENT'S CATALOG NUMBER 9
4. TITLE (AND SUBTITLE) MINORITY CARRIER LIFETIME AND DIFFUSION LENGTH IN P-TYPE MERCURY CADMIUM TELLURIDE	5. TYPE OF REPORT, PERIOD COVERED Final Technical Report, August 77 - January 79	
6. AUTHOR(S) Joseph L./Schmit, Stephen P./Tobin and Timothy J./Tredwell		7. PERFORMING ORG. REPORT NUMBER
8. CONTRACT OR GRANT NUMBER(S) F33615-77-C-5142		9. PROGRAM ELEMENT, PROJECT, TASK AREA & WORK UNIT NUMBERS Program Element: 62102F Project/Task/Work Unit: 2423/01/08
10. CONTROLLING OFFICE NAME/ADDRESS AIR FORCE MATERIALS LABORATORY (LPO) Air Force Systems Command Wright-Patterson Air Force Base, Ohio 45433		11. REPORT DATE February 1979
12. MONITORING AGENCY NAME/ADDRESS (IF DIFFERENT FROM CONT. OFF.) 1253p.		13. NUMBER OF PAGES 137
14. DISTRIBUTION STATEMENT (OF THIS REPORT) Approved for public release; distribution unlimited		15. SECURITY CLASSIFICATION (OF THIS REPORT) UNCLASSIFIED
16. DISTRIBUTION STATEMENT (OF THE ABSTRACT ENTERED IN BLOCK 20, IF DIFFERENT FROM REPORT)		
17. SUPPLEMENTARY NOTES		
18. KEY WORDS (CONTINUE ON REVERSE SIDE IF NECESSARY AND IDENTIFY BY BLOCK NUMBER) Mercury-Cadmium Telluride R _A Photovoltaic Detector Lifetime Diffusion length		
19. ABSTRACT (CONTINUE ON REVERSE SIDE IF NECESSARY AND IDENTIFY BY BLOCK NUMBER) This report covers a study of the relationship between minority carrier properties, τ_e , L_e and μ_e and majority carrier hole, and acceptor concentrations in p-type Hg _{0.61} Cd _{0.39} Te. This report documents the following conclusions: The dominant recombination mechanism is Shockley-Read not radiative. The recombination center is at 140 meV above the valence band edge and has a concentration proportional to the acceptor concentration. Minority carrier lifetime is proportional to N_A^{-1} and the diffusion length is proportional to $N_A^{-1/2}$ below 200K. Both τ_e and L_e are uniform to ± 10 percent. The		

DD FORM
1 JAN 73

1473

EDITION OF 1 NOV 55 IS OBSOLETE

UNCLASSIFIED

SECURITY CLASSIFICATION OF THIS PAGE (WHEN DATA ENTERED)

393 776

LB

HD-168 REV 11/74

UNCLASSIFIED

SECURITY CLASSIFICATION OF THIS PAGE (WHEN DATA ENTERED)

Block 20

electron mobility in p-type $\text{Hg}_{0.61}\text{Cd}_{0.39}\text{Te}$ equals the electron mobility in n-type within experimental error. The R_0A product at 193K is proportional to $(N_A - N_D)^{1/2}$ up to at least $2 \times 10^{16} \text{ cm}^{-3}$. Diode reverse recovery and EBIC line scans are reliable means of measuring τ_e and L_e .

SECURITY CLASSIFICATION OF THIS PAGE (WHEN DATA ENTERED)

FOREWORD

This report covers the first 17 months of contract F33615-77-C-5142 under the guidance of Robert L. Hickmott of AFML. The work was shared between the Honeywell Corporate Material Sciences Center and the Honeywell Electro Optics Center. The authors acknowledge the support of many people at both locations.

At CMSC, the samples were prepared and density measured by R. Camp. J. Lindberg made the Hall measurements and J. Holman sputtered the Cu layers. We thank Dr. M. W. Scott for his continued support and inspiration, and Dr. J. Bowers for the dedicated work in developing the LPE system late in the contract.

At HEOC during the course of this program, many MIS samples, photodiodes and Backside Illuminated Tapered Structures (BITS) were fabricated and characterized. The authors acknowledge the help of C. Bryant B. Pierson L. Kelley, B. Denley, and L. Gauthier in fabricating these devices and the help of R. McDonald, J. Nevin, K. Locke, M. Volland, and E. Henry in the characterization of these devices. The technical contributions of Dr. A. K. Sood, Dr. M. B. Reine, and D. L. Polla at EOC are also acknowledged.

Accession For	
NTIS GRA&I	<input checked="checked" type="checkbox"/>
DDC TAB	<input type="checkbox"/>
Unannounced	<input type="checkbox"/>
Justification	
By _____	
Distribution/	
Availability Codes	
Dist	Avail and/or special
A	

TABLE OF CONTENTS

Section	Page
1 INTRODUCTION	1
2 THEORY OF (Hg, Cd)Te PHOTODIODES	2
2.1 Analytical Photodiode Model	2
2.2 Minority Carrier Lifetime Mechanisms	6
2.2.1 Auger Recombination	8
2.2.2 Radiative Recombination	10
2.2.3 Shockley-Read Recombination	11
3 MATERIAL PREPARATION	15
3.1 Bulk Crystal Growth	15
3.2 Crystal Annealing	16
3.3 Liquid Phase Epitaxy Growth	18
4 DEVICE FABRICATION	20
4.1 MIS Sample Fabrication	20
4.2 Photodiode Fabrication	22
4.3 BITS Fabrication	24
5 MEASUREMENT METHODS	29
5.1 Determination of Carrier Concentration Using Hall Measurements	29
5.1.1 Electrical Contacts	29
5.1.2 Hall System	30
5.1.3 Determination of Carrier Concentration	30
5.1.4 Mobility Ratio	34
5.2 Determination of Alloy Composition	37
5.2.1 Composition Determination by Density Measurement	37
5.2.2 Composition Determination by Fluorescence	38
5.2.3 Composition Determination by Spectral Cutoff	38
5.3 MIS Determination of Bulk Properties	39
5.3.1 Majority Carrier Type	39
5.3.2 Bulk Carrier Concentration	39
5.3.3 Bulk Composition	42

TABLE OF CONTENTS (Continued)

Section	Page
5.4 Reverse Recovery Technique	43
5.4.1 Qualitative Description Technique	43
5.4.2 Experimental Apparatus	47
5.4.3 Interpretation of Data	47
5.4.4 Injected Carrier Density	53
5.5 R_oA Versus Temperature Measurement	54
5.6 EBIC Technique	55
5.7 The Backside-Illuminated Tapered Structure (BITS)	57
6 RESULTS	60
6.1 Carrier Concentration	60
6.2 Minority Carrier Lifetime	61
6.2.1 Lifetime versus Temperature	64
6.2.2 Lifetime versus Carrier Concentration	64
6.2.3 Lifetime versus Excess Carrier Density	77
6.2.4 Lifetime Uniformity	81
6.3 Diffusion Length Results	84
6.3.1 BITS Results	84
6.3.2 Diffusion Length versus Temperature	91
6.3.3 Diffusion Length versus Carrier Concentration	91
6.3.4 Uniformity of Diffusion Length	95
6.4 Minority Carrier Mobility	97
6.5 R_oA	102
6.5.1 R_oA versus Temperature	102
6.5.2 R_oA versus Carrier Concentration	107
6.5.3 R_oA Uniformity	107
7 ANALYSIS	109
7.1 Shockley-Read Recombination Analysis	109
7.1.1 Assumptions of the Model	109
7.1.2 Fitting the Data	110
7.1.3 Nature of the Defect	111

TABLE OF CONTENTS (Concluded)

Section	Page
7.2 Correlation of Measured Parameters	114
7.3 Limitations of Measurement Methods	118
7.3.1 Diode Reverse Recovery Technique	119
7.3.2 EBIC Line Scan Technique	122
7.4 Comparison with Results for Other $\text{Hg}_{1-x}\text{Cd}_x\text{Te}$	124
7.4.1 Shockley-Read versus Radiative	124
7.4.2 Energy Level of S-R Defect	124
7.4.3 Other Dopants	128
8 CONCLUSIONS AND RECOMMENDATIONS FOR DEVICE DESIGN AND FUTURE WORK	129
8.1 Conclusions	129
8.2 Recommendations for Device Design and Future Work	130
APPENDIX A METHODS FOR EXTRACTING LIFE TIME FROM REVERSE RECOVERY DATA	133
REFERENCES	135

LIST OF ILLUSTRATIONS

<u>Figure</u>		<u>Page</u>
1	Sources of Noise in Photodiodes	7
2	MIS Structure Configuration	20
3	Photodiode Fabrication	23
4	BITS Fabrication	25
5	Typical Hall Coefficient versus Reciprocal Temperature	32
6	Temperature Dependence of the Mobility of n- and p-Type Samples	35
7	Temperature Dependence of the Mobility Ratio	36
8	Ideal MIS Capacitance-Voltage Curves for a p-Type Semiconductor	40
9	MIS Spectral Measurement Setup	44
10	Typical Spectral Response Curve Using MIS	45
11	Schematic of Diode Reverse Recovery Technique	46
12	Reverse Recovery Circuit	48
13	Kuno Plot for Reverse Recovery Data at 126K	52
14	The Backside-Illuminated Tapered Structure (BITS)	58
15	Minority Carrier Lifetime versus Reciprocal Temperature	65
16	Lifetime by Kingston Method, Sample 2	66
17	Lifetime by Kingston Method, Sample 8	67
18	Dependence of Minority Carrier Lifetime at 295K on Hole Concentration	69
19	Dependence of Minority Carrier Lifetime at 193K on Hole Concentration	70
20	Dependence of Minority Carrier Lifetime at 77K on Hole Concentration	71
21	Dependence of Minority Carrier Lifetime at 77K on Acceptor Concentration	74
22	Dependence of Minority Carrier Lifetime at 193K on Acceptor Concentration	75

LIST OF ILLUSTRATIONS (Continued)

<u>Figure</u>		<u>Page</u>
23	Dependence of Minority Carrier Lifetime at 295K on Acceptor Concentration	76
24	Minority Carrier Lifetime as a Function of Carrier Injection Level; Data Compared to Auger and Radiative Theories	78
25	Minority Carrier Lifetime as a Function of Carrier Injection Level; Data of Figure 24 Compared to Shockley-Read Theory	80
26	Minority Carrier Lifetime by Kuno's Method as a Function of Injected Carrier Density	82
27	Lifetime as a Function of Position for Sample 2 at 193K	83
28	Lifetime as a Function of Position for Sample 3 at 193K	84
29	Lifetime as a Function of Position for Sample 8 at 193K	85
30	Thickness Dependence of Signal Current for a 4- μ m Cutoff BITS Array at 200K	86
31	Thickness Dependence of Signal Current for a 4- μ m Cutoff BITS Array at 77K	87
32	Thickness Dependence of Signal Current for BITS Array Number 6 From Sample 7 at 175K	89
33	The Data of Figure 32 Corrected for Background Level	90
34	Temperature Dependence of Minority Carrier Diffusion Length, L_e , for Sample 2	92
35	Temperature Dependence of L_e for Sample 3	93
36	Temperature Dependence of L_e for Sample 6	94
37	Dependence of L_e on Hole Concentration	96
38	Diffusion Length versus Position for Sample 2 at 80K	98
39	Temperature Dependence of Electron Mobility in n-Type $Hg_{1-x}Cd_xTe$ and p-Type Sample 2	99
40	Temperature Dependence of Electron Mobility in n-Type $Hg_{1-x}Cd_xTe$ and p-Type Sample 3	101
41	Temperature Dependence of $R_o A$ for Sample 3	103

LIST OF ILLUSTRATIONS (Concluded)

<u>Figure</u>		<u>Page</u>
42	Temperature Dependence of $R_o A$ for Sample 2	104
43	Temperature Dependence of $R_o A$ for Sample 7	105
44	Temperature Dependence of $R_o A$ for Sample 8	106
45	$R_o A$ at 193K as a Function of Hole Concentration	108
46	Schematic of the Energy Levels of $Hg_{0.61}Cd_{0.39}Te$ at 200K	113
47	Temperature Dependence of $R_o A$ of Sample 2 Compared to Diffusion-Limited $R_o A$ Calculated From τ_e and L_e	116
48	Temperature Dependence of $R_o A$ of Sample 3	117
49	Temperature Dependence of Minority Carrier Lifetime of a Sample of $Hg_{0.674}Cd_{0.326}Te$ by Kingston's and Kuno's Methods	125
50	Deep Level Transient Spectroscopy (DLTS) Signal as a Function of Temperature for a Sample From Crystal 20475	126
51	Schematic of the DLTS Energy Levels in the Bandgap of Crystal 20475	127

LIST OF TABLES

<u>Table</u>		<u>Page</u>
1	Calculated Lifetimes in $\text{Hg}_{0.6}\text{Cd}_{0.4}\text{Te}$	2
2	Acceptor Concentration as a Function of Annealing Temperature	17
3	Mobility Ratio for $\text{Hg}_{0.6}\text{Cd}_{0.4}\text{Te}$	34
4	Lifetime by Three Methods	51
5	Hole and Acceptor Concentrations of the Samples Used for Diodes	62
6	Summary of Diode Arrays	63
7	Interarray Uniformity of Measured Diffusion Length at 80 and 295K	97
A1	Lifetime From Diode Reverse Recovery	134

LIST OF SYMBOLS

<u>Symbol</u>	<u>Units</u>	<u>Meaning</u>
A	cm ²	Area of Detector
B	cm ³ sec ⁻¹	Carrier Capture Probability (Radiative)
b	-	Mobility Ratio, μ_e/μ_h
b _n	cm	Distance from Junction to n-side Space Charge Layer
b _p	cm	Distance from Junction to p-side Space Charge Layer
c	cm/sec	Speed of Light (3×10^{10})
C	F	Capacitance
C _f	F	High Frequency Capacitance in Inversion
C _{FB}	F	Flat-band Capacitance
C _i	F	Insulator Capacitance
d	cm	Thickness
D* _λ	cm $\sqrt{\text{Hz/watt}}$	Detectivity of a Detector
E _c	eV	Energy of Conduction Band Edge
E _F	eV	Fermi Energy
E _g	eV	Energy Gap
E _t	eV	Energy of S-R Recombination Level
E _v	eV	Energy of Valence Band Edge
Δf	sec ⁻¹	Noise Equivalent Bandwidth
F ₁ F ₂	-	Overlap Integrals
G _{ee}	cm ⁻³ sec ⁻¹	Generation Rate for Electron-Electron Auger Processes
G _{hh}	cm ⁻³ sec ⁻¹	Generation Rate for Hole-Hole Auger Processes
h	Joule-sec	Planck's Constant (6.63×10^{-34})
Hz	sec ⁻¹	Frequency
I _D	amp	Zero-Background Diode Current
i _f	amp	1/f Noise Current
I _F	amp	Diode Forward Current

<u>Symbol</u>	<u>Units</u>	<u>Meaning</u>
i_n	amp	RMS Noise Current in Bandwidth Δf
I_R	amp	Diode Reverse Current
I_{SAT}	amp	Diode Reverse Saturation Current
I_{sig}	amp	Signal-Generated Current
k	J/K	Boltzmann Constant (1.38×10^{-23})
K	degree Kelvin	Absolute Temperature
L_e	cm	Electron (Minority Carrier) Diffusion Length
L_h	cm	Hole (Minority Carrier) Diffusion Length
L_{opt}	cm	Optical Absorption Depth for 90 percent Absorption
m_e^*	g	Electron Effective Mass
m_h^*	g	Hole Effective Mass
m_o	g	Mass of Electron (9.11×10^{-28})
Δn	cm^{-3}	Concentration of Excess Electrons
n	cm^{-3}	Concentration of Electrons in Conduction Band
N_A	cm^{-3}	Acceptor Concentration
N_B	cm^{-3}	Bulk Carrier Concentration
N_C	cm^{-3}	Conduction Band Density of States
N_D	cm^{-3}	Donor Concentration
n_i	cm^{-3}	Intrinsic Carrier Concentration
n_o	cm^{-3}	Equilibrium Concentration of Electrons
n_p	cm^{-3}	Electron Concentration on p-side of Junction
N_t	cm^{-3}	Density of S-R Recombination Centers
N_v	cm^{-3}	Valence Band Density of States
p	cm^{-3}	Concentration of Holes in the Valence Band
p_o	cm^{-3}	Equilibrium Concentration of Holes
p_p	cm^{-3}	Hole Concentration on p-side of Junction
q	coul	Electronic Charge
r	-	Scattering Coefficient
R_D	ohm	Diode Dynamic Resistance
R_H	$cm^3/coul$	Hall Coefficient

<u>Symbol</u>	<u>Units</u>	<u>Meaning</u>
R_i	amp/watt	Current Responsivity of a Detector
R_o	ohm	Diode Zero-Bias Resistance
R_r	$\text{cm}^{-3} \text{sec}^{-1}$	Radiative Recombination Rate
s	cm sec^{-1}	Surface Recombination Velocity
T	$^{\circ}\text{K}$	Temperature
t	sec	Time
t_s	sec	Diode Storage Time
V_{bi}	volt	Junction Built-in Voltage
v_{th}	cm/sec	Carrier Thermal Velocity
W	cm	Junction Depletion Layer Width
W_m	cm	Maximum Depletion Width
x	-	Fraction of CdTe in $\text{Hg}_{1-x}\text{Cd}_x\text{Te}$
z	cm	Lateral Distance from Junction Edge
α	cm^{-1}	Optical Absorption Coefficient
β	-	Ratio of Hole-Hole to Electron-Electron Recombination
ϵ_i	F/cm	Insulator Dielectric Constant
ϵ_o	F/cm	Permittivity of Free Space (8.864×10^{-14})
ϵ_s	F/cm	Semiconductor Dielectric Constant
ϵ_{∞}	F/cm	Optical Frequency Dielectric Constant
η	-	Quantum Efficiency of Detector
λ	μm	Wavelength
λ_{co}	μm	Cutoff Wavelength
μ	-	Effective Mass Ratio, Electrons to Holes
μ_e	$\text{cm}^2 \text{V}^{-1} \text{sec}^{-1}$	Electron Mobility
μ_h	$\text{cm}^2 \text{V}^{-1} \text{sec}^{-1}$	Hole Mobility
$\sigma_{n,p}$	cm^2	Capture Cross-Section for Electrons, Holes
τ_A	sec	Auger Lifetime
τ_{Ai}	sec	Auger Lifetime in Intrinsic Material

<u>Symbol</u>	<u>Units</u>	<u>Meaning</u>
τ_e	sec	Electron (Minority Carrier) Lifetime on p-side
τ_h	sec	Hole (Minority Carrier) Lifetime on n-side
τ_{no}	sec	Lifetime for Electrons in Heavily p-type material
τ_{po}	sec	Lifetime for Holes in Heavily n-type material
τ_r	sec	Radiative Lifetime
τ_R	sec	Reverse Current Time Constant
τ_{S-R}	sec	Shockley-Read Lifetime
ϕ_B	$\text{cm}^{-2} \text{sec}^{-1}$	Background Radiation Flux

SECTION 1 INTRODUCTION

Prior to this contract, lifetime data was available on a variety of samples of $\text{Hg}_{1-x}\text{Cd}_x\text{Te}$. However, since composition ranged from $x = 0.2$ to 0.4 , measurement temperature varied from 77 to 300K , and diodes were prepared by a variety of techniques, it was not possible to correlate the data and determine the dependence of lifetime on any given parameter. The primary thrust of this contract was to determine the dependence of minority carrier lifetime in p-type $\text{Hg}_{0.6}\text{Cd}_{0.4}\text{Te}$ on carrier concentration. In order to eliminate unknown side effects, most of the samples were taken from one crystal grown under our previous contract. The hole concentration was varied by annealing under Hg pressure and by diffusing-in Cu. The composition was determined on the bulk samples by density and on finished MIS and diode devices by measurement of the cutoff wave length. Minority carrier lifetime was determined primarily by diode reverse recovery and verified by BITS measurements. The minority carrier diffusion length was determined primarily by EBIC measurements.

The models used to treat photodiodes and minority carrier lifetime are described in Section 2. The growth and annealing methods used to prepare samples are covered in Section 3. The techniques used to fabricate MIS, PV, and BITS samples are described in Section 4. Measurement techniques used to determine carrier concentration, alloy composition lifetime, diffusion length and R_0A are described in Section 5. Results of our measurements of carrier concentration, lifetime, diffusion length, mobility, and R_0A are given in Section 6. The analysis of these results is given in Section 7. Finally, our conclusions and recommendations for device design and further research appear in Section 8.

SECTION 2

THEORY OF (Hg, Cd)Te PHOTODIODES

2.1 ANALYTICAL PHOTODIODE MODEL

In this subsection, the theory of p-n junction photodiodes in defect-free (Hg, Cd)Te is reviewed. The parameters used to characterize detector performance are quantitatively related to the minority carrier properties in the material.

The detectivity D_{λ}^* of a detector is given by

$$D_{\lambda}^* = \frac{\sqrt{R_i} A \Delta f}{i_n} \quad (1)$$

where R_i is the current responsivity, A is the optically active area, Δf is the noise equivalent bandwidth, and i_n is the rms noise current in the bandwidth Δf .

The current responsivity R_i for a photodiode is given by

$$R_i = \frac{\lambda}{hc} \eta q \quad (2)$$

where h is Planck's constant, c is the speed of light, q is the electron charge and η is the quantum efficiency.

The noise sources associated with a photodiode are shot noise due to background current, Johnson noise and shot noise due to thermal generation, and $1/f$ noise i_f

$$i_n^2 / \Delta f = 4kT/R_D + 2q I_D + 2\eta q^2 \phi_B A + i_f^2 / \Delta f \quad (3)$$

where ϕ_B is the background flux, R_D the diode dynamic resistance and I_D the zero-background diode current. For a photodiode at zero bias voltage, and for which the background noise is negligible, D_λ^* is given by:

$$D_\lambda^* = \frac{\lambda q \eta}{hc} \sqrt{\frac{R_o A}{4kT}} \quad (4)$$

There are two well-known current mechanisms which contribute to $R_o A$. These are generation-recombination current and diffusion current. If there are no contacts or surfaces within a diffusion length of the diode, the $R_o A$ product due to diffusion current can be written as:

$$(R_o A)^{-1} = \left[\frac{n_i^2}{N_A} \sqrt{\frac{\mu_e}{\tau_e}} + \frac{n_i^2}{N_D} \sqrt{\frac{\mu_h}{\tau_h}} \right] q \sqrt{\frac{q}{kT}} \quad (5)$$

where:

- n_i = intrinsic carrier concentration
- μ_e, μ_h = electron and hole (minority carrier) mobility
- τ_e, τ_h = electron and hole (minority carrier) lifetime
- N_A, N_D = dopant concentrations on p and n sides (acceptor and donor concentrations)

Diffusion current is due to the diffusion of thermally generated minority carriers from the n and p sides of the semi-conductor to the depletion layer at the p-n interface. The volume of semiconductor which contributes to diffusion current is given by the diode area times the diffusion length for a minority carrier. The minority carrier diffusion length is given by:

$$L_D = \sqrt{\frac{kT}{q} \mu \tau_e} \quad (6)$$

The volume of semiconductor required to generate the signal is the diode area times the optical absorption depth required to absorb 90 percent of the incoming radiation:

$$L_{\text{opt}} = 2.5/\alpha \quad (7)$$

where α is the absorption coefficient, typically $5 \times 10^3 \text{ cm}^{-1}$. Thus, $L_{\text{opt}} \approx 5$ micrometers. In most cases, the minority carrier diffusion lengths are longer than 5 micrometers; thus, a substantial volume of the semiconductor is contributing noise without contributing signal.

It is possible to shrink the effective semiconductor volume to the volume necessary for signal collection by using "reflective" contacts⁽¹⁻³⁾. The use of heavily doped p^+ and n^+ regions in back of the p and n regions creates a space-charge barrier to minority carrier diffusion and reduces minority carrier density in the heavily doped regions. The R_0A for the case where reflective contacts are used is given by:

$$(R_0A)^{-1} = q \sqrt{\frac{q}{kT}} \left[\frac{n_i^2}{N_A} \sqrt{\frac{\mu_e}{\tau_e}} \tanh\left(\frac{b_p}{L_e}\right) + \frac{n_i^2}{N_D} \sqrt{\frac{\mu_h}{\tau_h}} \tanh\left(\frac{b_n}{L_p}\right) \right] \quad (8)$$

where b_p and b_n are the distances from the junction to the p - and n -side spacecharge barriers.

1. D. Long "Photovoltaic and Photoconductive Infrared Detectors " in Topics in Applied Physics, Volume 19: Optical and Infrared Detectors, pp. 101-147 (Springer-Verlag, Berlin Heidelberg, 1977); the p^+ - P backside contact is discussed on pp. 110-112.
2. "Detection of Long Wavelength Infrared at Moderate Temperatures, " Final technical report, NASA Johnson Space Center Contract NAS9-14180, Mod. 5S, April 1977, in particular, see Section 2.3.
3. D. Long, T. J. Tredwell and J. R. Woodfill, "Detectivity vs Temperature in Infrared Photo Detectors," Proceedings of the Joint Meeting of the IRIS Specialty Groups on Infrared Detectors and Imaging-Volume 1; 13-15 June, 1978, pp. 387-400.

For n^+ - on - p HgCdTe photodiodes at relatively high temperatures, diffusion current from the p-side of the junction determines the $R_O A$ product. In this case, for a thick p-side region (i.e., much thicker than a minority-carrier diffusion length L_e), Equation 5 reduces to

$$R_O A = \frac{1}{q} \sqrt{\frac{kT}{q}} \frac{N_A}{n_i^2} \sqrt{\frac{\tau_e}{\mu_e}} \quad (9)$$

If the thickness of the p-side of the n^+ - on - p photodiode is reduced to a thickness comparable to a minority - carrier diffusion length through the use of a perfectly reflecting backside contact, then, from Equation 8, the $R_O A$ product is given by

$$R_O A = \frac{1}{q} \sqrt{\frac{kT}{q}} \frac{N_A}{n_i^2} \sqrt{\frac{\tau_e}{\mu_e}} \coth \left(\frac{b_p}{L_e} \right) \quad (10)$$

and if $L_e > b_p$, then

$$R_O A = \frac{kT}{q} \frac{N_A}{n_i^2} \frac{\tau_e}{b_p} \quad (11)$$

that is, $R_O A$ is proportional to the product of N_A and τ_e for a "thin" p-type base region, whereas it is proportional to $N_A \tau_e^{1/2}$ for a "thick" p-type base region.

Generation-recombination (g-r) current is due to the thermal generation and recombination of carriers in the depletion layer.

The expression for $R_O A$ for g-r current has been derived by Sah, Noyce and Shockley.⁽⁴⁾ For bias voltages near $V = 0$, one has the following approximate expression,

4. C. T. Sah, R. N. Noyce and W. Shockley, "Carrier Generation and Recombination in P-N Junctions and P-N Junction Characteristics," Proc. IRE 45, 1228 (1957); see Equation 28, p. 1234.

$$(R_O A)^{-1} = \frac{q n_i W}{V_{bi} \sqrt{\tau_{no} \tau_{po}}} \quad (12)$$

where:

$$W = \text{depletion layer width} = \sqrt{\frac{2 \epsilon_s (V_{bi} + V)}{a N_B}} \quad (13)$$

$$V_{bi} = \text{built-in voltage} = \frac{kT}{q} \ln \left(\frac{N_A N_D}{n_i^2} \right) \quad (14)$$

τ_{no}, τ_{po} = minority carrier lifetimes on p and n sides of the junction.

Since diffusion-limited $R_O A$ increases as n_i^{-2} as the temperature is lowered, while generation-recombination noise increases as n_i^{-1} , there is a temperature at which the diode switches from diffusion to g-r limited behavior.

This is shown in Figure 1. The increase in $R_O A$ will not continue indefinitely as the temperature is decreased further; at some temperature, the surface leakage resistance (shunt resistance) dominates and $R_O A$ becomes independent of temperature. $R_O A$ versus temperature curves for diodes fabricated during this program are found in Section 6.5.

2.2 MINORITY CARRIER LIFETIME MECHANISMS

In the previous subsection it was seen that $R_O A$'s for both diffusion and generation-recombination limited operation depend on the minority carrier lifetime. Three mechanisms can act to limit the lifetime: Auger, radiative, and Shockley-Read. Of these, Auger and radiative are intrinsic to the material and operate even in perfect material samples, while Shockley-Read recombination is due to impurities and defects. In this subsection, analytical models of the three mechanisms are presented.

SOURCES OF NOISE

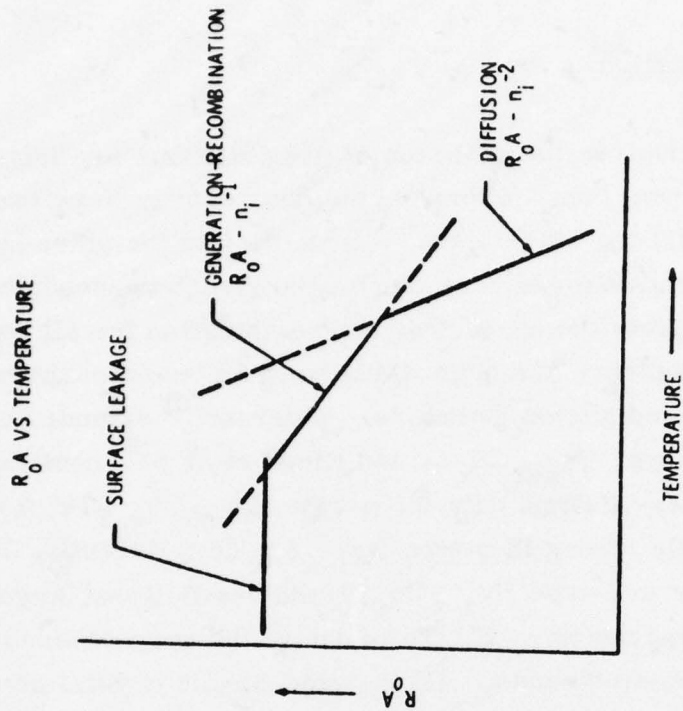
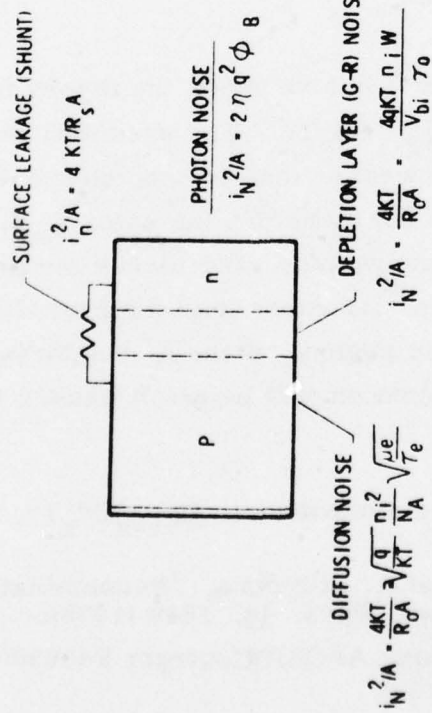


Figure 1. Sources of Noise in Photodiodes

2.2.1 Auger Recombination

Auger recombination involves the collision of two electrons (or holes) within the conduction (or valence) band, whereby one gains energy to be excited to a higher band state while the other makes a transition to the other band. This recombination mechanism is very much band structure-dependent. There is not yet a complete theory of Auger recombination for all types of band structure, but the theory has been worked out for some of the materials which are used in infrared photon detectors. Petersen⁽⁵⁾ extended the theory to the nondegenerate n-type $\text{Hg}_{1-x}\text{Cd}_x\text{Te}$ and Kinch et al.,⁽⁶⁾ confirmed his theory with their carrier-lifetime data for n-type $\text{Hg}_{0.8}\text{Cd}_{0.2}\text{Te}$; Auger recombination is relatively strong in n-type $\text{Hg}_{1-x}\text{Cd}_x\text{Te}$. Recently, Petersen has extended the theory to p-type $\text{Hg}_{1-x}\text{Cd}_x\text{Te}$ and verified that Auger recombination in n-type and p-type $\text{Hg}_{1-x}\text{Cd}_x\text{Te}$ is due to the very different shapes of the valence and conduction bands. All the zinc-blende crystal structure semiconductors have similar band structures and so would have similar Auger recombination properties.

In very recent work, Petersen⁽⁷⁾ has extended the theory of Auger recombination to degenerate n-type $\text{Hg}_{1-x}\text{Cd}_x\text{Te}$. The essential result is that Auger recombination is considerably weaker than in nondegenerate $\text{Hg}_{1-x}\text{Cd}_x\text{Te}$ of the same alloy composition x (and therefore the same λ_{co}). This conclusion is important to the design of an optimum zinc-blende semiconductor PV detector, which will be an n^+pp^+ structure with the photodetection occurring in the less heavily doped p-type region. If the n^+ region is statistically degenerate, its Auger recombination will be much weaker than otherwise

-
5. P. E. Petersen, "Auger Recombination in $\text{Hg}_{1-x}\text{Cd}_x\text{Te}$," J. Appl. Phys. 41, 3465 (1970).
 6. M. A. Kinch, M. J. Brau and A. Simmons, "Recombination Mechanisms in 8-14 μm HgCdTe ," J. Appl. Phys. 44, 1649 (1973).
 7. P. E. Petersen, Final Report, AFOSR Contract F49620-77-C-0028, Feb. 1979.

expected from the high carrier concentration, so that diffusion current from the n^+ region can be small and the corresponding shot noise negligible.

The Auger lifetime is given by

$$\tau_A = \frac{2n_i^2 (n_o/2G_{ee})}{(n_o + p_o + \Delta n) [n_o + \Delta n + \beta (p_o + \Delta n)]} \quad (15)$$

where G_{ee} is the generation rate for the electron-electron processes and β is a very small number, expressing the reduced probability of hole-hole processes due to the band structure. For extrinsic p-type $\text{Hg}_{0.6}\text{Cd}_{0.4}\text{Te}$ at typical temperatures, with negligible injected carriers, this reduces to

$$\tau_A = 2 \tau_{Ai} \quad (16)$$

independent of the doping level, where τ_{Ai} is the Auger lifetime in intrinsic material. For extrinsic n-type $\text{Hg}_{0.6}\text{Cd}_{0.4}\text{Te}$,

$$\tau_A = 2 \left(\frac{\eta_i}{\eta_o} \right)^2 \tau_{Ai} \quad (17)$$

The magnitude of τ_{Ai} can be easily calculated for the case of nondegenerate, parabolic bands by (8)

$$\tau_{Ai} = \frac{3.8 \times 10^{-18} \epsilon_\infty^2 (1+\mu)^{1/2} (1+2\mu) \exp \left[\frac{1+2\mu}{1+\mu} \frac{E_g}{kT} \right]}{\left(\frac{m_e^*}{m_o} \right) |F_1 F_2|^2 \left(\frac{kT}{E_g} \right)^{3/2}} \quad (18)$$

8. Blakemore, J.S., Semiconductor Statistics, Pergamon Press, Oxford (1962) Chapter 6.

where $\mu = m_e^*/m_h^*$ is the effective mass ratio of electrons to holes, a small number in (Hg, Cd)Te, and F_1 and F_2 are overlap integrals depending on the exact shape of the conduction and valence bands. Uncertainty in the overlap integrals, together with other approximations and assumptions used in the modeling, mean that Auger calculations are expected to give only order-of-magnitude accuracy. The qualitative results can be relied upon only for $\tau_A \gg \tau_{\text{rad}}$.

2.2.2 Radiative Recombination

Radiative recombination involves the recombination of an electron-hole pair by emission of a photon with approximately the gap energy. If the transition is between band extrema located at the same point in k-space, then it is "direct" radiative recombination and involves only the photon emission; this is the case for all the useful infrared photon detector materials. The lowest possible thermal generation rate in an effectively perfect semiconductor crystal occurs when Auger recombination is negligible so that only radiative recombination remains. Thus to maximize the detector performance, one always wants to reach the "radiative recombination limit" of the detector material.

Van Roosbroeck and Shockley⁽⁹⁾ showed originally that the radiative recombination rate is given in general by

$$R_r = \frac{8\pi k^3 T^3}{h^3 c^2} \int_{U_g}^{\infty} \frac{n_1^2 \alpha U^2 dU}{\exp U - 1} \quad (19)$$

Using a theoretical expression for α , Hall⁽¹⁰⁾ carried out the integration and derived:

9. W. vanRoosbroeck and W. Shockley, "Photon-Radiative Recombination of Electrons and Holes in Germanium," Phys. Rev. 94, 1558 (1954).
10. R.N. Hall, Proc. Inst. Electr. Eng. B. Suppl. 106, 923 (1959).

$$R_r = 5 \times 10^{13} n_i^2 \epsilon_\infty^{1/2} \left(\frac{m_o}{m_e^* + m_h^*} \right)^{3/2} \left(1 + \frac{m_o}{m_e^*} + \frac{m_o}{m_h^*} \right) \left(\frac{300}{T} \right)^{3/2} E_g^2 \quad (20)$$

In terms of lifetime,

$$\tau_r = \frac{n_i^2}{R_r (n_o + p_o + \Delta n)} \quad (21)$$

Thus, the radiative lifetime is the same in n-type as in p-type material, for the same doping levels, unlike Auger lifetime.

A comparison of radiative and Auger lifetime for $\text{Hg}_{0.6}\text{Cd}_{0.4}\text{Te}$ of both carrier types is given in Table 1. In either n- or p-type $\text{Hg}_{0.6}\text{Cd}_{0.4}\text{Te}$, radiative lifetime dominates over Auger lifetime. Only for high temperatures or doping levels does Auger become comparable to radiative, and then only for n-type material. To avoid Auger recombination altogether, the photo-diode should be dominated by properties of the p-side; this is accomplished with an n+ on p junction structure.

2.2.3 Shockley-Read Recombination

In many semiconductors, lifetime is determined not by the Auger or radiative processes, but by defects in the material. These defects introduce energy levels in the forbidden gap, which allow holes and electrons to more easily recombine. The theory of a single defect level in the energy gap was developed by Shockley and Read.⁽¹¹⁾ Previously, Shockley-Read lifetime has been reported in heavily compensated n-type $\text{Hg}_{0.8}\text{Cd}_{0.2}\text{Te}$ by Kinch⁽⁶⁾,

11. W. Shockley and W. T. Read, Jr., "Statistics of the Recombinations of Holes and Electrons," Phys. Rev. 87, 835 (1952).

Table 1. Calculated Lifetime in $\text{Hg}_{0.6}\text{Cd}_{0.4}\text{Te}$ (in sec), for Selected Temperatures and Carrier concentrations

T (°K)	Carrier Concentration N (cm^{-3})	(p-type) τ_A , for $p_o = N$	(n-type) τ_A , for $n_o = N$	(p or n) τ_{rad} , for $n_o + p_o = N$
100	10^{14}	1.3×10^{13}	2.6×10^{-1}	7.5×10^{-5}
	10^{15}	1.3×10^{13}	2.6×10^{-3}	7.5×10^{-6}
	10^{16}	1.3×10^{13}	2.6×10^{-5}	7.5×10^{-7}
150	10^{14}	4.5×10^5	2.2×10^{-1}	1.4×10^{-4}
	10^{15}	4.5×10^5	2.2×10^{-3}	1.4×10^{-5}
	10^{16}	4.5×10^5	2.2×10^{-5}	1.4×10^{-6}
200	10^{14}	7.4×10^1	2.2×10^{-1}	2.1×10^{-4}
	10^{15}	7.4×10^1	2.3×10^{-3}	2.1×10^{-5}
	10^{16}	7.4×10^1	2.3×10^{-5}	2.1×10^{-6}
250	10^{14}	3.7×10^{-1}	2.7×10^{-1}	2.8×10^{-4}
	10^{15}	3.7×10^{-1}	2.7×10^{-3}	2.8×10^{-5}
	10^{16}	3.7×10^{-1}	2.7×10^{-5}	2.8×10^{-6}

and by Ayache and Marfaing.⁽¹²⁾ These were majority carrier lifetimes, in n-type material, however.

Shockley-Read lifetime is given by

$$\tau_{\text{S-R}} = \frac{\tau_{p_o} (n_o + n_i + \Delta n) + \tau_{n_o} (p_o + p_i + \Delta n)}{(n_o + p_o + \Delta n)} \quad (22)$$

where τ_{p_o} is the lifetime for holes in highly n-type material, and τ_{n_o} is the lifetime for electrons in highly p-type material, n_o is the thermal equilibrium concentration of electrons, p_o is the thermal equilibrium concentration of holes and Δn is the concentration of photo-excited electron-hole pairs.

12. J. C. Ayache and Y. Marfaing, Compt. Rend. Acad. Sci. B265, 568 (1967)

τ_{no} and τ_{po} can be expressed as

$$\tau_{po} = \frac{1}{\sigma_n v_{th} N_t} \quad (23)$$

and

$$\tau_{po} = \frac{1}{\sigma_p v_{th} N_t} \quad (24)$$

where σ_n and σ_p are the effective capture cross-sections for electrons and holes, v_{th} is the thermal velocity defined by

$$v_{th} = \sqrt{3 kT / m_e} \quad (25)$$

and N is the density of S-R recombination centers, n_i and p_i are defined as:

$$n_i = N_c \exp (E_t - E_c) / kT \quad (26)$$

$$p_i = N_v \exp (E_v - E_t) / kT \quad (27)$$

where N_c and N_v are the conduction and valence band density of states, E_c and E_v are the conduction and valence band energies, and E_t is the energy level of the Shockley-Read recombination center. In the simplest case of interest for p-type material, with small Δn and E_t below midgap,

$$\tau_{S-R} = \tau_{no} \left(1 + \frac{p_i}{p_o} \right) = \tau_{no} \left(1 + \exp \left[\frac{E_F - E_t}{kT} \right] \right) \quad (28)$$

At low temperatures, the Fermi level E_F is below the trap level, and the lifetime is constant at τ_{no} . Lifetime increases exponentially with increasing

temperature for $E_F > E_t$, until limited by Auger or radiative recombination. The energy level of the Shockley-Read defect can be determined from a plot of lifetime versus temperature, through Equation 22.

Because Shockley-Read recombination is determined by the particular defect involved, no a priori numerical calculations are possible. The density of trapping centers and the capture cross-sections are needed to determine τ_{no} , and E_t must also be known. However, the temperature dependence of Shockley-Read lifetime is distinct from Auger or radiative lifetimes, allowing positive identification of the recombination mechanism. The dependence of lifetime on excess carrier density Δn can also be used to distinguish between the three mechanisms. Shockley-Read recombination is discussed in more detail in Section 7.1.

SECTION 3

MATERIAL PREPARATION

3.1 BULK CRYSTAL GROWTH

All of the material used for this contract was grown at the Honeywell Corporate Material Sciences Center. The quench-annealed material (crystal 52374) was grown under a previous Air Force contract. The growth process was described in the final report issued under that contract⁽¹³⁾. Ingot 52374 was selected because it was mostly single crystalline and very little of it had been used for other purposes. It had been intended as an Al doped ingot, but the Al adhered to the quartz capsule during growth and never got into the crystal. In our quench-anneal process, the ingot is inclined 20° from the horizontal when it is quenched and therefore has a small compositional gradient from top to bottom which is at right angles to the length of the ingot.

In order to ensure that every sample is uniform in composition, we cut rectangular pieces parallel to the length of the ingot. These pieces are called planks and are 1 cm long by 0.8 to 1.2 cm wide. The planks are given a letter and number designation indicating the distance from the tip of the crystal in cm and the distance from the top-side of the crystals in mm. For example, sample 52374, J4 is the fourth 1-mm thick plank from the top of section J which is 9 to 10 cm from the tip of crystal 52374. Forty-four such planks were cut mainly from sections I through O (8 to 15 cm from tip) and density was measured as described in Section 5.2. The composition of these 44 planks was $x = 0.39 \pm 0.01$, although each plank was uniform to ± 0.002 . Hall measurements, described in Section 5.1, showed that the hole concentration for these planks was $1.7 \pm 0.2 \times 10^{16} \text{ cm}^{-3}$ as grown. However,

13. J.L. Schmit and E.S. Johnson, "Exploratory Development on $\text{Hg}_{1-x}\text{Cd}_x\text{Te}$ Improvement," Phase II, March 1977, AFML-TR-77-21.

the residual impurity content of 52374 is $4 \pm 2 \times 10^{15}$ donors cm^{-3} , as indicated by Hall measurements on planks D6, H4, K6 and T7 after annealing to remove stoichiometric acceptors.

Most of these planks were never made into diodes. Eight were made porous by annealing at too high a temperature, several were consumed during learning how to make good MIS devices and some were simply not used. Tables 5 and 6 in Section 6.1 list the samples from which τ_e , L_e and $R_o A$ were taken.

Most of the samples were taken from one crystal (52374) because we expected that unknown variations in impurities and defects from crystal to crystal would affect the lifetime. However, one variation which could be easily controlled was the crystal growth method. Six samples were cut from an 3-mm diameter zone leveled crystal. This crystal, 96V, was grown by C. J. Speerschnider in 1970 under Honeywell internal funding. The crystal was grown similar to quench-anneal crystals through the quenching step, but instead of annealing the ingot to remove dendrites, a molten zone was passed through the ingot at 0.03 cm/hr to form a single crystal which was p-type. The six samples from 96V, labeled K1 through K6, have $x = 0.392 \pm 0.005$ and had a hole concentration of $5.2 \times 10^{16} \text{cm}^{-3}$ before annealing.

3.2 CRYSTAL ANNEALING

When an ingot is grown it is normally annealed in its entirety in the growth ampule in order to remove the dendrites formed during quenching. That anneal is considered part of the growth process and is not the topic of this section. We anneal for two reasons: either to lower the stoichiometric acceptor concentration or to diffuse-in an impurity.

The stoichiometry of crystals is adjusted as described under a previous contract⁽¹³⁾. Briefly, crystal samples, usually $\sim 1 \times 1 \times 0.1 \text{ cm}^3$, are

loaded into quartz capsules with excess Hg and freshly crushed (Hg, Cd)Te powder, evacuated and sealed off. The capsule is held in a vertical tube furnace for several weeks and quenched in water. Due to a small positive temperature gradient in the furnace, the sample is annealed under the maximum vapor pressure of its constituents at the sample temperature. The choice of annealing temperature determines the final acceptor concentration⁽¹⁴⁾ which compensates the residual donor impurity concentration. The difference between the acceptor and donor concentrations gives the hole concentration in a sample. Under this contract, a 30-day anneal at 275°C was used to reduce the acceptor concentration to a negligible level so the residual donor concentration could be determined. Recall from Section 3.1 that crystal 52374 has $\sim 4 \times 10^{15}$ donors cm^{-3} . Table 1 lists the hole concentration before and after annealing at various temperatures. It includes an estimate of the acceptor concentrations obtained by assuming the donor concentration is uniformly $4 \times 10^{15} \text{cm}^{-3}$.

Table 2. Acceptor Concentration as a Function of Annealing Temperature

Sample	$N_A - N_D$ (Before) ($\times 10^{16} \text{cm}^{-3}$)	Anneal		$N_A - N_D$ (after) ($\times 10^{15} \text{cm}^{-3}$)	$\sim N_A$ (after) ($\times 10^{15} \text{cm}^{-3}$)
		Time (Days)	Temperature (°C)		
52374, D6	1.2	30	275	-4.0	0
52374, P4	1.9	26	304	1.4	5.4
96V, K3	5.21	30	352	4.3	8.3
52374, N9	2.05	62	375	8.3	12.3

14. J.L. Schmit and E.L. Stelzer, J. of Electronic Matter. 7, 65 (1978).

In order to get high hole concentrations, we added copper to the samples before annealing. The method was straightforward: copper was first sputtered in a thick layer on a dummy substrate to determine the deposition rate. With the sputter process in steady state, the (Hg, Cd)Te planks were moved into position to be sputtered for a few seconds to receive a few angstroms of Cu. A 1\AA thick layer of Cu diffused uniformly through our sample thickness should provide 3×10^{15} acceptor/cm³. The Cu coated samples were sealed in a capsule with Hg and powdered (Hg, Cd)Te, evacuated, sealed and annealed. Samples annealed for 4 or 7 days at 650°C with insufficient Hg to provide the vapor pressure over free Hg (35 atmospheres) developed $\sim 1.2 \times 10^5 \text{ cm}^{-2}$ voids between 2 and 5 μm in diameter. These samples were not suitable for MIS devices or diodes and were not used further. Samples without Cu also developed pits under these conditions. Later diffusion anneals were for 7 days at 450°C with excess Hg and did not show pitting. This technique was used to prepared Cu doped samples for the MIS and diode work.

3.3 LIQUID PHASE EPITAXY GROWTH

Part way through this contract it became apparent that neither quench-annealed material nor zone-leveled material was free of lifetime limiting Shockley-Read (SR) recombination centers. The growth process most likely to provide material with a lower concentration of SR centers was LPE (Liquid Phase Epitaxy) due to its lower growth temperature.

During the early 1970's we attempted LPE growth from a Hg rich melt, but were not very successful. The very large segregation coefficient for Cd (the Cd concentration in a given layer is ~ 50 times the Cd concentration in the metal-rich melt it grew from) made composition control very difficult. Under this contract we chose to pursue the LPE growth of (Hg, Cd)Te from a Te rich melt on a CdTe substrate. The segregation coefficient is

much less with a Te-rich melt and the lower Hg vapor pressure permits open-tube slider growth.

We have designed and built a system based on our experience with slider LPE growth of III-V compounds. As of January 15, 1979, we determined a few liquidus compositions and temperatures, determined the parameters of surface preparation, slider-substrate clearance, degree of super-cooling, etc., which allow the melt to wipe-off, and have attempted 16-layer growths. Most of the evaluation to date has been microscopic determination of growth morphology, but the more recent layers are p-type and are good enough to begin electrical measurements. No LPE material was grown or evaluated during 1978, therefore, the diode measurements and the conclusions of this report refer only to quench-anneal and zone-level grown material. The growth and evaluation of LPE (Hg, Cd)Te is the goal of our 1979 work and will be reported in early 1980.

SECTION 4

DEVICE FABRICATION

4.1 MIS SAMPLE FABRICATION

The basic MIS structural configuration used for this work is shown in Figure 2. The structure consists of a (Hg, Cd)Te substrate upon which a dielectric insulator (typically 4000 Å thick) is deposited. The gate electrodes are circular (0.015 inch diameter) gold dots evaporated to a thickness of about 100 Å. Smaller indium dots, 0.005 inch in diameter, provide a contact pad onto which a gold wire is bonded by thermal compression.

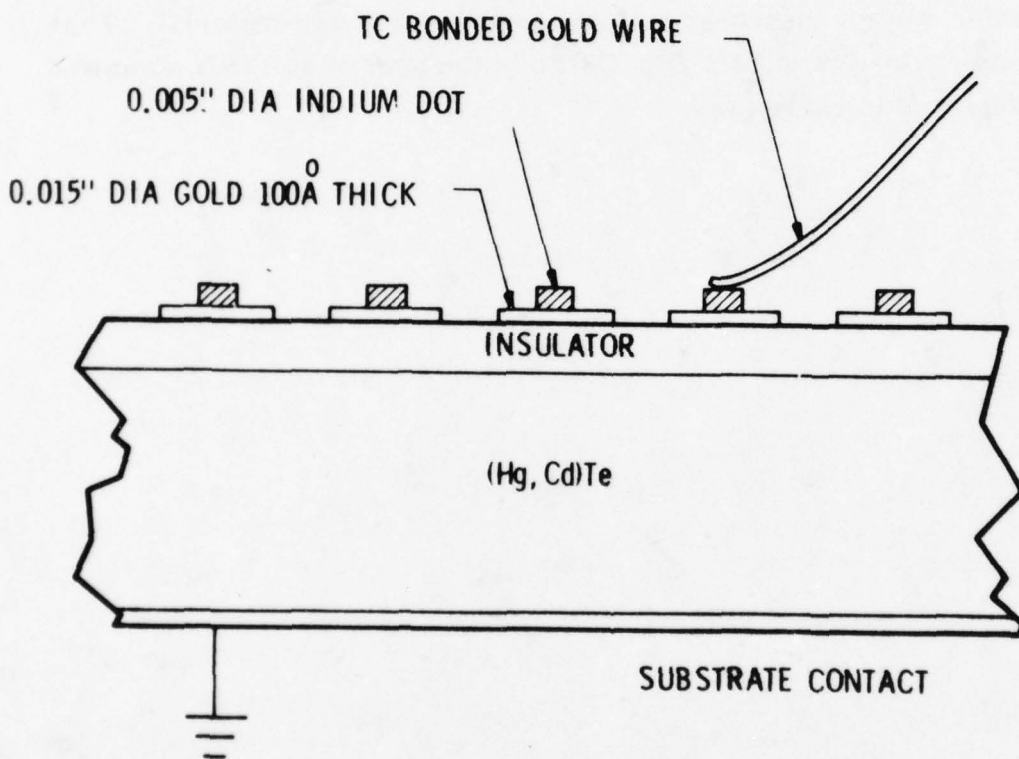


Figure 2. MIS Structure Configuration

Prior to the fabrication of MIS structures, the wafer of (Hg,Cd)Te is mounted on a lapping fixture and lapped with successively finer abrasives. The wafer is then removed from the fixture, rinsed, cleaned, and then etched in a 5:1 methanol/bromine solution for 10 seconds. The etching solution is continuously circulated to ensure a smooth and uniformly etched surface. The etch is followed by a series of rinses.

An insulating coating is then deposited. The insulator used for most devices was thorium tetrafluoride (ThF_4). This insulator was chosen primarily for its low pinhole density, and it resulted in a high yield of operative MIS structures. In addition, it has a high dielectric constant ($\epsilon_{\text{io}} \approx 12 \epsilon_0$) which allows a reasonably thick coating ($\sim 4000\text{\AA}$ in this case). The ThF_4 /(Hg,Cd)Te interface has also been found to exhibit lower surface state densities than most of the other dielectrics studied.⁽¹⁵⁻¹⁷⁾ ThF_4 was deposited by evaporation of ThF_4 powder in a vacuum.

Sputtered ZnS was also used as the insulator on several MIS samples. This was primarily done as a diagnostic aid in fabricating photodiodes, which use ZnS as the surface passivation layer. MIS C-V curves are used to determine the ZnS / (Hg,Cd)Te surface potential, which can have a large effect on photodiode operation. The curves are also used to determine bulk carrier concentration. For both MIS structures and photodiodes fabricated on this program, ZnS was deposited by RF sputtering.

-
15. J. D. Beck, R.M. Broudy, and R.W. Bechdolt, "Metal-Insulator-Semiconductor Results in 3 to 5 Micrometer (Hg,Cd)Te," Proc. IRIS Detector Specialty Group Meeting, 1977.
 16. R.W. Bechdolt, "A Metal-Insulator-Semiconductor Study of the Bulk and Surface Properties of (Hg,Cd)Te," Master's Thesis, Department of Electrical Engineering and Computer Science, Massachusetts Institute of Technology, May, 1977.
 17. J.D. Beck and R.W. Bechdolt, "Exploratory Development of (Hg,Cd)Te: Trapping and Surface Processing," First Interim Technical Report, AFML Contract F33615-76-C-5070, January-October 1976.

After insulator deposition, the next step was evaporation of the gold field plate. Circular dots, 0.015 inch in diameter, were evaporated to a thickness of approximately 100 Å through a metal mask. The thin layer of gold was used because it is semitransparent to infrared radiation with wavelengths between 3 and 5 micrometers. It was then possible to measure the bandgap with a spectral response setup described later in this section. Next, indium dots of 0.005-inch diameter were evaporated onto the gold to a thickness of approximately 1.5 micrometer. These relatively soft indium pads could have gold wires bonded to them with little pressure so that no damage would result to the insulator. The substrate contact consisted of a conductive silver paste into which the wafer was pressed. The wafer was then mounted into a dewar.

4.2 PHOTODIODE FABRICATION

The diodes used in this study were formed by ion implantation of boron into p-type $\text{Hg}_{0.61}\text{Cd}_{0.39}\text{Te}$, resulting in an n^+ -on-p structure. A heavy dosage of boron was used, giving an electrically active donor concentration of approximately $2 \times 10^{18} \text{ cm}^{-3}$. This n^+ concentration was much greater than any of the p-side acceptor concentrations used, so that in all cases we had essentially a one-sided junction. In this way, only the properties of the minority-carrier electrons on the p-side mattered.

The fabrication procedure is outlined in Figure 3. It began with preparation of the wafer back surface by lapping with successively finer abrasives, cleaning, and etching in a 5:1 methanol/bromine solution. The same procedure was used for the wafer front surface, followed immediately by sputtering of approximately 1000 Å of ZnS over the whole surface. A thick photoresist pattern was then deposited over the insulator to define the diode active areas for implant. In most cases, the pattern consisted of linear arrays of $10 \times 10 \text{ mil}^2$ squares; however, several of the early arrays used patterns with a wide range of areas.

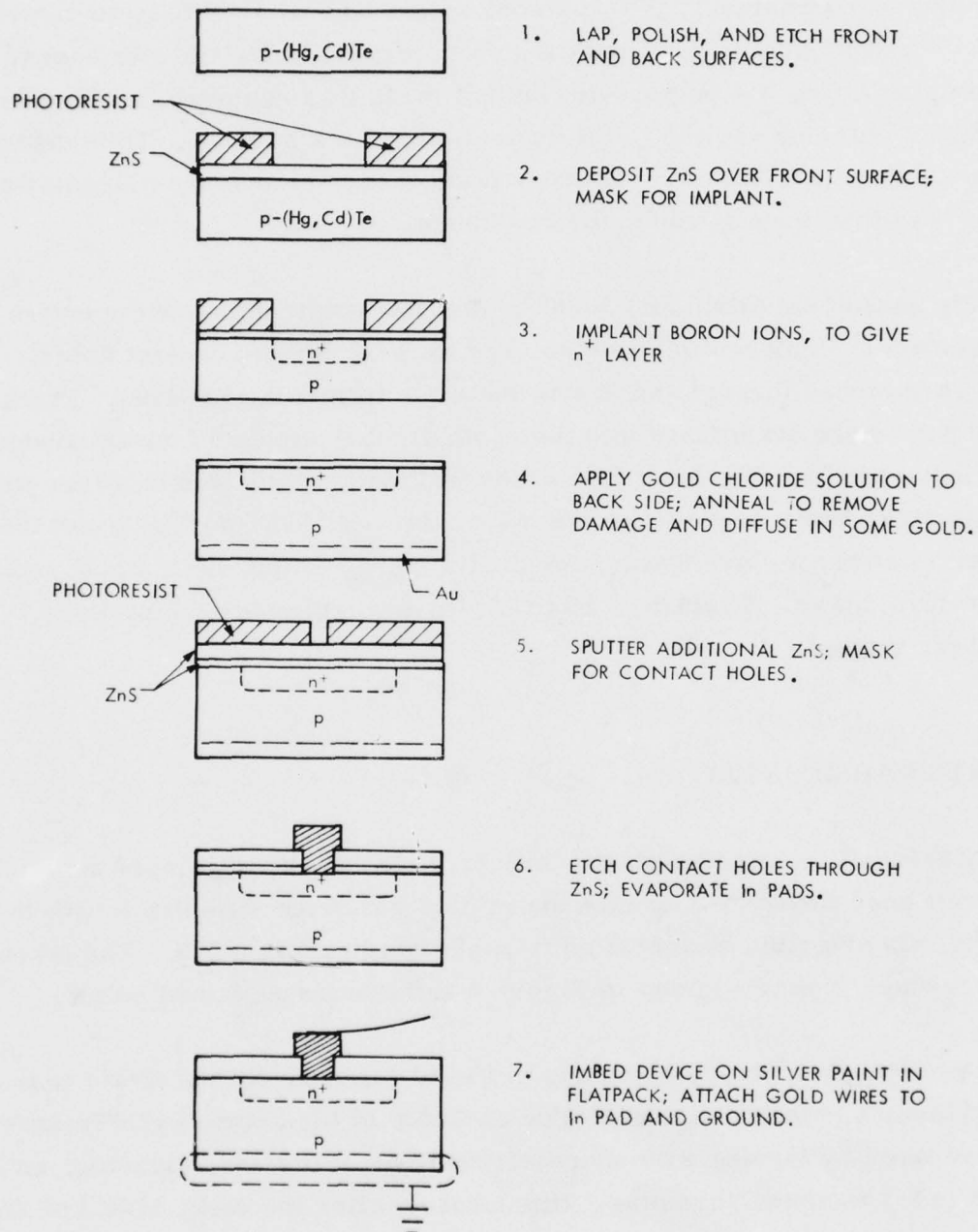


Figure 3. Photodiode Fabrication

Boron ions were implanted in two steps, at 100 KeV and 40 KeV, to obtain the desired doping profile. The dosage was $1 \times 10^{15} \text{ cm}^{-2}$ in both cases. After implantation, the photoresist implant mask was removed, and a solution of gold chloride applied to the entire wafer back surface. This ensures a good ohmic p-side contact. A thermal anneal to remove the implantation damage was then done at 150°C for two hours.

After the anneal, an additional 3000Å of ZnS was sputtered over the entire front surface. Photoresist was then used to mask for the contact holes, which were etched through the ZnS to the n^+ - side of the junction. Thick indium pads were evaporated into the contact holes, and gold wires bonded to the indium pads. The back side of the wafer was imbedded in silver paint, in a flat pack, and a common ground wire attached. The flat pack was then mounted in either a glass dewar, for preliminary testing, or a metal variable-temperature dewar. Typically, 15 to 25 devices from each wafer were bonded for testing.

4.3 BITS FABRICATION

The Backside-Illuminated Tapered Structure (BITS) was developed at Honeywell specifically to measure the minority carrier diffusion length in HgCdTe. Its principle of operation is explained in Section 5.7. The fabrication procedure is diagrammed in Figure 4 and briefly explained below.

Fabrication began with angle-lapping of the IR-transparent substrate to the desired taper and then polishing. The backside of the p-type HgCdTe wafer was prepared by lapping with successively finer abrasives, cleaning, and etching in 5:1 methanol/bromine. Immediately after the etch, 1000 Å of ZnS was sputtered on to passivate the back surface. The backside was then glued to the tapered substrate.

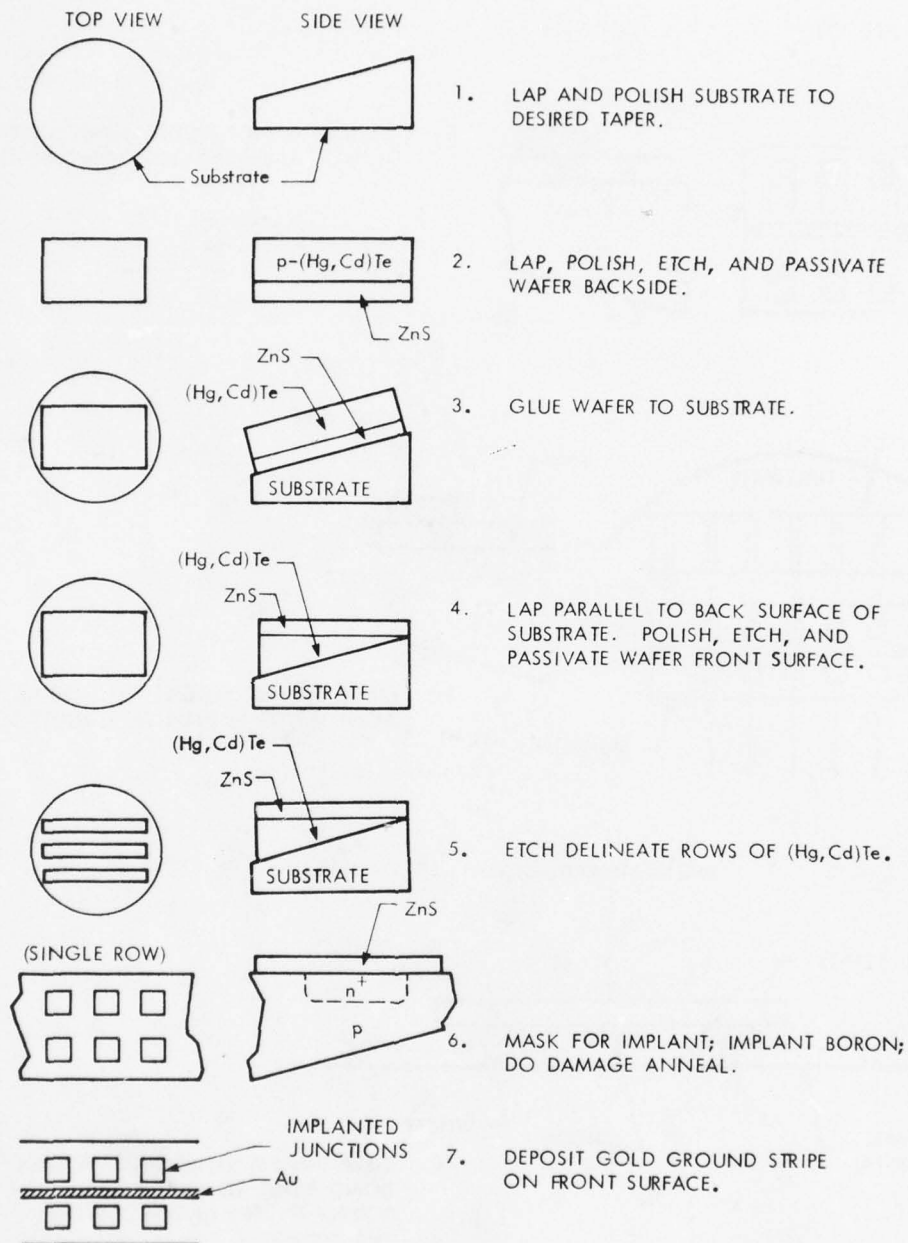


Figure 4. BITS Fabrication

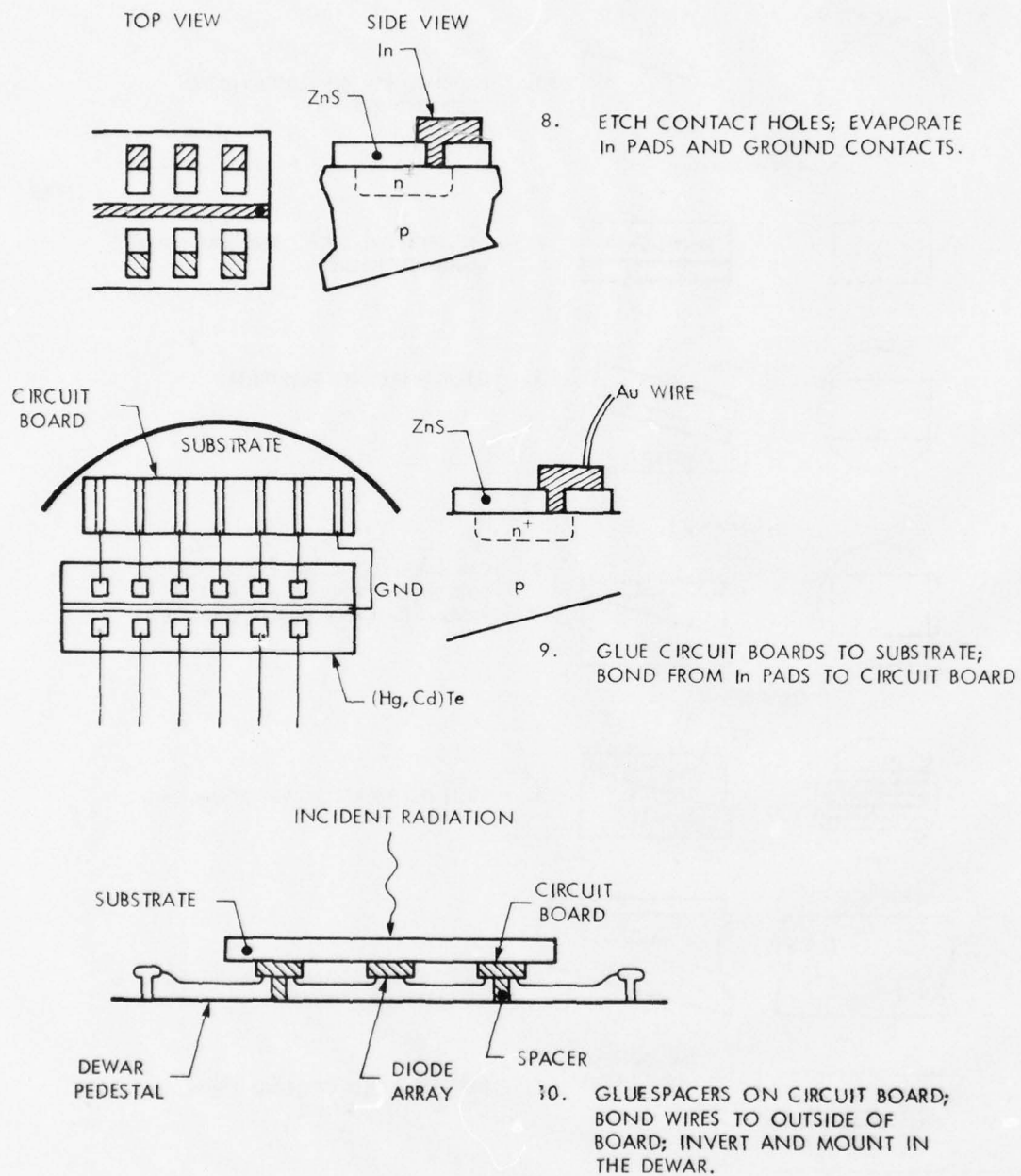


Figure 4. BITS Fabrication (Concluded)

The substrate was mounted on a lapping plug, and the HgCdTe/substrate structure lapped parallel to the substrate back surface. This resulted in a tapered slice of HgCdTe.

On each of the resulting rows, a double row of $4 \times 6 \text{ mil}^2$ implanted diodes was formed, essentially as described in Section 4.2. The major difference was the ground contact, which could not be formed on the inaccessible back surface. Instead, a 2-mil wide gold strip was deposited on the front surface, between the two rows of diodes. This was done after the damage anneal and before the second ZnS deposition. At the same time that contact holes were etched to the diode n^+ regions, holes were etched to the gold stripe at each end of the array. Silver paint was used to make contact between the gold strip and the ground wire. In some cases ground contact was made only at the thick end of the array to avoid damaging any thin-end diodes.

In order to mount the devices upside down, alumina circuit boards with chrome-gold patterns were epoxied to the substrate. Gold wires were bonded from the indium pads on the devices to the circuit boards. A second gold wire was bonded to the outside of the circuit board and left hanging free. An alumina spacer was then epoxied on top of the circuit board and the whole assembly inverted. The device was mounted by attaching the alumina spacers to the dewar pedestal with epoxy, leaving the diodes suspended above the pedestal and facing away from the outside environment. The gold wires connected to the circuit boards were then soldered to mounting terminals in the dewar.

A number of variations on the above procedure were tried. First, several substrate materials were used. CdTe had good IR transmission and an excellent thermal expansion match to HgCdTe, but its brittleness resulted in several cracked substrates during the fabrication procedure. Sapphire had good transmission and excellent mechanical strength; however, it was very

difficult to lap and polish. Irtran II (ZnS) was eventually selected for its good transmission, mechanical strength, and relative ease of angle lapping. No degradation in diffusion length was seen resulting from strain, due to some thermal expansion mismatch between ZnS and HgCdTe.

A major problem encountered during development of the BITS structure was stray radiation in the dewar. It was found that stray radiation making its way to the diode front surface could produce a sizable background current; the current often swamped out the current originating at the backside for the thicker elements. Because the expression relating diffusion length to signal current considered only signals originating at the back surface, this effect posed major problems in interpreting the data. Several measures were taken to minimize the background with good success. The first was to evaporate a thick chrome-gold layer between the HgCdTe rows, on the substrate surface, blocking the incident radiation between rows. The second was to blacken the inside of the dewar, and especially the pedestal directly under the device. These measures resulted in about an order of magnitude reduction in the background current.

SECTION 5

MEASUREMENT METHODS

This section details the methods used to characterize our $\text{Hg}_{1-x}\text{Cd}_x\text{Te}$ material and devices. It includes a description of how we make and interpret Hall measurements, and how we determine composition. We describe how MIS methods are used to determine electrical type and concentration and to determine alloy composition. The use of the diode reverse recovery technique and R_0A versus temperature measurements to determine lifetime are described. EBIC (Electron Beam Induced Current) and BITS (Backside Illuminated Tapered Structure) to determine minority carrier diffusion length are described.

5.1 DETERMINATION OF CARRIER CONCENTRATION USING HALL MEASUREMENTS

5.1.1 Electrical Contacts

During our previous contract with AFML⁽¹³⁾, we developed a technique for making ohmic contacts to $\text{Hg}_{1-x}\text{Cd}_x\text{Te}$ which were good down to 16K. Under the present contract, we needed to cool only to 77K, and so a simpler contacting technique was developed. Square samples $\sim 1 \times 1 \times 0.1 \text{ cm}^3$ suitable for Van der Pauw Hall measurements were used. The corners of each square were electropolated with Cu using CT367⁽¹⁸⁾ without masking. Indium dots were soldered to the corners using DIVCO Number 229 stainless steel flux and excess Cu was removed by a 1-second HNO_3 rinse. Copper leads were then attached and measurements made from either 300 or 400 to

18. Coppertech, Inc., 9th & Greenleaf St., Allentown, PA 18102.

77K. The advantage of these contacts over the Au ones used previously is ease of application. Since Cu is not as soluble as Au in In, no antidiffusion barrier is required and the entire operation can be done without masking the sample.

Low resistance ohmic contacts are made to n-type $\text{Hg}_{1-x}\text{Cd}_x\text{Te}$ by soldering with In just above its melting point without using flux.

5.1.2 Hall System

The temperature-dependent Hall and resistivity measurements on the p-type samples are made potentiometrically with a Fluke 8300A digital voltmeter. A Varian V2100 dc magnet and power supply are used for the field of 1 to 8 kilogauss. The cryogenic system is a Janis 8DT cryostat with a calibrated GaAs diode and Lakeshore DTC500 controller. Measurements are made at discrete temperatures on this system and plotted as a function of reciprocal temperatures to determine the carrier concentration as discussed below.

5.1.3 Determination of Carrier Concentration

Either Van der Pauw, or regular Hall measurements give the Hall coefficient, R_H , at each temperature and the resistivity is also routinely measured. However, knowing R_H at one temperature does not automatically give the hole concentration. The Hall coefficient is related to carrier concentration by the following expression:⁽¹⁹⁾

$$R_H = \frac{r (nb^2 - p)}{q (nb + p)^2} \quad (29)$$

19. E. H. Putley, The Hall Effect and Related Phenomena, Butterworths, London (1960).

where

r = scattering coefficient
 q = electronic charge
 n = electron concentration
 p = hole concentration
 b = the mobility ratio, μ_e/μ_h
 μ_e = electron mobility
 μ_h = hole mobility

The scattering coefficient is usually near one and we have no measure of it anyway, so we assume $r = 1$ in the following discussion. Equation 29 can be simplified under certain conditions to give the electron and hole concentrations directly. The usual conditions are exhaustion (when $n \gg p$ or $p \gg n$), cross-over (when $R_H = 0$), peak (when R_H is a maximum), and intrinsic (where $n = p$, usually at high temperature). These regions are indicated in Figure 5.

In n type material where $n \gg p$, Equation 27 reduces to

$$R_H = \frac{r}{qn} \quad \text{or} \quad n = \frac{1}{qR_H} = \frac{-6.25 \times 10^{18}}{R_H} \quad (30)$$

in cgs units. Similarly, in heavily p-type material where $p \gg nb^2$ Equation 29 reduces to

$$R_H = \frac{-r}{qp} \quad \text{or} \quad p = \frac{-1}{qR_H} = \frac{+6.25 \times 10^{18}}{R_H}. \quad (31)$$

Equations 30 and 31 apply only to heavily enough doped samples at low enough temperatures so that intrinsic carriers are negligible but not so low that the impurities are freezing out (are not ionized). Measurements must be made as a function of temperature to ascertain that the conditions are met. All the Hall measurements under this contract were taken over the range 77 to at least 300K. Figure 5 is a plot of R_H versus inverse

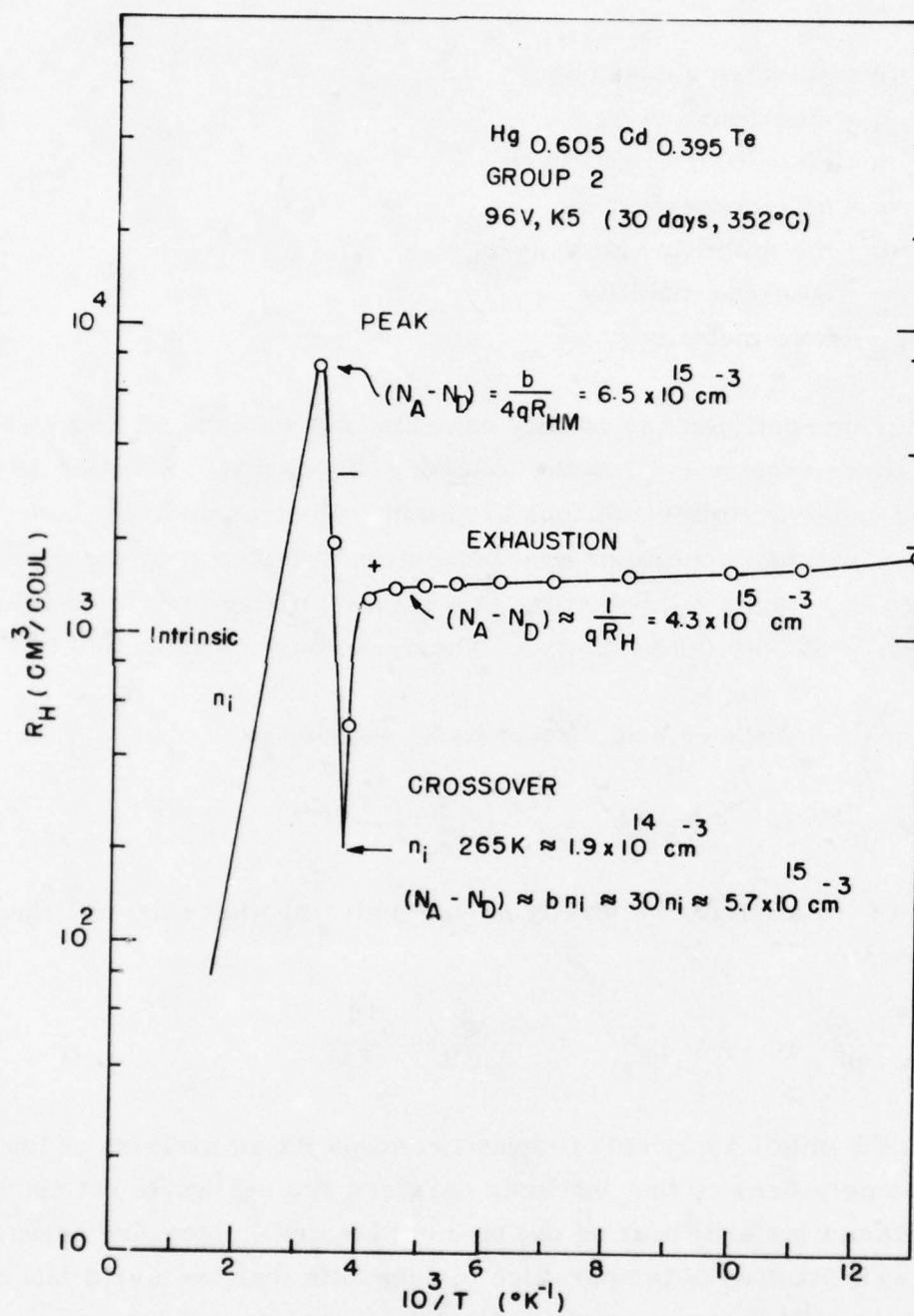


Figure 5. Typical Hall Coefficient versus Reciprocal Temperature

temperature for a typical sample measured. The value of $(N_A - N_D) = 4.3 \times 10^{15} \text{ cm}^{-3}$ is found from the exhaustion portion of this curve.

At the crossover where $R_H = 0$ Equation 29 reduces to

$$p = nb^2 = \frac{n_i^2 b^2}{p} = n_i b \quad (32)$$

If we assume $b = 30$, then the crossover temperature for the sample in Figure 5 yields a value of $(N_A - N_D) = p = 5.7 \times 10^{15} \text{ cm}^{-3}$. Only one digit is significant since the value of b is estimated and the exact temperature of the crossover is not accurately measured.

At the peak value of R_H , Equation 26 reduces to

$$R_H = \frac{(b-1)^2}{4bqp} \quad \text{or} \quad p = \frac{b}{4qR_H(\text{max})} \quad (33)$$

assuming $b \gg 1$. For the example shown in Figure 5, again assuming $b = 30$, we find $(N_A - N_D) = p = 6.5 \times 10^{15} \text{ cm}^{-3}$. As in the crossover case, only one digit is significant.

In the intrinsic case where $n = p$ because most electrons and holes are generated by thermal excitation across the bandgap, Equation 26 reduces to

$$R_H = \frac{(b-1)}{qn_i(b+1)} = \frac{1}{qn_i} \quad (34)$$

where n_i is the intrinsic carrier concentration.

Equation 34 is frequently used to determine n_i experimentally using n-type samples. Under this contract our main interest was in p-type samples, and since $(N_A - N_D)$ does not come into Equation 34, it cannot be used to determine

$(N_A - N_D)$. We simply use the calculated values of $n_i^{(20)}$ to complete the high-temperature portion of the Hall curve as shown in Figure 5.

5.1.4 Mobility Ratio

In much of the preceding discussion we used an estimated value of the electron to hole mobility ratio, b . The value used came from dividing the electron mobility of an n-type sample by the hole mobility measured in a p-type sample. An example of a plot of electron and hole mobilities is found in Figure 6, which is taken from Figure 30 of the Second Interim Report issued under a recent AFML contract.⁽²¹⁾ Dividing the electron mobility by the hole mobility gives an estimate of b , as shown in Figure 7. The ratio was determined for 11 pairs of samples from crystals which contained both n and p-type regions. The crystals were grown during 1971 through 1974. Figure 7 shows three typical plots. Averaging all 11 pairs gives the following estimate of b (Table 3):

Table 3. Mobility Ratio for $\text{Hg}_{0.6}\text{Cd}_{0.4}\text{Te}$

T (K)	b
400	28 ± 4
300	30 ± 4
200	34 ± 4
150	38 ± 4
100	44 ± 2
70	48 ± 6
40	63 ± 20
20	120 ± 60

20. J.L. Schmit, J. Appl. Phys. **41**, 2876 (1970).

21. E. L. Stelzer and J. L. Schmit, "Exploratory Development on $\text{Hg}_{1-x}\text{Cd}_x\text{Te}$ Improvement, Phase II," Interim Report under F33615-74-C-5041, January 1975.

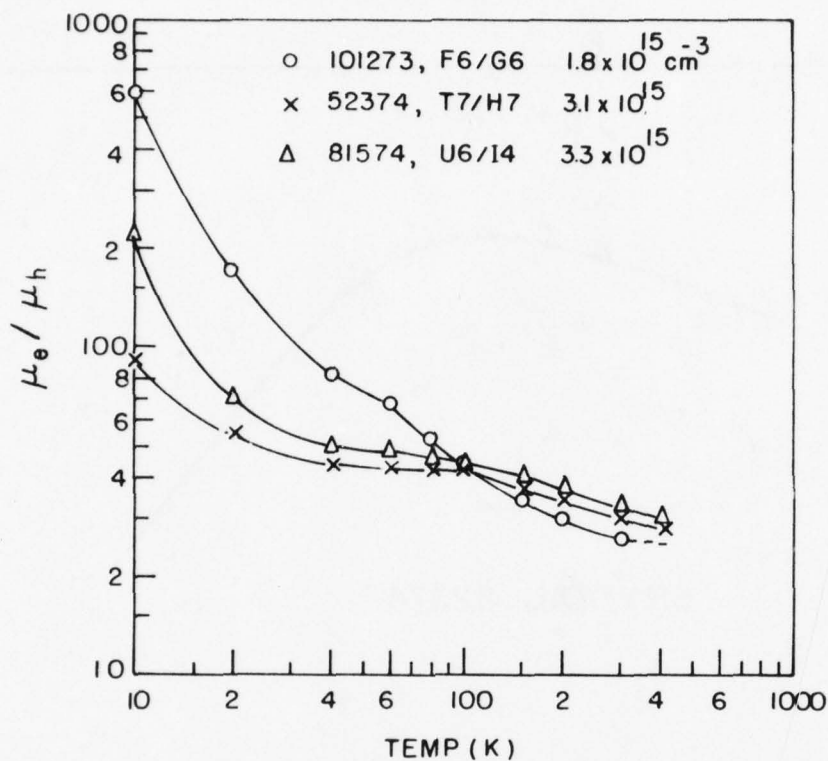


Figure 7. Temperature Dependence of the Mobility Ratio

Below about 100K the scatter is very bad due to ionized impurity scattering which depends on the dopant levels in both the n and the p-type samples. Above 100K where lattice scattering limits the mobility, the precision is approximately ± 10 percent. Recall that the basic premise of this determination of b is that the mobility does not depend on whether the carrier is a majority or a minority carrier; that is, the majority carrier mobility μ_e in n-type material equals the minority carrier mobility μ_e in p-type material, and similarly μ_h is the same in n-type and p-type materials. This contract provides data in Section 6.4 indicating that this a good assumption.

5.2 DETERMINATION OF ALLOY COMPOSITION

The major task of this contract has been to determine lifetime and minority carrier diffusion length as functions of hole concentration. It is necessary to hold other parameters, such as alloy composition, constant. Honeywell's long effort on $\text{Hg}_{1-x}\text{Cd}_x\text{Te}$ has resulted in the development and refinement of several reliable techniques for alloy composition determination described below.

5.2.1 Composition Determination by Density Measurement

The density method is the primary means of determining alloy composition in $\text{Hg}_{1-x}\text{Cd}_x\text{Te}$. The x value has been found to vary linearly with density by Wooley and Ray⁽²²⁾, Galazka⁽²³⁾, and by Blair and Newnham⁽²⁴⁾, so that measurements of crystal density can be used to determine x . The following expression gives the density versus x dependence for $\text{Hg}_{1-x}\text{Cd}_x\text{Te}$, where ρ is the density: $x(\text{Hg}_{1-x}\text{Cd}_x\text{Te}) = 3.5280 - 0.44924 \rho$.⁽²⁵⁾ The absolute value of x , determined by density measurements, has an uncertainty of about 1 mole percent due to uncertainties in the original standards used by the above authors; however, the precision or reproducibility of these measurements is closer to 0.1 mole percent, which corresponds to 0.005- μm in peak wavelength at 1.5 μm , or about 0.1 μm at 10 μm ⁽²⁶⁾. The density measurement is done by a standard lost-weight method which maintains the necessary

-
22. J. C. Woolley and B. Ray, *J. Phys. Chem. Solids* **13**, 151 (1960).
 23. R. R. Galazka, *Acta Phys. Polon.* **24**, 791 (1963).
 24. J. Blair and R. Newnham, Conference on the Metallurgy at Elemental and Compound Semiconductors, Boston, 1960, Interscience, New York p. 393 (1961).
 25. D. Long and J. L. Schmit, Semiconductors and Semimetals, Vol. 5, Chap. 5, Academic Press, New York, p. 243, (1970).
 26. J. L. Schmit and E. L. Stelzer, *J. Appl. Phys.* **40**, 4865 (1969).

precision by use of a microbalance and a high-density, low-volatility fluid.⁽²⁷⁾ The normal density determination procedure is to cut every fourth centimeter region from an ingot into planks, measure the density of each and interpolate the density of material between the measured planks. Under this contract, the density of all 44 planks used was measured.

5.2.2 Composition Determination by Fluorescence

Analysis of alloy compositions can be made by using an electron beam microprobe in which an electron beam is impinged on a sample causing x-rays characteristic of the individual atoms to be emitted. The x-rays at each energy are counted, giving a relative measure of the fraction of each element present. However, all elements are not equally efficient at being excited by the incident electrons and some of the x-rays are reabsorbed before they can be collected and counted. This technique is best used as a secondary standard to compare an unknown with known standards. We have studied the application of this technique to $\text{Hg}_{1-x}\text{Cd}_x\text{Te}$ and have standards available. The EDAX (Energy Dispersive Analysis of x-rays) attachment of our SEM (Scanning Electron Microscope) provides us with the capability of making measurements on small samples. The accuracy of the EDAX is only ~ 0.01 mole fraction, but it can measure samples as small as a few micrometers. The determination of tie lines under this contract has required the determination of composition on microscopic dendrites grown out of a Te solution. The electron beam microprobe has proven ideal for this work.

5.2.3 Composition Determination by Spectral Cutoff

The ideal way to determine the composition of infrared detectors is by measuring the cutoff energy of individual detectors since that is the

27. "FREON" E5, Fluorinated Ether, E. I. Dupont Co., Wilmington DE 19898.

parameter one seeks to control when measuring composition. A technique less destructive of the test plank is measurement of the spectral response of an MIS array fabricated on the surface of the plank. This technique gives good resolution and was used on one plank to verify the homogeneity of our starting crystal. The technique is described in greater detail in Section 5.3.3.

5.3 MIS DETERMINATION OF BULK PROPERTIES

MIS Capacitance-Voltage (C-V) techniques have previously been developed and extensively used for the bulk characterization of HgCdTe⁽¹⁶⁾. During this program, we have used some of the techniques to nondestructively determine majority carrier type, bulk doping concentration, and alloy composition (x-value). Because each wafer accommodates many small MIS devices, we are able to measure these properties in more detail than by Hall or density measurements, which average over the wafer.

5.3.1 Majority Carrier Type

The majority carrier type of the semiconductor is easily determined from the shape of the high-frequency C-V curve. A negative (or decreasing) slope in the capacitance-voltage curve in going from negative to positive voltage indicates p-type material, while a positive slope indicates n-type material. Most of the samples tested were p-type, although occasionally n-type regions were found around the sample edges.

5.3.2 Bulk Carrier Concentration

The high frequency C-V curve also determines the bulk carrier concentration defined by $N_B = N_A - N_D$. The necessary measured parameters are the insulator capacitance C_i (measured when the surface is accumulated),

and the minimum capacitance C_f (measured when the surface is strongly inverted). These quantities are indicated in Figure 8. The capacitance ratio is given by:

$$\frac{C_f}{C_i} = \frac{1}{1 + \frac{\epsilon_i}{\epsilon_s} \frac{W_m}{d}} \quad \text{where} \quad (35)$$

W_m = maximum depletion depth

d = insulator thickness

ϵ_i = insulator dielectric constant

ϵ_s = semiconductor dielectric constant

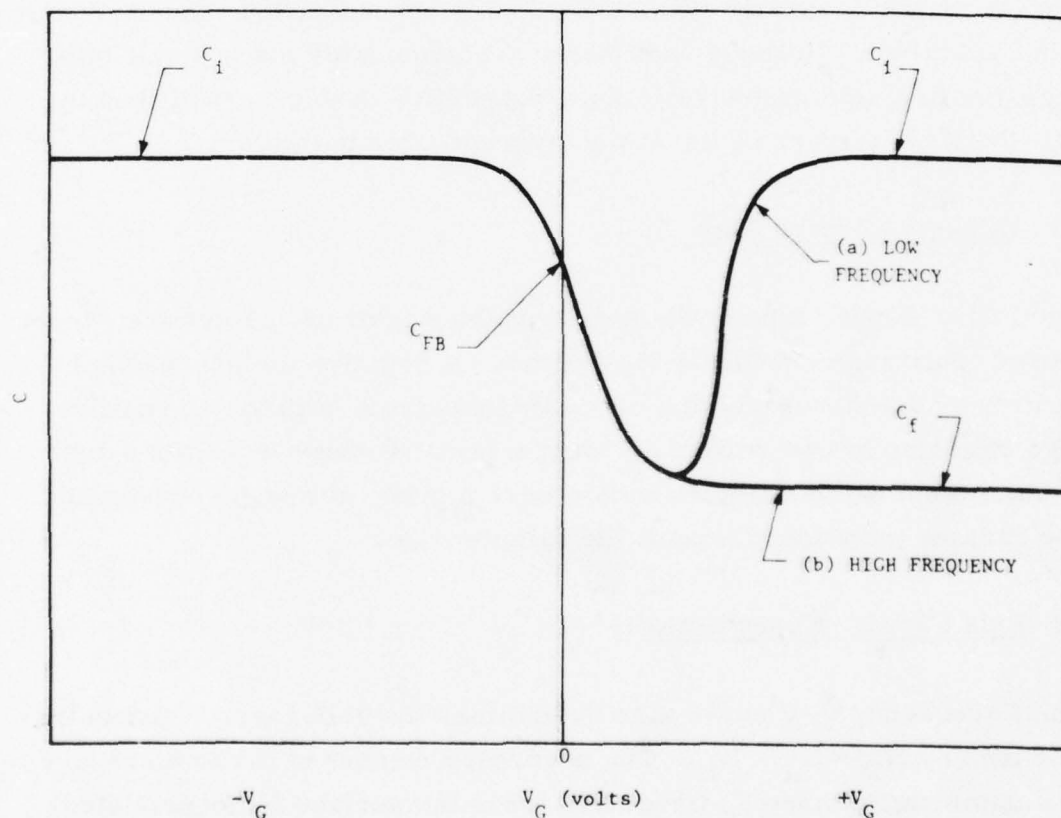


Figure 8. Ideal MIS Capacitance-Voltage Curves for a p-Type Semiconductor

The maximum depletion depth is determined by the bulk carrier concentration:

$$W_m \approx \sqrt{\frac{4 \epsilon_s kT \ln (N_B/n_i)}{q N_B}} \quad \text{where} \quad (36)$$

k = Boltmann's constant

T = temperature

q = electron charge

n_i = intrinsic carrier concentration.

Hence, N_B can be determined from the following equation:

$$N_B = \frac{4kT \ln (N_B/n_i)}{\epsilon_s q^2 A^2 \left(\frac{1}{C_f} - \frac{1}{C_i} \right)^2} \quad (37)$$

By simply measuring the insulator capacitance, C_i , and the high frequency inversion layer capacitance, C_f , via C-V curves, the net doping concentration can be determined.

It is necessary as well to know the dielectric constant (ϵ_s) and the intrinsic carrier concentration (n_i). For (Hg, Cd)Te, the dielectric constant is determined by extrapolating between the known value for $\text{Hg}_{0.8}\text{Cd}_{0.2}\text{Te}$ and that of CdTe. The intrinsic carrier concentration is determined from an expression derived by Schmit:⁽²⁰⁾

$$n_i = (8.445 - 2.2375x + 0.00342T) 10^{14} E_g^{3/4} T^{3/2} \exp(-E_g/2kT) \quad (38)$$

where x is the mole fraction of CdTe in (Hg, Cd)Te. The value of x is determined from the measured energy gap E_g (from a spectral response measurement), and an empirical relationship between E_g and x .

The estimates of net doping concentration N_B from MIS C-V data repeatedly show very good agreement with Hall data. In addition, the MIS technique allows a nondestructive mapping of the impurity concentration across the surface of a wafer of material, using photolithographic techniques to fabricate many small MIS structures.

The high-frequency C-V measurements are made using a Princeton Applied Research Model 410 Automatic C-V Test Station, operating at 1 MHz. No variations from the standard operating procedure are used. Devices are mounted in a specially designed glass dewar, shielded from stray radiation, and tested at the boiling temperature of Freon 14 (145K). Typically, about 20 MIS devices are bonded and tested for each HgCdTe wafer.

5.3.3 Bulk Composition

Because the gold gate on MIS structures is semi-transparent to infrared wavelengths, the MIS devices show photoresponse. This response versus wavelength can be used to find the material cutoff wavelength, and hence energy gap. Using a relationship between energy gap and x-value (in $\text{Hg}_{1-x}\text{Cd}_x\text{Te}$) from Schmit, ⁽²⁶⁾ the composition then can be determined. The necessary equations are:

$$E_g = \frac{hc}{\lambda} = \frac{1.24}{\lambda_{co}} \quad (39)$$

$$E_g = 1.59x - 0.25 + 5.233(10^{-4})T(1-2.08x) + 0.327x^3 \quad (40)$$

where

- E_g = energy gap (eV)
- λ_{co} = cutoff wavelength (μm)
- x = fraction of CdTe in $\text{Hg}_{1-x}\text{Cd}_x\text{Te}$
- T = temperature ($^{\circ}\text{K}$)

The spectral response measurement uses the fact that the capacitance is a function of the optical generation rate in and near the depletion region of an MIS device. The depletion width becomes smaller as the number of generated carriers increases; thus the capacitance will increase. In this measurement, a standard Perkin-Elmer spectral station is used as the source of radiation of different wavelengths. The radiation is chopped at a rate of 13 Hz. The capacitance modulation of the MIS device is monitored, and a plot of the relative amplitude of the capacitance variation versus wavelength is constructed. The measurement setup is shown in Figure 9.

A plot of relative response versus wavelength for one of the devices is shown in Figure 10. The cutoff region is quite clear, with a cutoff wavelength of $3.19 \mu\text{m}$. The x -value determined from this cutoff is $x = 0.386$, in good agreement with $x = 0.384$ determined from density measurements on this wafer. Although some x -variation exists across the wafers, the average x determined from several MIS samples agrees with the density value very well, usually within 0.01.

5.4 REVERSE RECOVERY TECHNIQUE

5.4.1 Qualitative Description of Technique

A conceptual model of the measurement circuit is shown in Figure 11. For the case of an $n^+ \text{-on-p}$ diode, a forward current, I_F , composed primarily of electrons, is injected into the p-side. The transient response determines the minority carrier lifetime of the electrons on the p-side.

By applying a sudden reverse bias, a transient curve consisting of two phases can be observed. The first phase is one of constant reverse current, I_R , and lasts for a storage time, t_s . During this time, the junction voltage remains positive; the current is supported by the previously

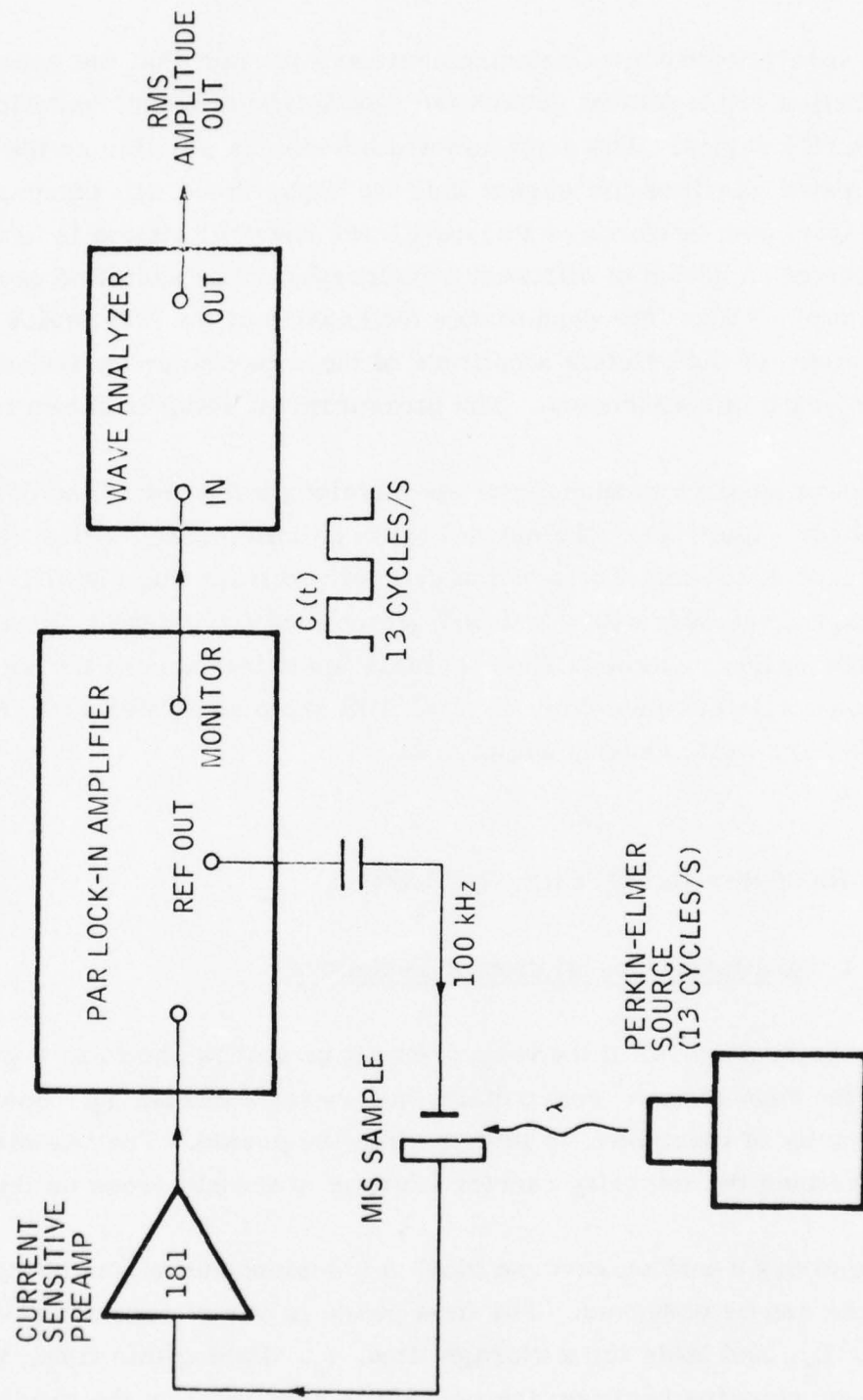


Figure 9. MIS Spectral Measurement Setup

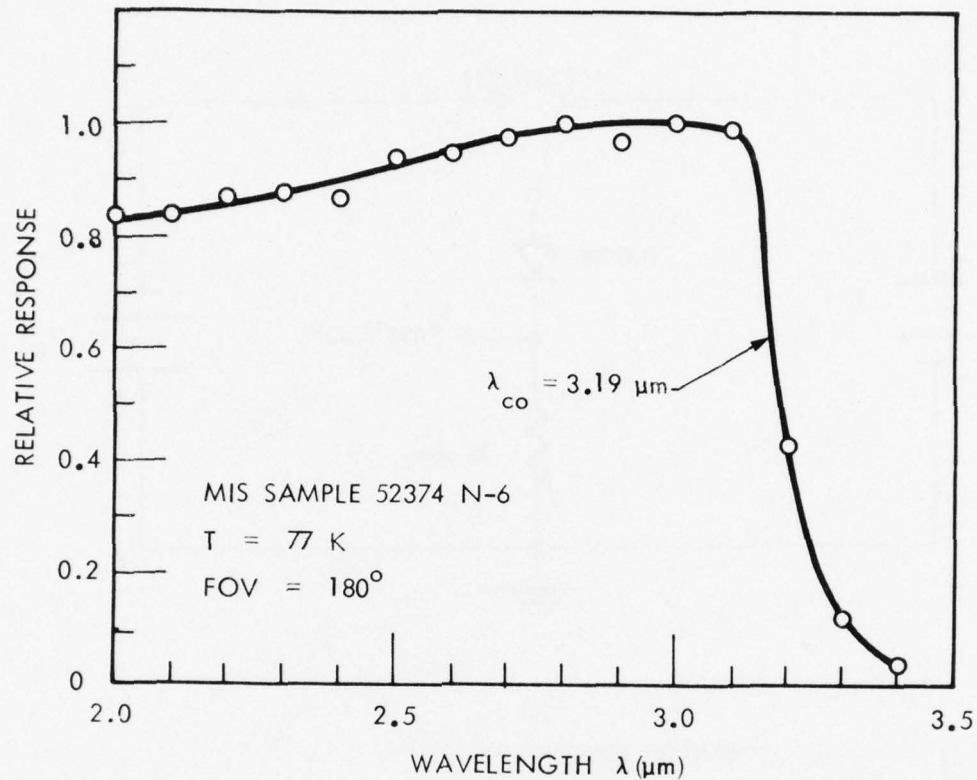


Figure 10. Typical Spectral Response Curve Using MIS

injected minority carriers. The reverse current is limited to a constant value of I_R by the applied reverse bias V_R and series resistance of the circuit. After a time t_s , the electron density at the junction is near zero. The subsequent exponential decay phase of current, determined by diffusion and recombination on the p-side, establishes the normal reverse current, I_{sat} , as shown in the lower portion of Figure 11.

The minority carrier lifetime can be calculated by either of these reverse current phases. However, the constant current phase lends itself to an easier calculation, is less susceptible to trapping effects than the decay phase, and the time period is easier to accurately determine.

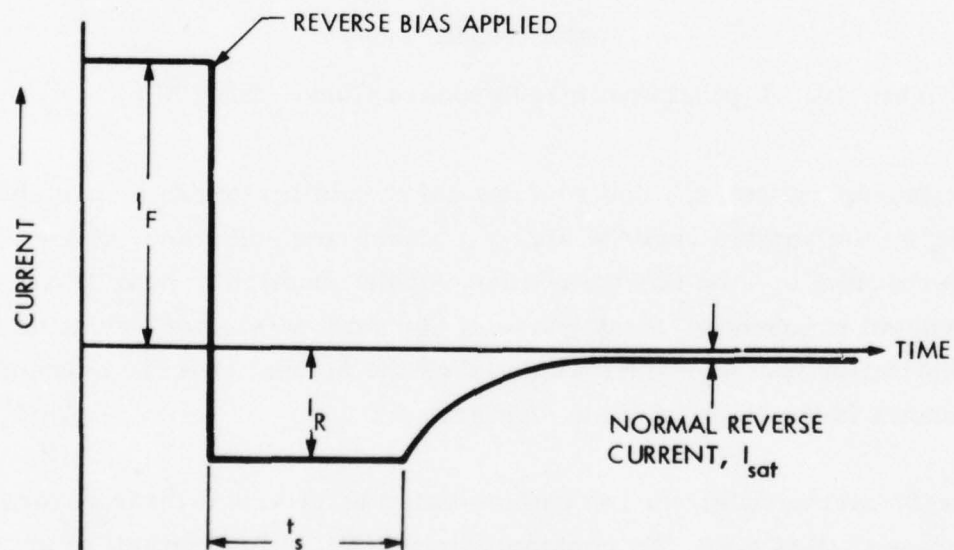
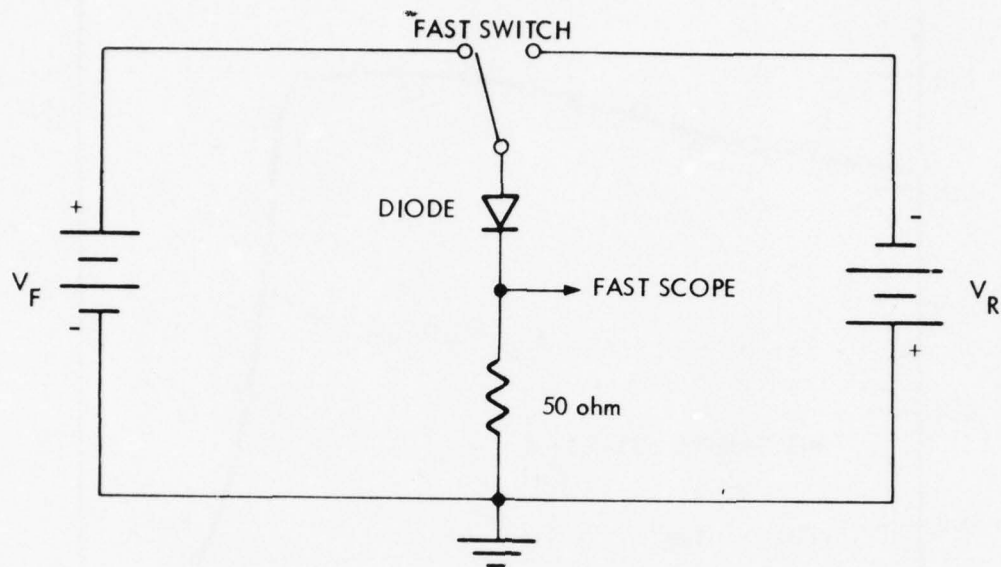


Figure 11. Schematic of Diode Reverse Recovery Technique

5.4.2 Experimental Apparatus

Experimentally, the reverse recovery measurement system is quite simple. The forward and reverse voltages are supplied by a Tektronix 508 pulse generator with forward-to-reverse transition time of less than 10 ns. The positive and negative voltage levels can be individually controlled to vary the ratio of I_F/I_R . A 10 k ohm variable resistor is used in series with the diode to allow small current levels to be used. Actual waveform measurements are taken across a 50-ohm resistor. The resistors are housed in a shielded box, with short coaxial cables extending to the test dewar. All leads are kept short to avoid ringing in the circuit, and the shielded box is plugged directly into the oscilloscope. The scope is a Tektronix 7603 with a 100-MHz bandwidth. Storage times down to about 20 nsec have been measured reliably with this system. A diagram of the circuit is shown in Figure 12.

In operation, the ratio I_F/I_R is varied by holding I_F fixed and changing I_R . This is because the number of injected carriers, determined by I_F , can affect the lifetime. See Section 6.2.3.

5.4.3 Interpretation of Data

There are many methods described in the literature for extracting minority carrier lifetime from the measured reverse recovery parameters (t_s , I_F , I_R), defined in Figure 11. Several of them treat special cases, such as an abrupt junction with infinite base width, and come up with easily evaluated expressions for lifetime. Others provide a more general treatment, but the mathematics becomes prohibitively complicated. A partial list of references, with the device model assumed for each, is given in Appendix A. The methods most applicable for our purposes are as follows:

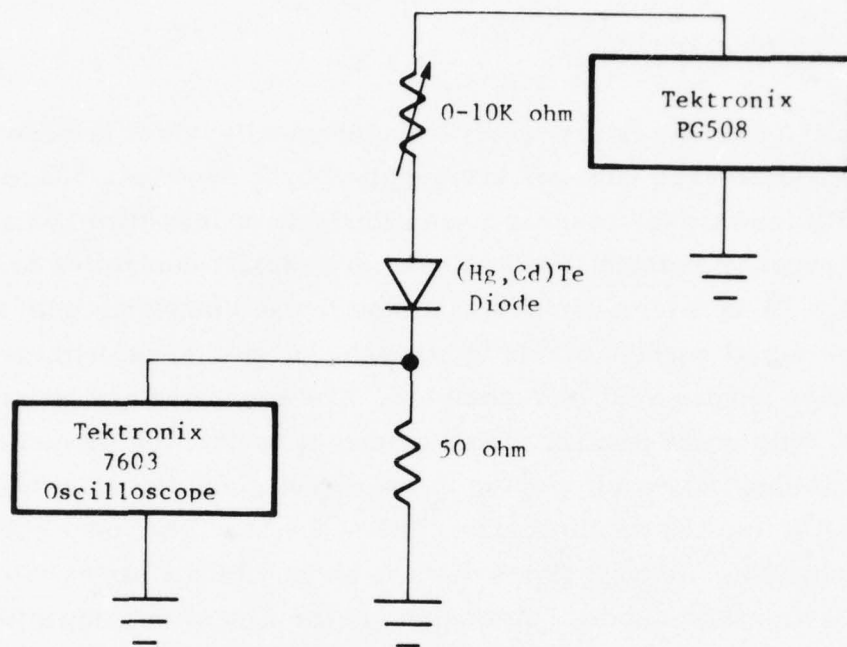


Figure 12. Reverse Recovery Circuit

- (1) From Kingston, ⁽²⁸⁾ Lax and Neustadter, ⁽²⁹⁾ and others. For the case of an abrupt junction, with a very thick base region ($W \gg L_e$), both papers derive the following expression:

$$\text{erf} \sqrt{\frac{t_s}{\tau_e}} = \frac{1}{1 + \frac{I_R}{I_F}} \quad (41)$$

This method requires only a single reverse recovery curve to determine the lifetime.

28. R. H. Kingston, Proc. IRE 42, 829 (1954).

29. B. Lax and S. F. Neustadter, J. Appl. Phys. 25, 1148 (1954).

- (2) Kuno⁽³⁰⁾ does not assume an abrupt junction, nor does he assume a specific base width (thickness of the lightly doped side of the junction). His expression is:

$$t_s = \tau_e \ln \left(1 + \frac{I_F}{I_R}\right) + \tau_e \ln \left(1 + \frac{\tau_R}{\tau_e}\right) \quad (42)$$

Here, τ_R is a parameter defined by the relation $Q(t_s) = I_R \tau_R$, where $Q(t_s)$ is the charge remaining in the base region at the end of the constant-current phase. τ_R has no physical significance as a lifetime, and is assumed by Kuno to be a constant. Kuno's method is to plot t_s versus $\ln(1 + \frac{I_F}{I_R})$; the slope is then τ_e . This requires a series of reverse recovery measurements to be made, over a range of $\frac{I_F}{I_R}$ ratios.

- (3) Moll, Krakauer, Shen⁽³¹⁾ for narrow-base graded junctions) and Moll, Hamilton⁽³²⁾ (for p-i-n junctions), both derive the approximation:

$$t_s = \tau_e \ln \left(1 + \frac{I_F}{I_R}\right) \quad (43)$$

The assumption used is that the field associated with the graded junction sweeps out all the injected carriers by the end of the storage period. This is equivalent to $Q(\tau_s) = 0$ in Kuno's formulation; in that case, Equation 42 reduces to Equation 40. As with method (1), this method requires just one reverse recovery measurement to determine the lifetime.

30. H. J. Kuno, IEEE Trans. on Electron Dev., ED11, 8 (1964).

31. J. L. Moll, S. Krakauer and R. Shen, Proc. IRE 50, 43 (1962).

32. J. L. Moll and S. A. Hamilton, Proc. IEEE 57, 1250 (1969).

Each of the above methods involves some questionable assumptions. Method (1), for instance, is for the case of an ideal abrupt junction. However, C-V data from these junctions usually show deviation from a linear $1/C^2$ versus V plot, indicating that the junction is not abrupt. Method (1) also assumes a lightly doped region of thickness W, so that $W \gg L_e$, the minority carrier diffusion length. While this assumption is reasonable for diodes fabricated on planks, it does not hold for BITS arrays.

Method (2) depends on the assumption that τ_R , a defined quantity is a constant independent of I_F/I_R . Any variation of τ_R with I_F/I_R will change the slope of a "Kuno plot," and hence the calculated lifetime. Kuno gives no physical explanation for the linear relationship between $Q(t_s)$ and I_R , but rather points to experimental fits of t_s versus $\ln(1 + I_F/I_R)$, which do follow Equation 42. Our data, also, have given consistently good linear fits well within experimental errors (see Figure 13). One disadvantage of this method is the number of reverse recovery curves which must be recorded to get a reliable "Kuno plot". Error bars in the resulting lifetime can also be large, because slopes are involved, rather than measured values.

Method (3) has a major problem: it simply does not fit the measured data. A plot of t_s versus $\ln(1 + I_F/I_R)$ does not pass through the origin, and the difference is significantly greater than experimental error. The assumption that all the injected charge is swept from the base by time t_s is apparently not valid for our junctions. Using Kuno's formulation, the experimental values we get from "Kuno plots" correspond to $\tau_e^R = 0.5$ to 2.0 , and not to $\tau_R = 0$, as method (3) assumes.

For comparison purposes, the three expressions were used to evaluate reverse recovery data from a 4- μm diode. (See Table 4.) Note that methods (1) and (3) calculate lifetimes for each data point, while a single lifetime is determined by method (2). The Kuno plot for method (2) is shown in Figure

Table 4. Lifetime Evaluated by Three Methods, from Reverse Recovery Data on 4- μ m diode 20475 S43 D3 No. 2, at 126K. I_F and I_R in Units of mV across 50 ohms

I_F (mV)	I_R (mV)	t_s (nsec)	LIFETIME, τ_e (nsec)		
			Kingston (1)	Kuno (2)	Moll (3)
150	55	120	196	162	91
150	40	155	197		99
150	31	190	202		108
150	23	235	207		116
150	15.5	295	210		130
150	8	385	202		129

13; the fit to theory is good. The range in lifetimes calculated by Equation 41 is well within experimental error, while the increase in lifetime with I_F/I_R seen for Equation 43 is rather large.

Of the three methods, Kuno's is felt to be most indicative of the true minority carrier lifetime. This is partly because inclusion of the parameter τ_R corresponds to large fields across the base region, quickly sweeping out the injected carriers, as in model (3); larger values of τ_R can model an abrupt junction in which a significant portion of the injected charge remains at $t = t_s$. Our n^+ on p junctions are neither ideal abrupt nor narrow-base graded, but somewhere intermediate. Kuno's method calculates a lifetime between these two special cases, where we expect the true lifetime to lie. The good fit of data to theory, over a range of I_F/I_R , also makes us more confident of the accuracy of Kuno's method.

However, the advantages of Kuno's method are offset by the large amount of data which must be taken to construct a Kuno plot. Kingston's method requires one reverse recovery curve; Kuno's requires about five to determine the lifetime. Kuno's method rapidly becomes impractical when testing each element of a large array for uniformity, while varying also the temperature and injection level.

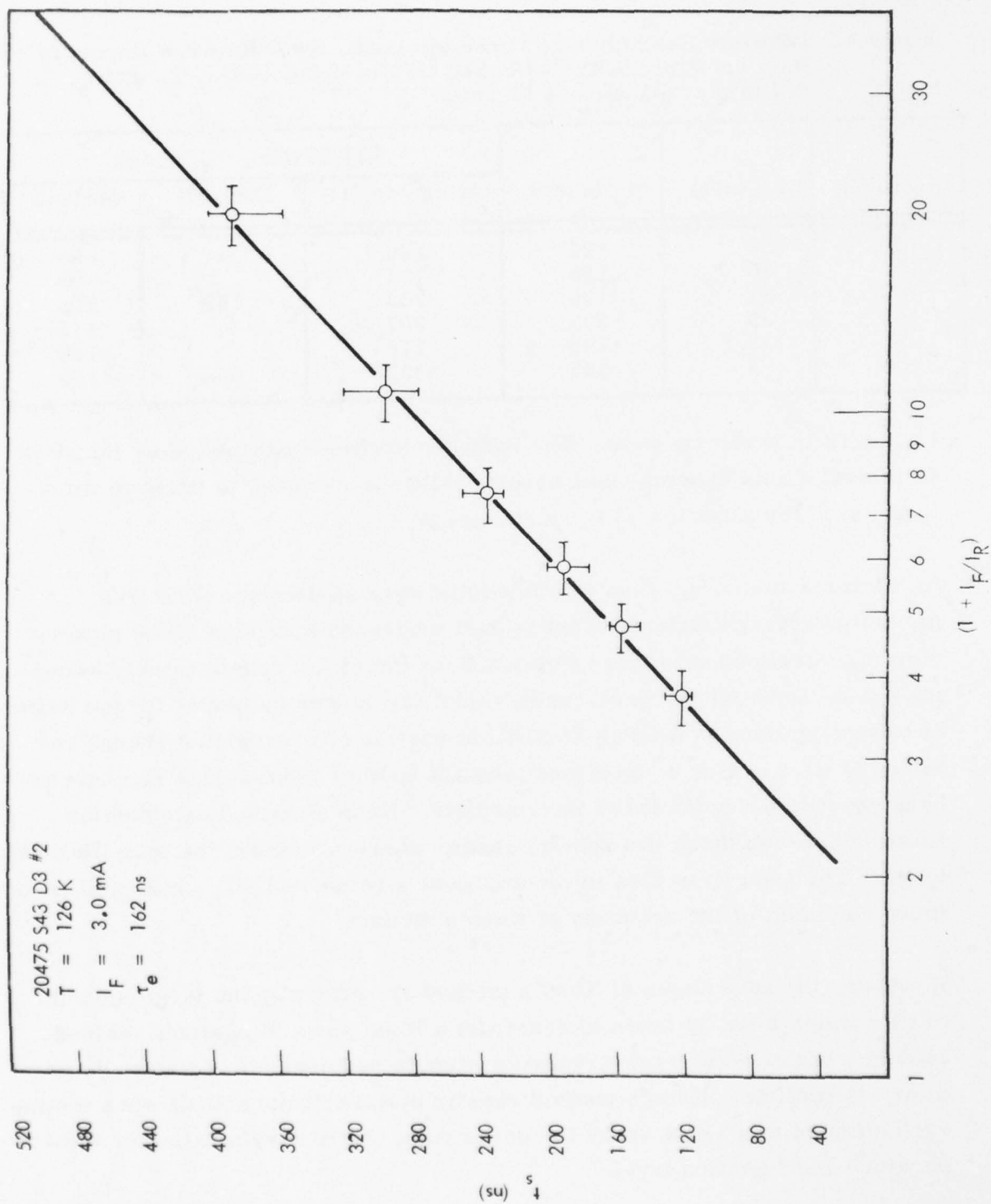


Figure 13. Kuno Plot for Reverse Recovery Data at 126K

Kingston's method is, therefore, significantly more desirable on the basis of throughput, while not greatly inferior to Kuno's in terms of accuracy. For example, Kuno and Kingston lifetimes are compared over a wide range of temperatures in Section 6.2. The temperature dependence of lifetime is essentially the same, and the difference in magnitude is less than a factor of two. These relationships hold in general for all the lifetimes tested during the program: Kingston lifetime is larger than Kuno, by up to a factor of two, and the temperature dependence is about the same. Because a great number of lifetime measurements had to be made during the program, Kingston's method was, therefore, used for the bulk of them. In interpreting the lifetime data, it must only be kept in mind that the Kingston lifetime is larger than the true minority carrier lifetime, by up to a factor of two. Kuno lifetime should be used when quoting absolute numbers for the lifetime.

5.4.4 Injected Carrier Density

An inherent feature of the reverse recovery technique is injection of a finite number of excess carriers into the material being measured. Because the diode at zero bias operates under very low injection levels, and the simple lifetime expressions assume negligible excess carriers, the injected carrier density presents a complication in interpreting the data. On the other hand, the variation of lifetime with injection level provides additional information about the recombination mechanism. Ideally, the injection level would be variable over the full range from negligible excess carriers, satisfying the low injection assumptions, to very high excess carrier densities. In practice, good lifetime data are obtainable over a restricted, but useful, range of injected carrier densities.

The two useful measures of injection level are the injected current density, easily and accurately obtained from the diode forward current and junction area ($J_F = I_F/A$), and the actual number density of excess injected carriers. The excess carrier density is given approximately by:

$$\Delta n \approx \frac{I_F \tau_e}{2AqL_e} \quad (44)$$

Inaccuracies arise because Δn varies with distance from the junction, making some sort of averaging necessary. τ_e and L_e also depend on the injection level, so that the calculated Δn should be considered only approximately correct.

5.5 R_O A VERSUS TEMPERATURE MEASUREMENT

Variable temperature dewars for the measurements were built by Andonian Cryogenics to Honeywell specifications. Cooling is provided by a reservoir of liquid nitrogen; the flow rate of liquid can be throttled to control the cooling rate of the specimen pedestal. This allows very rapid cooldown, but still long hold times. Resistive heaters are used in conjunction with a Honeywell-built temperature controller to set and maintain the desired temperature. Temperature measurement is done by Lakeshore Cryotronics AD-500 calibrated diode temperature sensors. The dewar can be used over the full temperature range from 80K to above room temperature. Sixty-one pin electrical connectors provide access to the test devices, and allow testing of large arrays (such as BITS). Internal wiring is done with grounded mini-coax cable to minimize stray capacitance (the dewar is also used for MIS).

Zero bias resistances are generally measured from diode I-V curves, using Tektronix 576 or 577 curve tracers. For measurement of very high R_O values, the curve tracers are not sensitive enough, and an alternate method is used. A small amplitude ac voltage is applied across the device, and the resulting current measured with a PAR 181 trans-impedance preamp and PAR 124A lock-in amplifier. By superimposing the ac signal on a slowly varying voltage ramp, and connecting the voltage and current signals to an

x-y recorder, the I-V characteristics can be traced out, and R_o determined.

5.6 EBIC TECHNIQUE

The Electron Beam Induced Current (EBIC) mode of operating the Scanning Electron Microscope (SEM) can be used to determine the minority carrier diffusion length in a very localized region near a p-n junction. It can, therefore, be used to measure diffusion length on standard diodes, without resorting to special device structures such as BITS (Section 5.7). The excellent resolution of the SEM also allows detailed study of the spatial variation of diffusion length.

We have used the EBIC line scan technique,⁽³³⁾ which uses the electron beam of the SEM to generate carriers outside a p-n junction, and a sensitive current amplifier to measure the current as these carriers diffuse to the junction. As the beam is moved away from the junction edge, the current decreases in a manner characteristic of the minority carrier diffusion length, allowing L_e to be measured.

The relationship between the collected current I and the lateral distance from the junction edge z on the p-side of the junction is given by:

$$I = I_o e^{-z/L_e} \quad (45)$$

where I_o is a constant and L_e is the minority carrier (electron) diffusion length on the p-side. This relationship is valid for negligible surface

33. See, for example, W. H. Hackett, Jr., R. H. Saul, R. W. Dixon, and G. W. Kammlott, J. Appl. Phys. 43, 2857 (1972).

recombination (i. e., for surface recombination velocity $s \ll \frac{L_e}{\tau_e}$) and for a point-source generation of minority carriers. Common values of L_e/τ_e for p-type (Hg, Cd)Te are of the order of $20 \mu\text{m}/200 \text{ nsec} = 10^4 \text{ cm/sec}$. Surface recombination velocities, on the other hand, have been measured on MIS devices in the range of 10-1000 cm/sec. Surface effects are, therefore, expected to be small. The finite extent of the carrier generation region is more important, especially very near the junction edge. A variation from the above expression is seen for $z < 5 \mu\text{m}$ from the junction; however, plotting $\log I$ versus z further from the junction results in excellent linear fits for determining L_e .

The experimental apparatus consists of an ISI Super II SEM, with a GW Electronics Model 103 specimen current amplifier. The electron beam is set to scan across the junction edge, and the data recorded on an x-y recorder. The x-direction corresponds to beam displacement, while y records the specimen current. Traces taken both left-to-right and right-to-left across the junction edge show negligible hysteresis on the recorder.

The zero of current is calibrated by moving the beam far away from the junction of interest. Absolute calibration of the current magnitude is not necessary, as only relative magnitude is needed for determining L_e . The distance scale is calibrated from known dimensions on the array being tested.

Our SEM has a variable temperature cold stage built by Air Products. Cooling is provided by a Joule-Thompson apparatus, as low as 80K. Resistive heating raises the temperature to 300K or above. Temperature is monitored by a Copper-constantan thermocouple, accurate to about 3K. For making variable-temperature L_e measurements, the device was cooled to 80K, and then allowed to slowly warm to room temperature, over a period of several hours.

5.7 THE BACKSIDE-ILLUMINATED TAPERED STRUCTURE (BITS)

The Backside-Illuminated Tapered Structure (BITS) was developed at Honeywell specifically to measure the minority-carrier diffusion length L_e in p-type (Hg, Cd)Te. It is shown schematically in Figure 14.

The principle of operation is quite simple: infrared radiation from some source passes through an IR-transmitting substrate and epoxy layer, and is absorbed very near the back surface of the $\text{Hg}_{1-x}\text{Cd}_x\text{Te}$ sample. As the absorption coefficient is about $5 \times 10^3 \text{ cm}^{-1}$ in $\text{Hg}_{1-x}\text{Cd}_x\text{Te}$, absorption will take place within about $5 \mu\text{m}$ of the surface. The carriers so generated diffuse through the bulk to the front surface, where they are collected and read out as a signal current. In the BITS structures fabricated to date, ion-implanted n^+ -on-p diodes perform the charge collection; other methods, such as MIS devices, could also be used. When the thickness of the (Hg, Cd)Te sample is less than a diffusion length, nearly all generated charges will diffuse and be collected as signal. The signal current (I_{sig}) should be relatively constant in this region. Where the sample thickness is greater than a diffusion length, however, a significant proportion of the carriers will recombine before reaching the diode junctions. As the thickness increases, therefore, this signal is expected to drop. By looking at the signal current versus thickness of the sample, one can directly determine the diffusion length.

The BITS method of determining diffusion length has an inherent advantage over the EBIC method (described in Section 5.6) in that the effects of surface recombination are eliminated. Whereas front-surface scans look at lateral diffusion of carriers, and may be influenced by surface effects, the BITS method collects carriers before they reach the surface. The disadvantage of the BITS method is that it requires fairly difficult device fabrication steps.

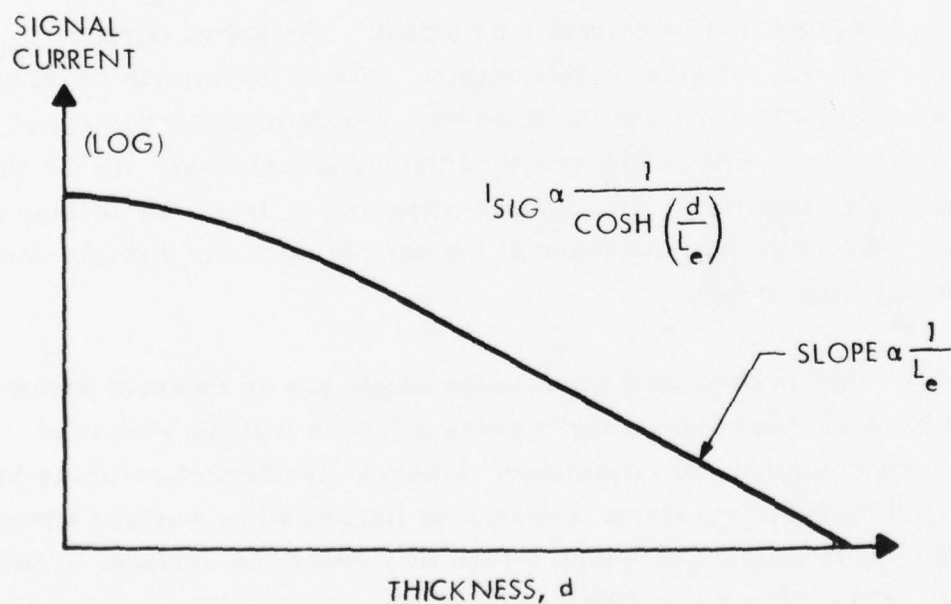
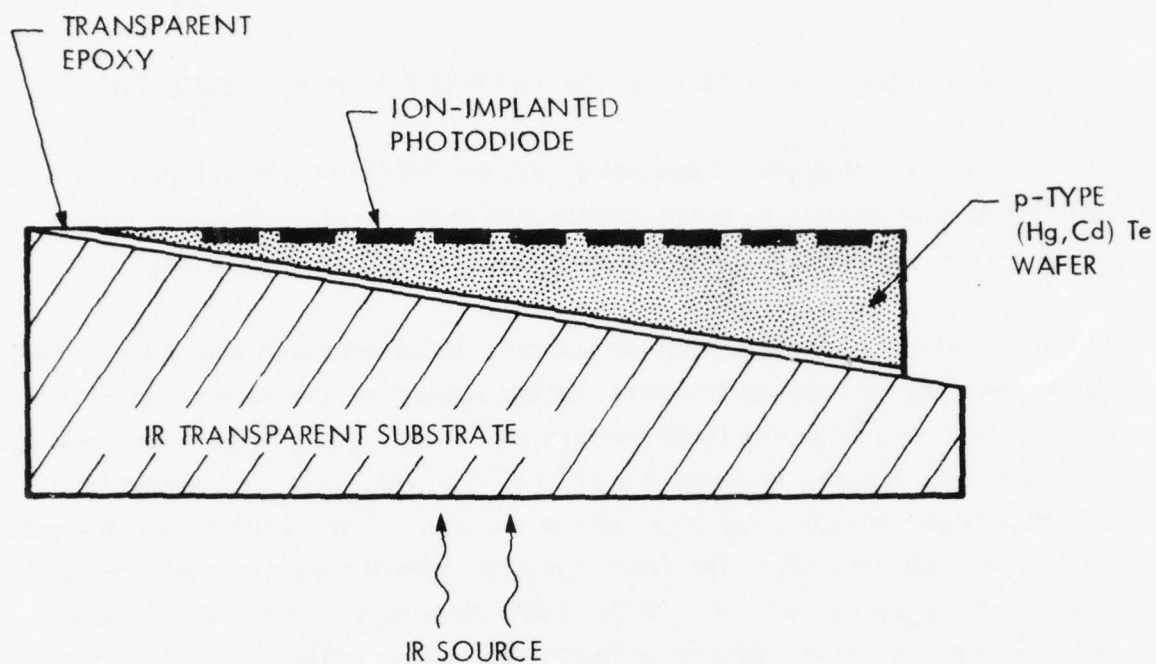


Figure 14. The Backside-Illuminated Tapered Structure (BITS)

One can show quite simply that the signal current for a n^+ -p junction in the BITS configuration is given by

$$I_{\text{sig}} = \frac{q Q_{\text{sig}} A_{\text{eff}}}{\cosh (d/L_e)} \quad (46)$$

where Q_{sig} is the signal photon flux at the back surface, A_{eff} is the effective collection area of a given junction, and d is the thickness of the p-region between the n^+ -p junction and the back surface.

The experimental data necessary to determine L_e are the signal current at each diode versus the base thickness under the diode. Base thickness is profiled during fabrication of the structure, using the micrometer stage on a Unitron or Reichert microscope. For looking at the wafer edge, the microscope is first focused on the top surface, then on the epoxy under the (Hg, Cd)Te; the difference in micrometer readings gives the thickness. These readings are repeated at each element of the array to get the thickness profile.

A uniform source of signal radiation is needed in order to properly determine diffusion length. The source is a 1000K IR Industries blackbody, chopped at a frequency of 1 kHz. The dewar containing the BITS array is mounted far enough away from the blackbody to ensure a uniform level of radiation across the array (about 15 cm). The signal current is first converted to a voltage using a PAR 181 transimpedance preamp, then measured with a wave analyzer. The reference frequency is supplied by the chopper. Signal levels were generally strong enough so that signal integration was not necessary.

Once the signal current for all elements was recorded, the thickness profile was used to plot $\log (I_{\text{sig}})$ versus thickness. From this plot, L_e was determined by fitting Equation 46.

SECTION 6

RESULTS

In this section, we present our data on $(N_A - N_D)$, on minority carrier lifetime as measured by the diode reverse recovery technique, and on minority carrier diffusion length measured by BITS and EBIC. The lifetime data is given versus position on a wafer to demonstrate uniformity, versus temperature and carrier injection level to provide a basis for identifying the recombination mechanisms and versus hole and acceptor concentrations to identify possible device improvements.

The diffusion length results are given to compare BITS and EBIC techniques and are presented as functions of temperature, carrier concentration and position as was the lifetime data. The minority carrier mobility is determined from the τ_e and L_e measurements. R_0A is given as a function of temperature to determine the limiting leakage mechanism and versus carrier concentration to provide a basis for selecting parameters for improved devices.

6.1 CARRIER CONCENTRATION

The primary technique used to determine carrier concentration under this contract has been Hall measurements as detailed in Section 5.1. Several samples have also been measured using the MIS technique as detailed in Section 5.3. Both of these techniques give the hole concentration $p = (N_A - N_D)$. In Section 3, we indicated that the residual donor concentration in crystal 52374 is $\sim 4 \times 10^{15} \text{ cm}^{-3}$ determined by Hall measurements on four samples after annealing to remove stoichiometric acceptors. We assume that this donor concentration exists in all our p-type samples and add it to

the measured value of $(N_A - N_D)$ to get the acceptor concentration, N_A . Table 5 lists the 11 planks of $Hg_{1-x}Cd_xTe$ which were made into devices and measured. The first column of the table lists sample numbers which will be found on subsequent figures. The second column lists the crystal and plank numbers. The third column gives the composition measured by density. The fourth column gives the technique by which the crystal was grown; Q/A means quench-anneal while ZL means zone-leveled. The fifth column lists the annealing conditions for those samples which were annealed. The sixth column lists the hole concentration determined by Hall measurements; if a second number is listed it is from MIS measurements. The last column is the acceptor concentration derived by adding the donor concentration $4 \times 10^{15} \text{ cm}^{-3}$, to the $(N_A - N_D)$ value in column six. We use the MIS value rather than the Hall value because MIS devices are made on the surface near to where diodes are later made. We could just as well have averaged the results because the differences are probably due to scatter in both the Hall and MIS data rather than to concentration gradients. The only serious discrepancy is sample 8 and for that one the Hall value was interpolated from measurements on nearby samples.

6.2 MINORITY CARRIER LIFETIME

Of the lifetime measurement methods investigated during this program, diode reverse recovery proved to be the easiest, most reliable, and most widely applicable. Consequently, the measurements reported in this subsection were all obtained by reverse recovery. Characteristics of all diode arrays used in this study are listed in Table 6. It also compares the composition measured by density with that determined from λ_{co} on MIS devices and diodes.

Table 5. Hole and Acceptor Concentrations of the Samples Used for Diodes

Sample (Number)	Material (Crystal, Plank)	Compo- sition (x)	Growth Tech- nique	Anneal (Days, °C)	Hole Concen- tration (10^{15} cm^{-3})	Acceptor Concen- tration (10^{15} cm^{-3})
1	52374, 04	0.392	Q/A	26, 304	1.0, 0.9	4.9
2	52374, P4	0.390	Q/A	26, 304	1.4	5.4
3	96V, K5	0.395	ZL	30, 352	4.3, 4.3	8.3
4	96V, K3	0.388	ZL	30, 352	4.3	8.3
5	52374, N9	0.384	Q/A	62, 375	8.3, 7	11
6	52374, L4	0.394	Q/A	None	16	20
7	52374, 02	0.395	Q/A	None	17.5	21.5
8	52374, N6	0.384	Q/A	None	18, 10	14
9	52374, L6	0.380	Q/A	None	19	23
10	52374, J4	0.393	Q/A	Cu, 7, 450	22.6	26.6
11	52374, K5	0.389	Q/A	Cu, 7, 450	28	32

Table 6. Summary of Diode Arrays

Sample	Composition			No. of Elements	Area (mil) ²	τ_e at 295K (10 ⁻⁸ sec)
Number	Density	MIS	Diode			
1	0.392	0.395		22	varied	100
2	0.390			15	9.5x10.5	105
3	0.395		0.377	16	9.5x10.5	29
4	0.388		0.369	3	9.5x10.5	-
5	0.384	0.389		22	varied	4
6	0.394	0.394		46	varied	-
7	0.395	0.393		19	4x6(BITS)	5.5
8	0.384	0.386	0.375	19	9.5x10.5	13
9	0.380	0.399	0.377	46	varied	7
10	0.393		0.388	13	9.5x10.5	4.6
11	0.389		0.376	19	9.5x10.5	3

6.2.1 Lifetime versus Temperature

Measurements of minority carrier lifetime were carried out from 77K to 300K using the variable temperature apparatus described in Section 5.5. The data are presented in Figure 15, 16, and 17 for samples with three different doping levels. For more heavily doped samples, the lifetimes at low temperatures were too short to measure with our apparatus.

In each case, comparison with the calculated radiative lifetime shows the lifetime is not limited by this mechanism. Measured lifetimes have significantly lower magnitudes and also a different temperature dependence. A much better fit to the temperature dependence is given by the simple Shockley-Read model, also shown in Figures 15, 16, and 17. This modeling is explained and elaborated in Section 7.1. The calculated Auger lifetime, of course, is too large in magnitude to fit on the graphs of τ_e versus $10^3/T$.

6.2.2 Lifetime versus Carrier Concentration

A major goal of the program was to determine the dependence of lifetime on p-type carrier concentration in order to optimize the n+-on-p photodiode structure. Lifetime has been evaluated both as a function of the hole concentration ($N_A - N_D$), and of the acceptor concentration (N_A). The distinction is important, as explained below.

Material samples with several different doping levels were prepared as described in Section 3. The effective carrier densities ($N_A - N_D$) were determined by Hall measurements, and in some cases by MIS. Ion-implanted n+ on p junction arrays were then formed and evaluated. Table 6 provides pertinent information on the devices. Each error bar in the accompanying figures represents the range of lifetime measured on a multi-element array, and is not intended to depict experimental error. The data were evaluated, using Kingston's method, with a forward current $I_F = 10$ mA, and a forward to reverse current ratio of about 5:1.

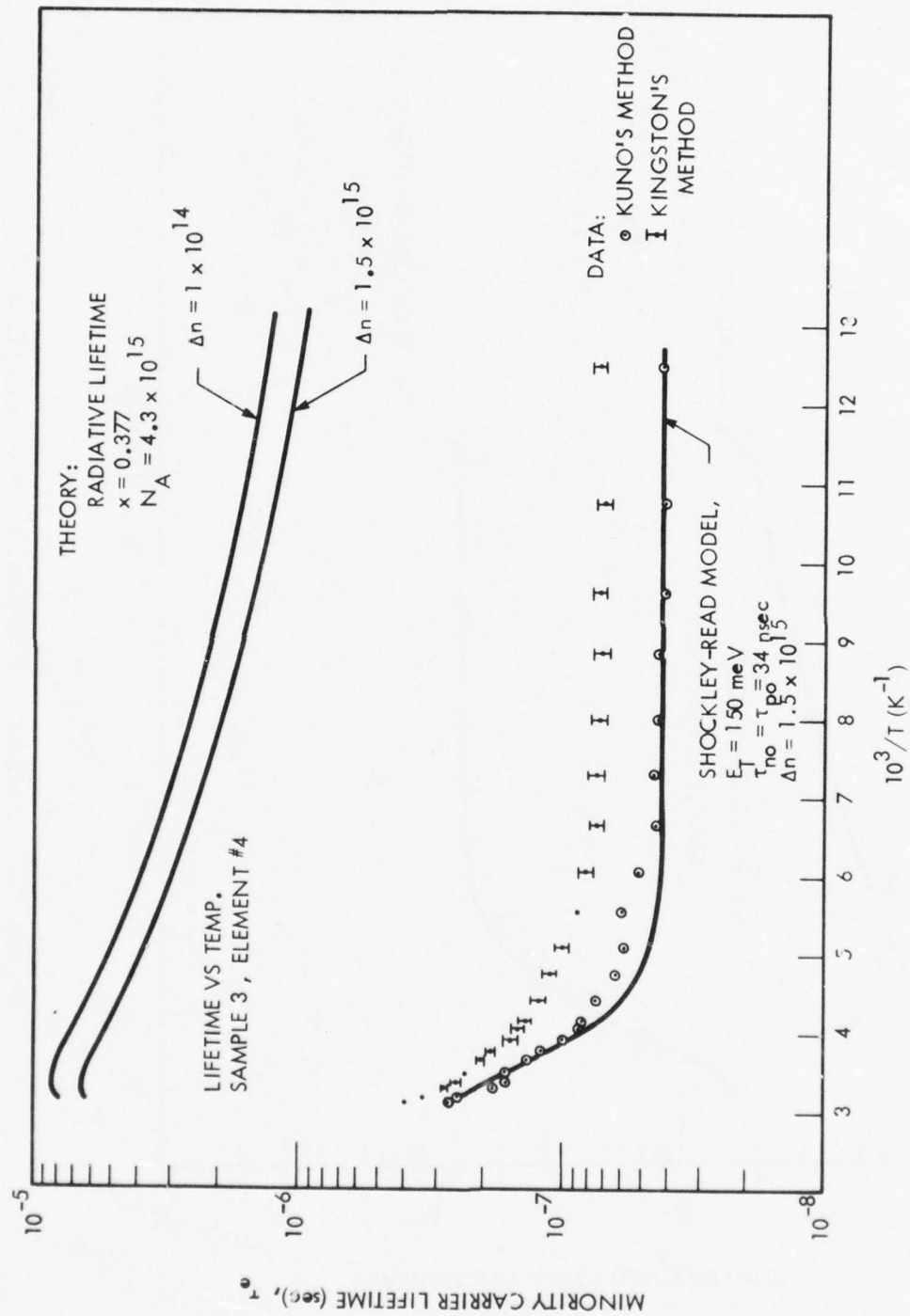


Figure 15. Minority Carrier Lifetime versus Reciprocal Temperature

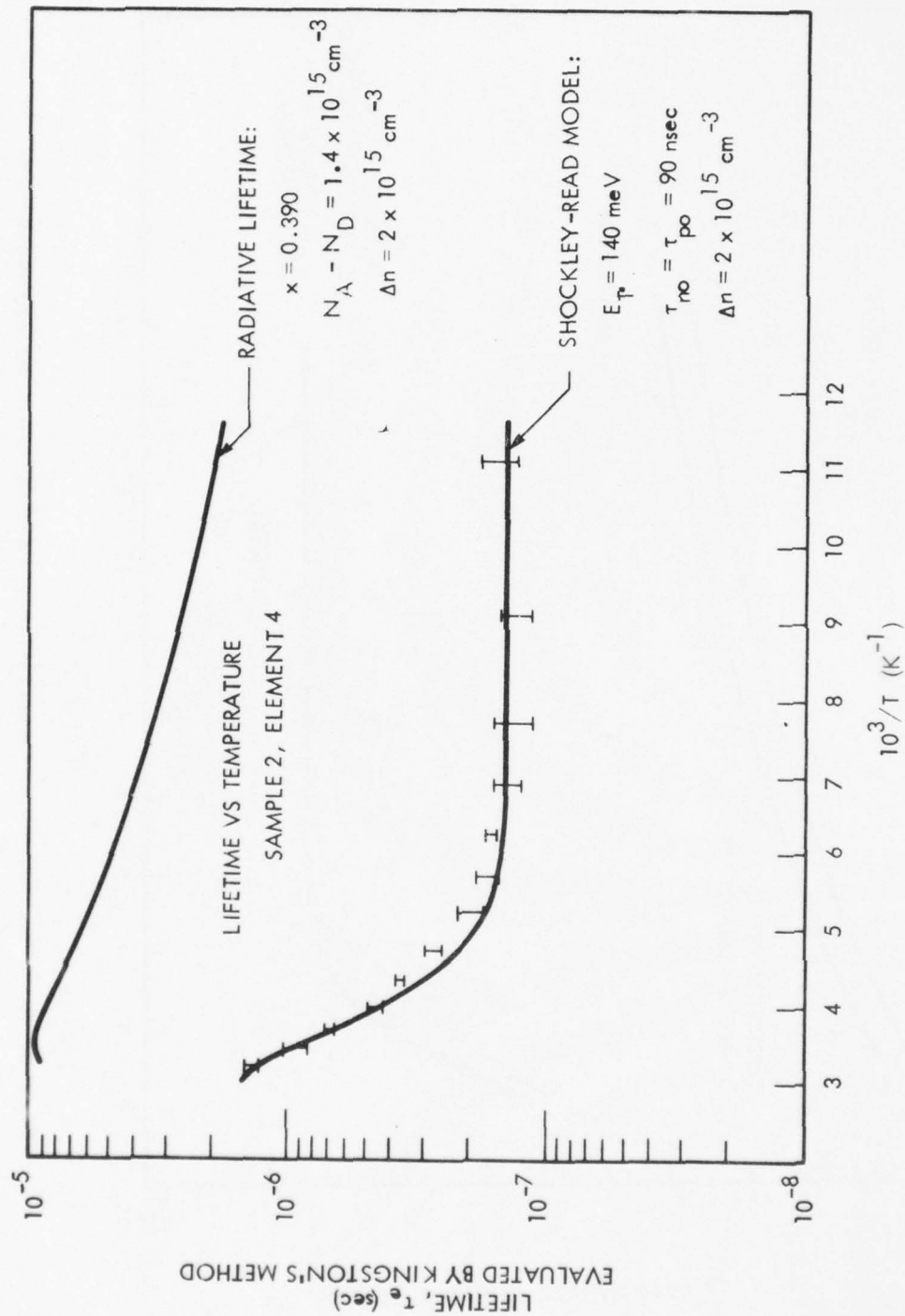


Figure 16. Lifetime by Kingston Method, Sample 2

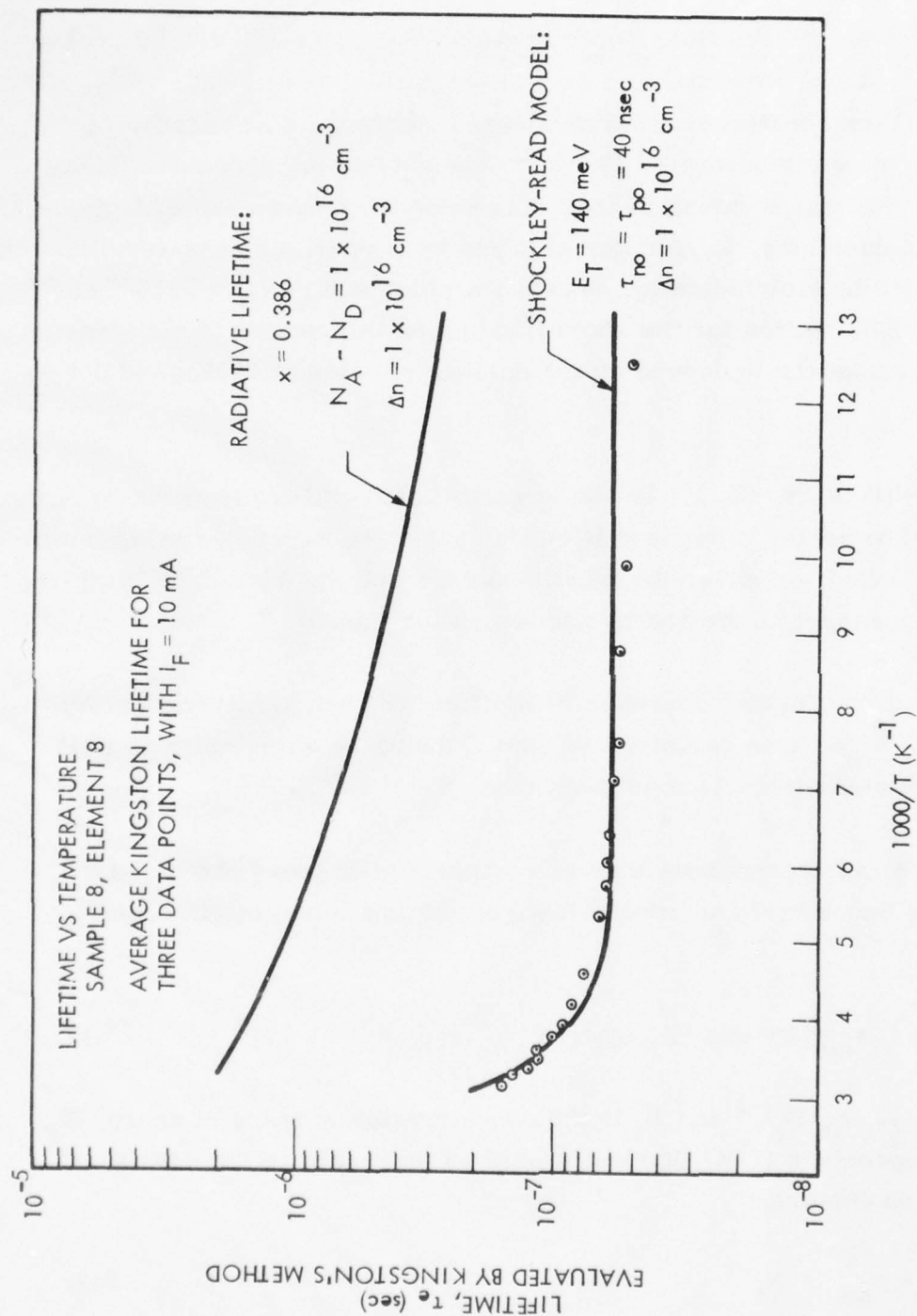


Figure 17. Lifetime by Kingston Method, Sample 8

6.2.2.1 Lifetime versus Hole Concentration -- Figures 18, 19, 20 present lifetime versus hole concentration data at temperatures of 295K, 193K, and 77K. For all temperatures, lifetime shows a decrease with increasing $N_A - N_D$. At room temperature, lifetime depends on hole concentration as $(N_A - N_D)^{-1}$. No major variation from this behavior is seen for Q/A material doped by stoichiometry, Q/A material doped by copper, or zone-levelled material doped by stoichiometry, except the point at $N_A - N_D = 7 \times 10^{15} \text{ cm}^{-3}$ (sample 5). The reason for the short lifetime on this device is not clear. Lifetime thus appears to depend on the number of holes at 295K, and not on their source.

At 193K, the fit to $(N_A - N_D)^{-1}$ is not as good, but is still reasonable within experimental accuracy. Because lifetime decreases with decreasing temperature and increasing doping, the most heavily doped samples have lifetimes too short to measure (indicated by arrows on the figure).

At 77K, due to the further decrease of lifetime with temperature, the dependence on $N_A - N_D$ is less certain. A general decrease with doping is still seen, but the dependence is less steep than $(N_A - N_D)^{-1}$.

The experimental dependences may be compared with those predicted by theory. For Shockley-Read recombination, the low injection lifetime is given by

$$\tau = \tau_{no} [1 + \exp (E_F - E_t)/kT] \quad (47)$$

where $\tau_{no} = (\sigma_e v_{th} N_t)^{-1}$ and N_t is the concentration of traps at energy E_t . The low-temperature (77K) lifetime should go inversely as the density of recombination centers,

$$\tau = \tau_{no} \propto N_t^{-1} \quad (48)$$

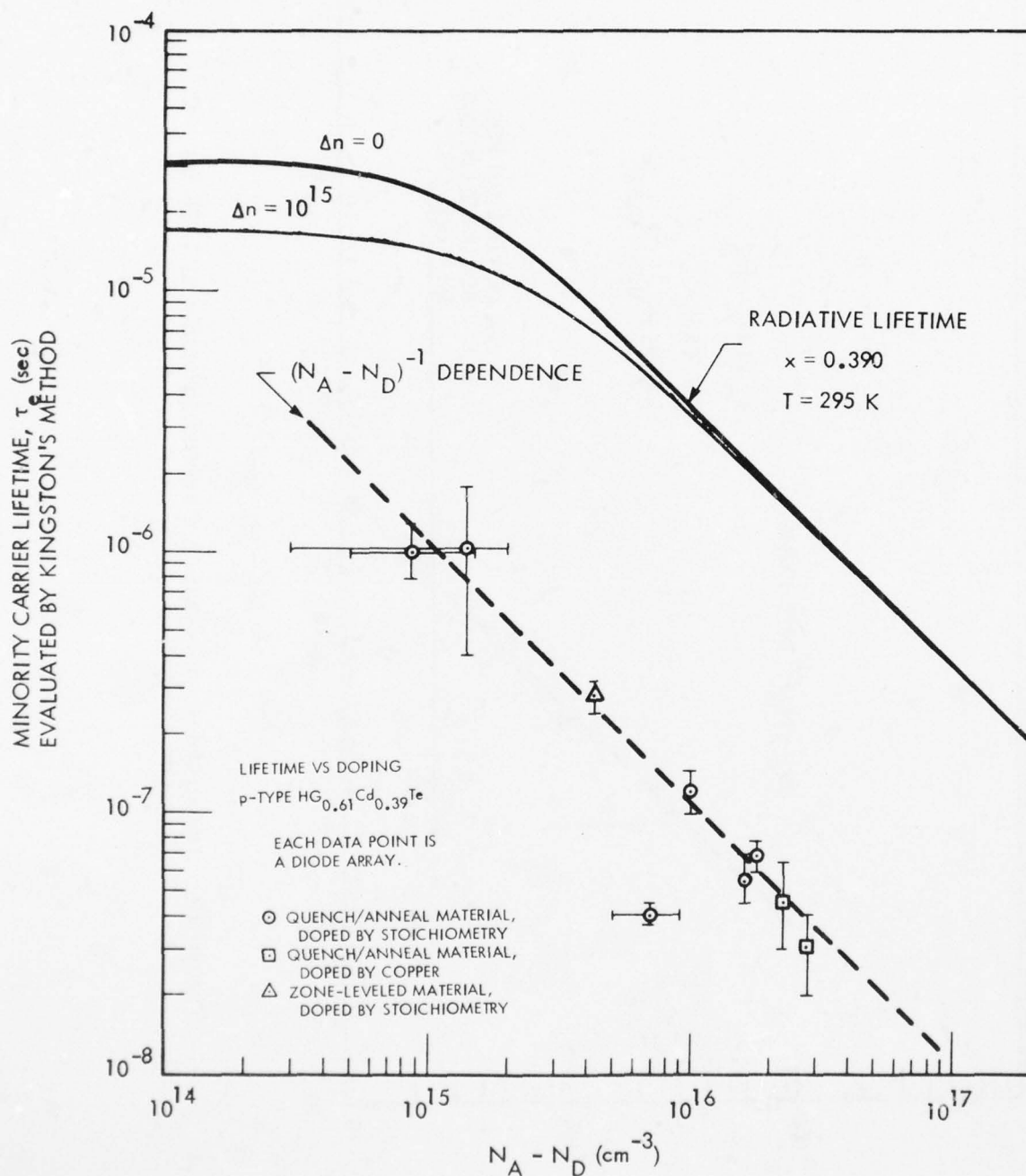


Figure 18. Dependence of Minority Carrier Lifetime at 295K on Hole Concentration

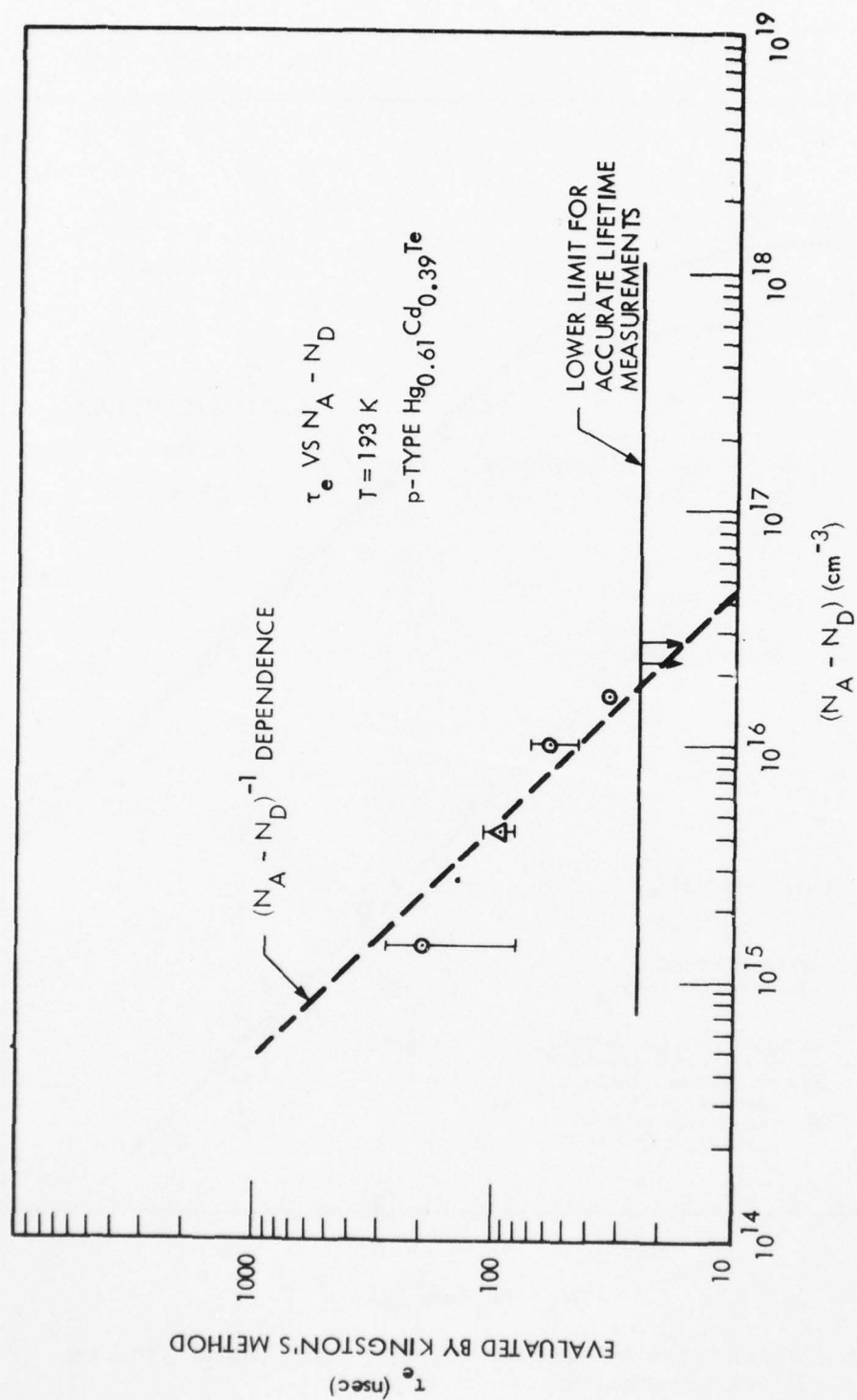


Figure 19. Dependence of Minority Carrier Lifetime at 193K on Hole Concentration

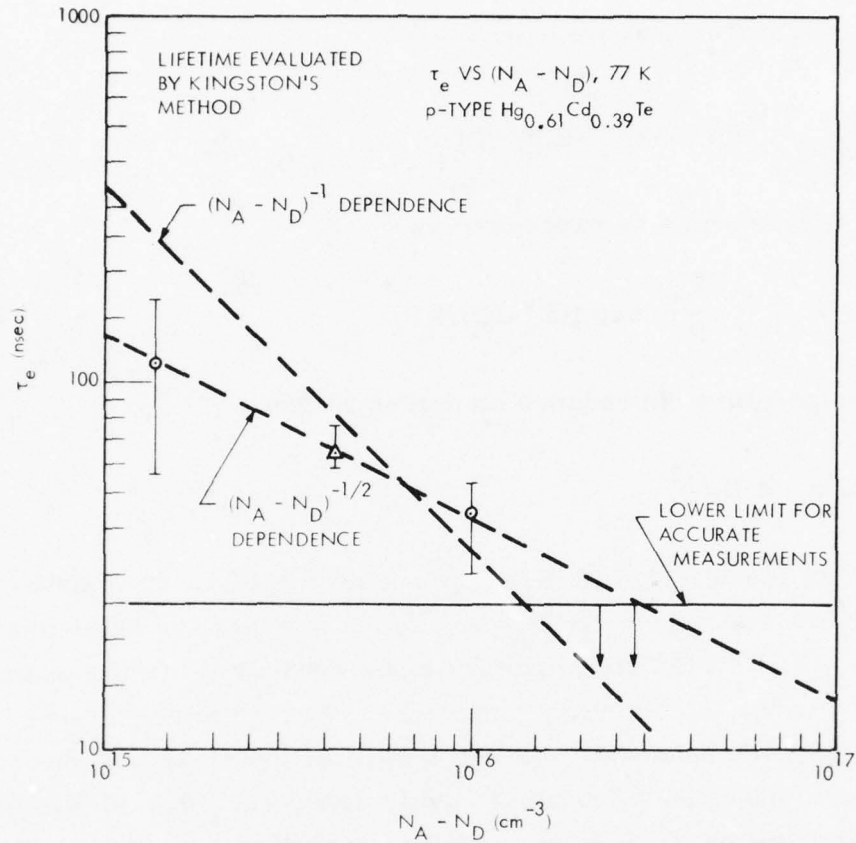


Figure 20. Dependence of Minority Carrier Lifetime at 77K on Hole Concentration

Any dependence of τ on $N_A - N_D$ must come through a dependence of N_t on $N_A - N_D$. Because τ is not independent of $N_A - N_D$ at 77K, the density of S-R recombination centers must be related to $N_A - N_D$.

At high temperatures (295K), the Fermi level is above the recombination level, and the low injection lifetime is given by

$$\tau \approx \tau_{no} \exp[(E_F - E_t)/kT] \quad (49)$$

Now for p-type materials, we have

$$\frac{p}{N_V} = \exp [- (E_F - E_V)/kT] \quad (50)$$

so that the lifetime may be expressed as

$$\tau = \tau_{no} \frac{N_V}{p} \exp [(E_V - E_t)/kT] \quad (51)$$

The high temperature dependence on doping is then

$$\tau \propto (p N_t)^{-1} \quad (52)$$

At 77K, it was found that $N_t \propto (N_A - N_D)^b$, where $0 < b < 1$. It is then expected that at 295K we would have $\tau \propto (N_A - N_D)^{-1+b}$, whereas the experimental data show $\tau \propto (N_A - N_D)$. This discrepancy arises because lifetimes cannot always be measured under low injection conditions. At high temperatures, the measured lifetimes underestimate the low-level injection lifetime. This effect is more pronounced for more lightly doped samples, so that the true low injection lifetime would have a steeper dependence on $N_A - N_D$ than measured. The high temperature results are then consistent with the low temperature results.

At 193K, the dependence of τ on $N_A - N_D$ will be intermediate between the low and high temperature dependences. It is expected to be closer to the low-temperature case, because at 193K τ is still close to τ_{no} .

In contrast, the low-injection radiative recombination model has $\tau \propto (n_o + p_o)^{-1}$, which for extrinsic p-type material becomes $\tau \propto (N_A - N_D)^{-1}$ at all temperatures. The observed change with temperature of the slope of τ versus $N_A - N_D$ lends further support to our conclusion that the lifetime is not radiatively limited. The curve for radiative lifetime versus $N_A - N_D$ at 295K has

been plotted in Figure 18. For very low doping levels the material is intrinsic at 259K, and the dependence varies from $(N_A - N_D)^{-1}$.

6.2.2.2 Lifetime versus Acceptor Concentration -- Because this p-type material is partly compensated by native donors, the number of holes will not equal the number of acceptors. Various low temperature anneals of samples from ingot 52374, to reduce the number of stoichiometric acceptors, revealed a residual n-type doping of $N_D \approx 4 \times 10^{15} \text{ cm}^{-3}$. This appears to be relatively uniform throughout the crystal. There will then be large differences between $N_A - N_D$ and N_A for lightly doped samples. Plots of τ versus $N_A - N_D$ and τ versus N_A will have different slopes, and provide different information about the lifetime mechanism.

Figures 21, 22, 23 show lifetime versus acceptor concentration at 77K, 193K, and 295K. A value of $N_D = 4 \times 10^{15} \text{ cm}^{-3}$ was used for all samples in computing N_A . This is accurate for all samples except the zone-levelled one; the native donor concentration in this crystal was not measured. We have assumed the source of unintentional native donors was the same in the growth of both crystals, and taken $N_D = 4 \times 10^{15}$ for the zone-levelled sample also.

At 77K, the data give a good fit to $\tau \propto N_A^{-1}$. Because we have $\tau \propto N_t^{-1}$ (Equation 48) in the Shockley-Read model for low injection at low temperatures, then the number of recombination centers N_t is proportional to the number of acceptors N_A . The dependence of τ on $N_A - N_D$ found in the previous subsection is actually a dependence on N_A . Physically, this makes more sense. The recombination centers are much more likely to be the result of acceptors introduced into the crystal than to be tied directly to the number of free holes.

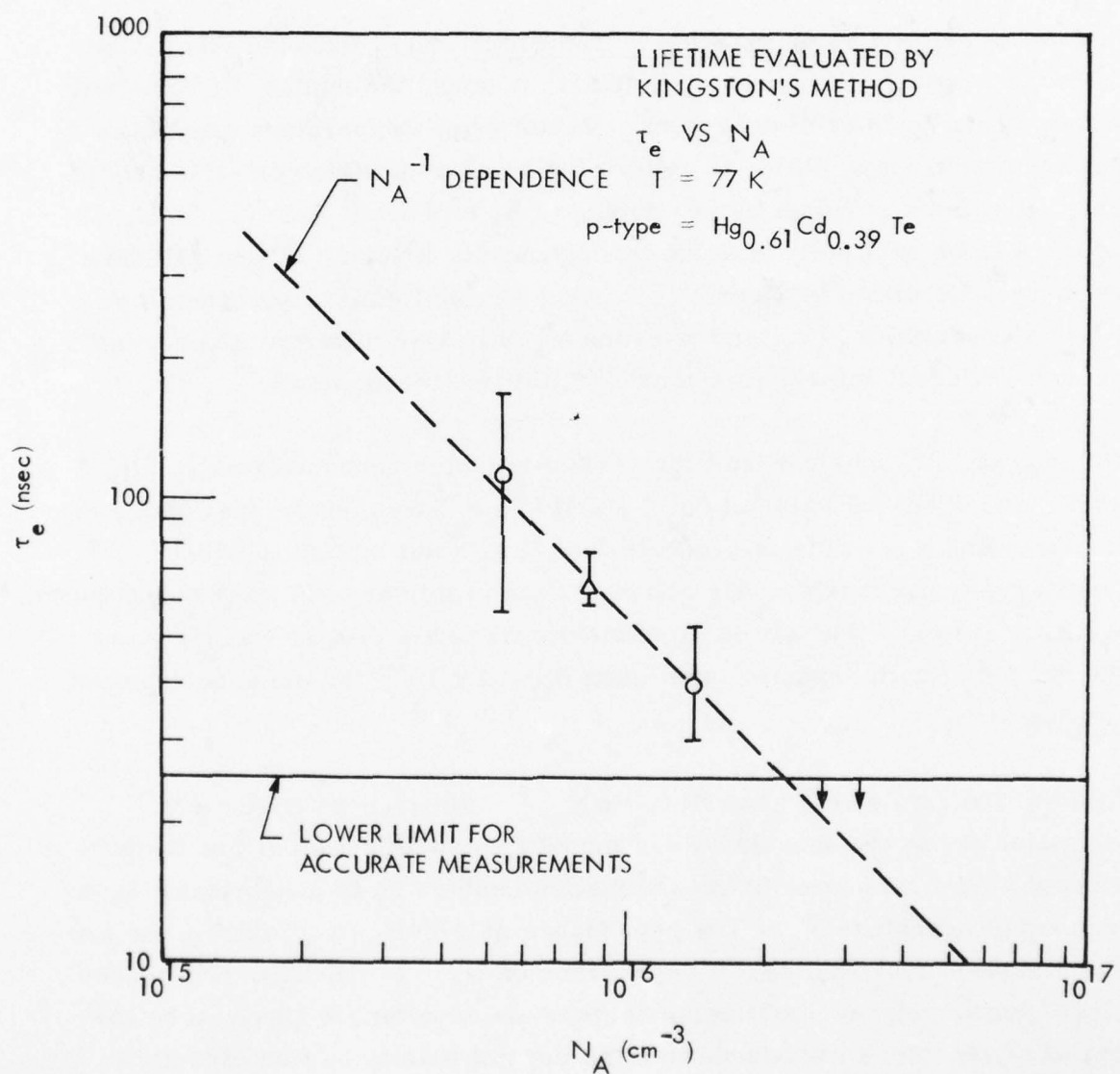


Figure 21. Dependence of Minority Carrier Lifetime at 77K on Acceptor Concentration

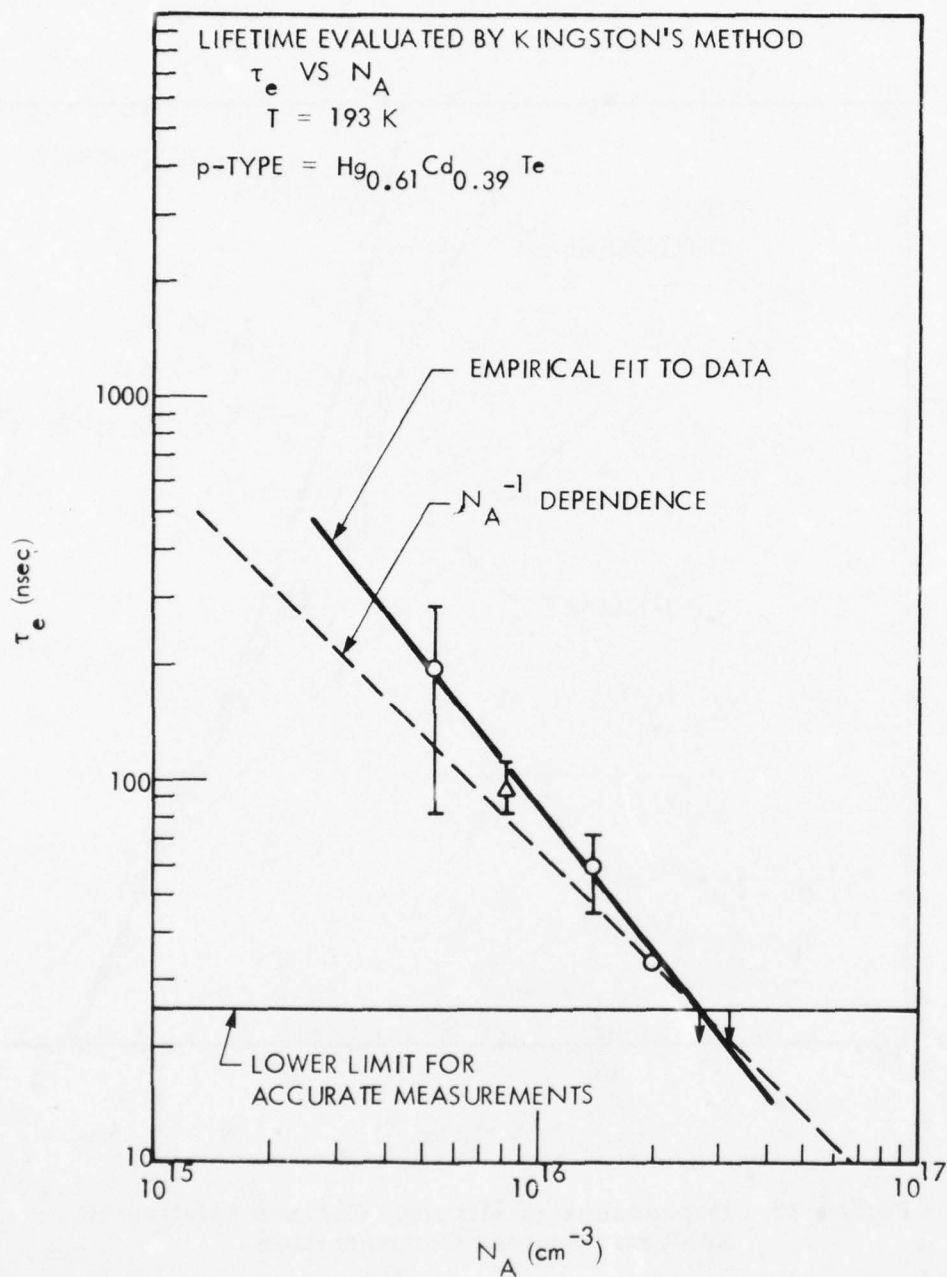


Figure 22. Dependence of Minority Carrier Lifetime at 193K on Acceptor Concentration

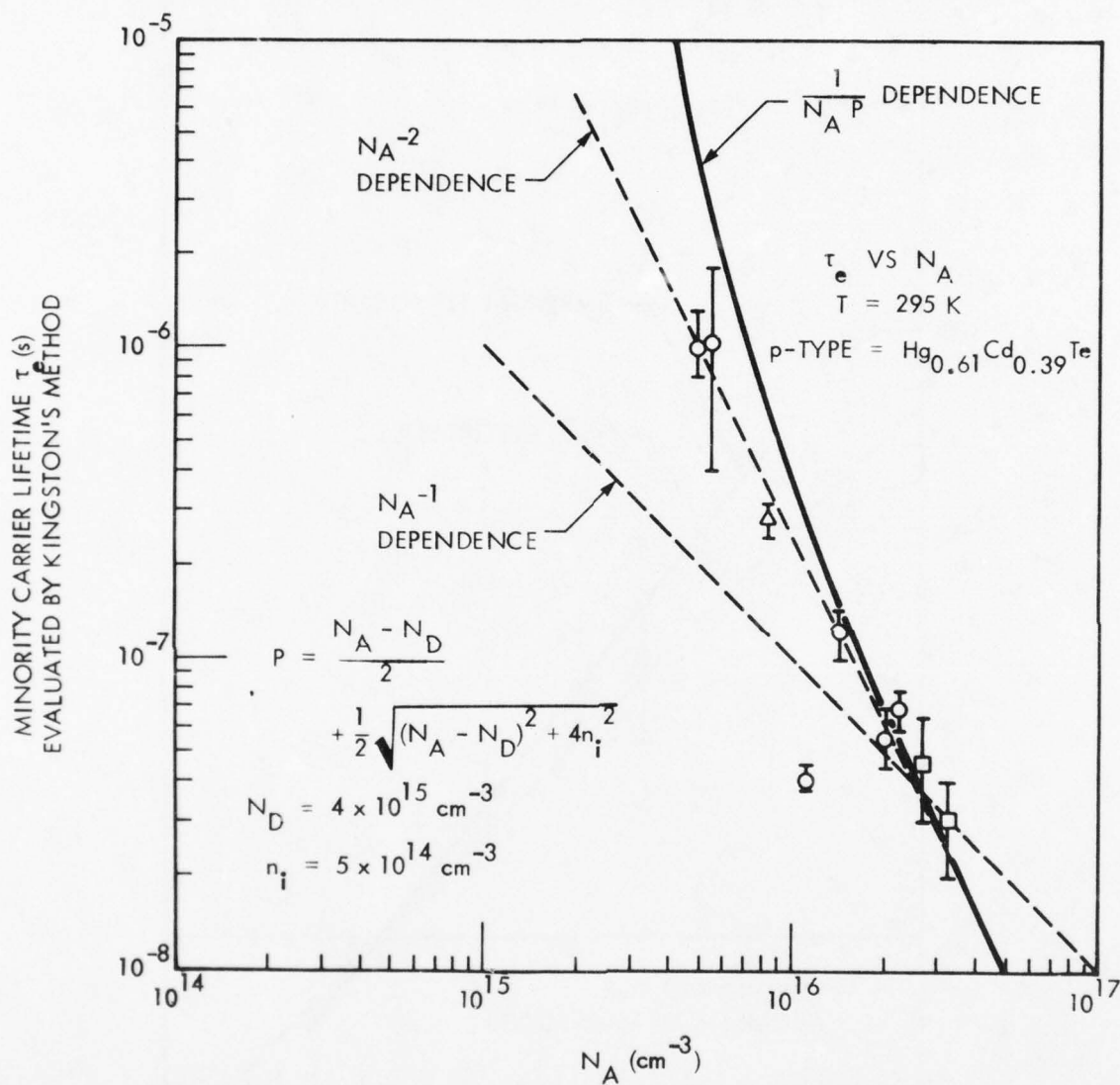


Figure 23. Dependence of Minority Carrier Lifetime at 295K on Acceptor Concentration

At 193K, τ_e versus N_A is beginning to deviate from the N_A^{-1} dependence. An empirical fit to the data give $\tau_e \propto N_A^{-1.27}$. This is because the exponential term in Equation 47 is no longer negligible. As expected, the decrease in τ_e with N_A is still significantly less steep than the $(pN_A)^{-1}$ dependence predicted for the high temperature regime.

At 295K, the dependence of measured lifetime on N_A is approximately N_A^{-2} . The $(pN_A)^{-1}$ dependence for low-injection lifetime is not seen at the low end of the N_A scale, because injection is significant in this case. The effect of non-negligible injection at high temperatures is to lower the lifetime.

The important result of this section is that the lifetime versus doping data can be explained by assuming a Shockley-Read recombination mechanism, in which the number of recombination centers is proportional to the number of acceptors.

6.2.3 Lifetime versus Excess Carrier Density

The dependence of lifetime on excess carrier density is important for two reasons. First, we would like to have a negligible excess carrier density, both to satisfy assumptions used in simple lifetime modeling, and to more accurately measure the lifetime which affects R_0A . Second, the variation of lifetime with injected carrier density, at non-negligible levels, gives additional information about the recombination mechanism. For these reasons, reverse recovery measurements were made using a wide range of the forward current I_F , which can be related to excess carrier density.

Figure 24 presents lifetime versus excess carrier density measurements for lightly doped ($N_A - N_D = 1.4 \times 10^{15} \text{ cm}^{-3}$) sample 2 at three temperatures. The dependence of τ_e on Δn shown here is representative of the samples tested: with increasing Δn , lifetime decreases at room temperature, remains nearly constant at 193K, and increases at 77K. This

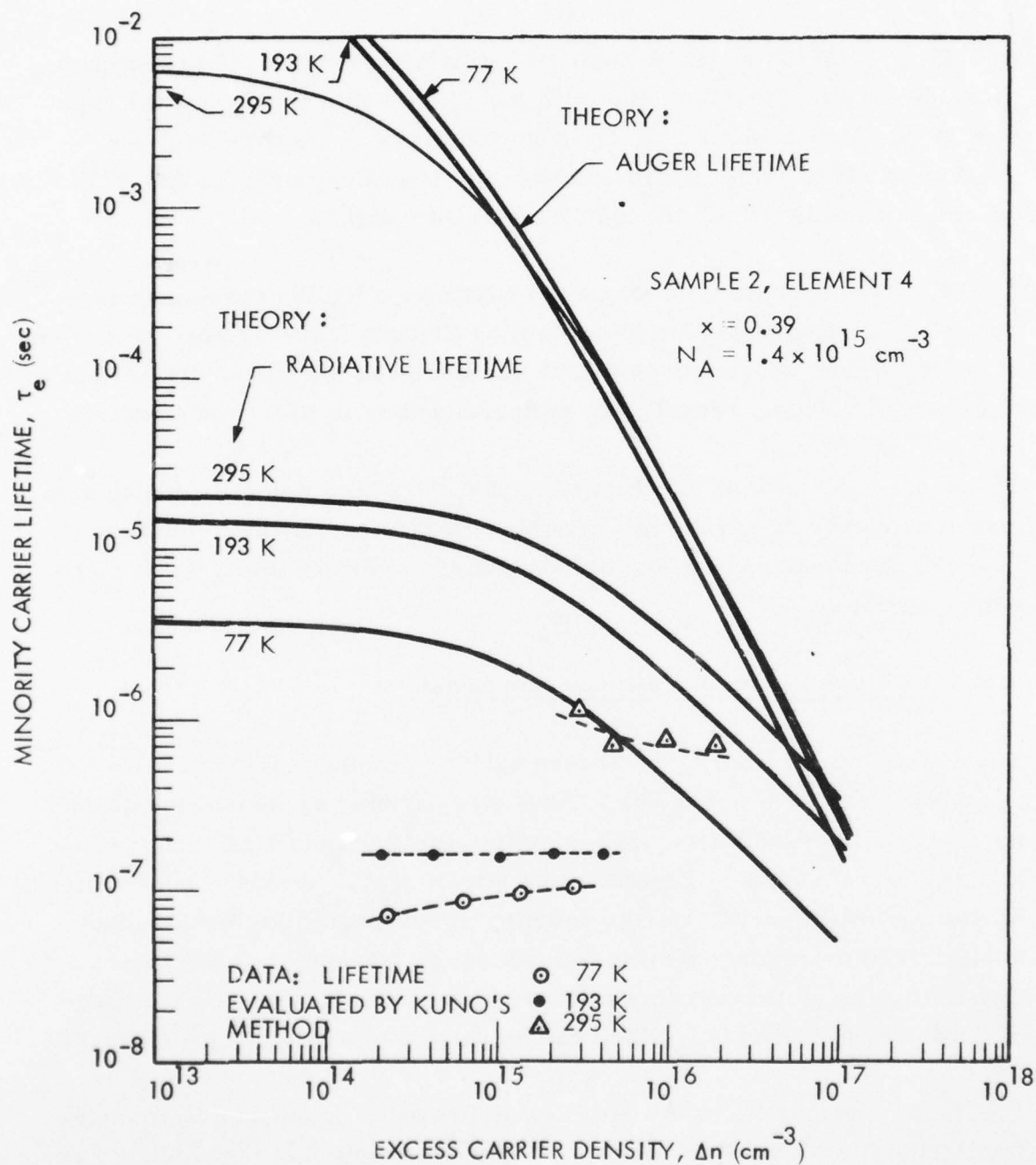


Figure 24. Minority Carrier Lifetime as a Function of Carrier Injection Level; Data Compared to Auger and Radiative Theories

dependence cannot be explained by either radiative or Auger recombination, as shown in Figure 24. Theoretical curves were plotted using the expressions in Section 2.2. Magnitude, variation with Δn , and variation with temperature all show poor agreement with the data.

The simple Shockley-Read model provides a much better fit in all respects; see Figure 25. Dependencies on Δn and temperature are in good agreement with the data, and may be physically understood as follows. Assume an acceptor-type recombination level near the center of the energy gap. At 77K, the Fermi level is well below the recombination level; lifetime is determined by electron capture at the recombination center. Increasing the density of excess carriers fills some of these centers, hence increasing the lifetime. At 295K, the Fermi level is above E_T so that the traps are mostly filled; lifetime is limited by hole capture from the valence band. Increasing Δn increases the number of traps filled by electrons, and hence decreases the hole lifetime. At 195K we have a situation midway between the extremes, where the Fermi level is near the trap level. Changing Δn has little effect on the lifetime.

Figure 25 also provides a check on the validity of low-level injection assumptions. At 77K and 193K, the change of lifetime with Δn is very small; data points for the lowest values of Δn are in excellent agreement with the calculated asymptotic values for $\Delta n \rightarrow 0$. These experimental lifetimes can then be used quite accurately (within 20 percent) to model diode $R_0 A$, and for comparison with theoretical low-level injection models for lifetime. At 295K, the variation of τ_e with Δn is greater, and agreement with the simple S-R model is poorer than at the lower temperatures. Although extrapolation to a low-level lifetime is not possible due to limited data, this lifetime will certainly be longer than the highest measured value; the theoretical curve suggests a factor of two increase. Injection effects must then be considered when interpreting high-temperature lifetime measurements of this lightly doped material.

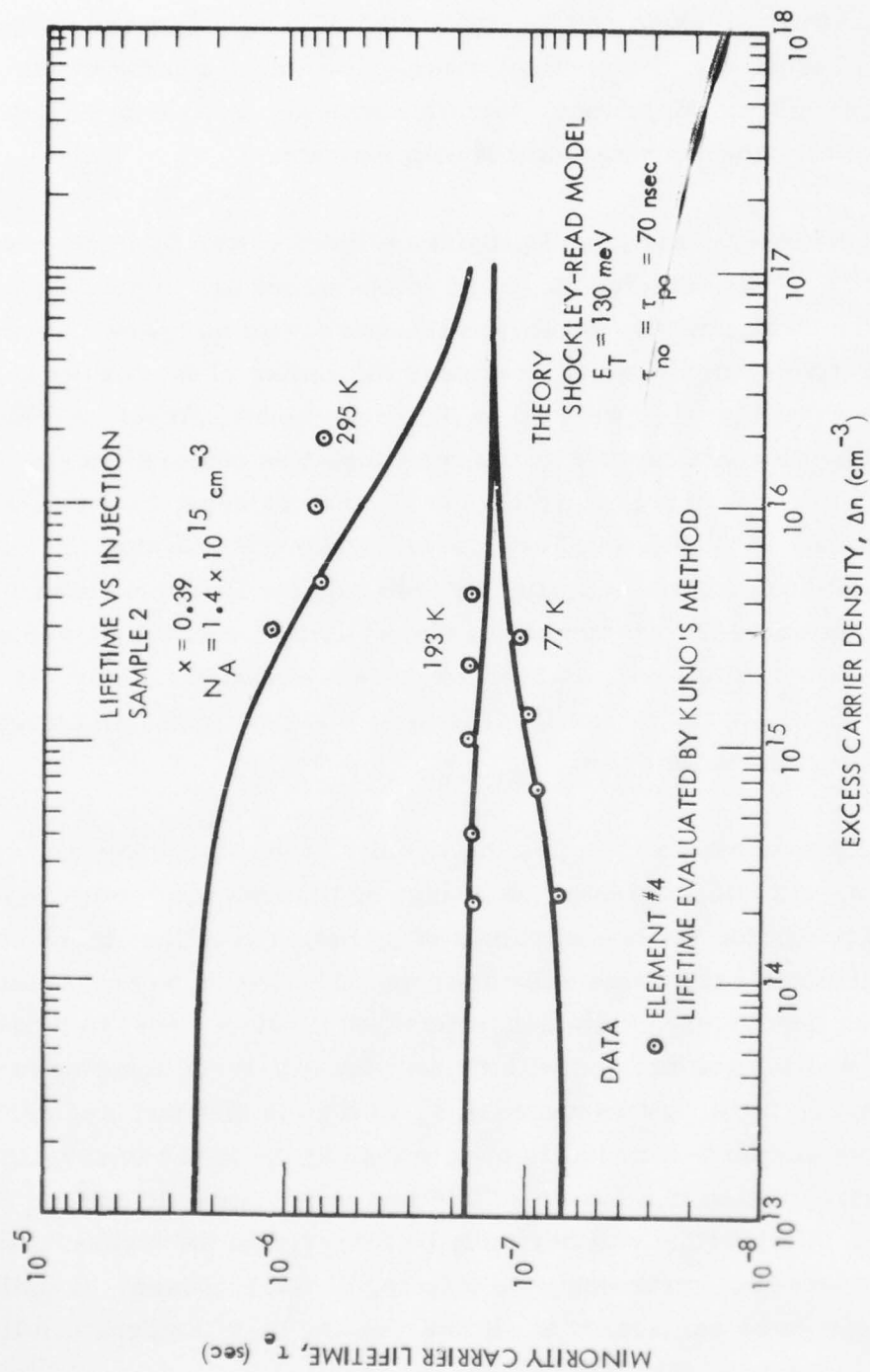


Figure 25. Minority Carrier Lifetime as a Function of Carrier Injection Level; Data of Figure 24 Compared to Shockley-Read Theory

AD-A071 094

HONEYWELL ELECTRO-OPTICS CENTER LEXINGTON MA
MINORITY CARRIER LIFETIME AND DIFFUSION LENGTH IN P-TYPE MERCUR--ETC(U)
FEB 79 J L SCHMIT, S P TOBIN, T J TREDWELL F33615-77-C-5142

UNCLASSIFIED

AFML -TR-79-4036

NL

2 of 2
AD
A071094



END
DATE
FILMED
8 -79
DDC

Lifetime versus Δn for a more heavily doped sample is shown in Figure 26 with calculated S-R lifetime curves. Again, radiative and Auger lifetimes need not be considered. For more heavily doped material, the effect of excess carriers is less severe; lifetime is nearly independent of the injection level. A good approximation to the low-level lifetime is, therefore, expected from measured values. As in the previous sample, the one-level S-R model gives a good qualitative fit to the data.

6.2.4 Lifetime Uniformity

The uniformity of lifetimes measured on multielement diode arrays varied from sample to sample. An idea of the range of measured lifetimes for each array can be obtained from Figures 18, 19, 20, with array descriptions in Table 6. All of these measurements were made with the same junction area, I_F , and I_F/I_R . In general, the variation in measured lifetime was greatest for the most lightly doped material, which also had the greatest variation in $N_A - N_D$ (due to close compensation). Figure 27 shows a map of lifetime versus position for a diode array on lightly doped material. The variations in lifetime are, in general, systematic, and suggest variations in carrier concentration, or density of trapping centers, across the wafer. The composition (x-value) variation across the wafer, measured by diode spectral response, is very small and cannot explain the lifetime variations.

Lifetime was more uniform for the zone-levelled sample shown in Figure 28, and the quench/annealed sample of Figure 29. Both were more heavily doped than the previous sample, with more uniform $N_A - N_D$ (measured by MIS). Again, variations in lifetime seem tied to variations in hole concentration.

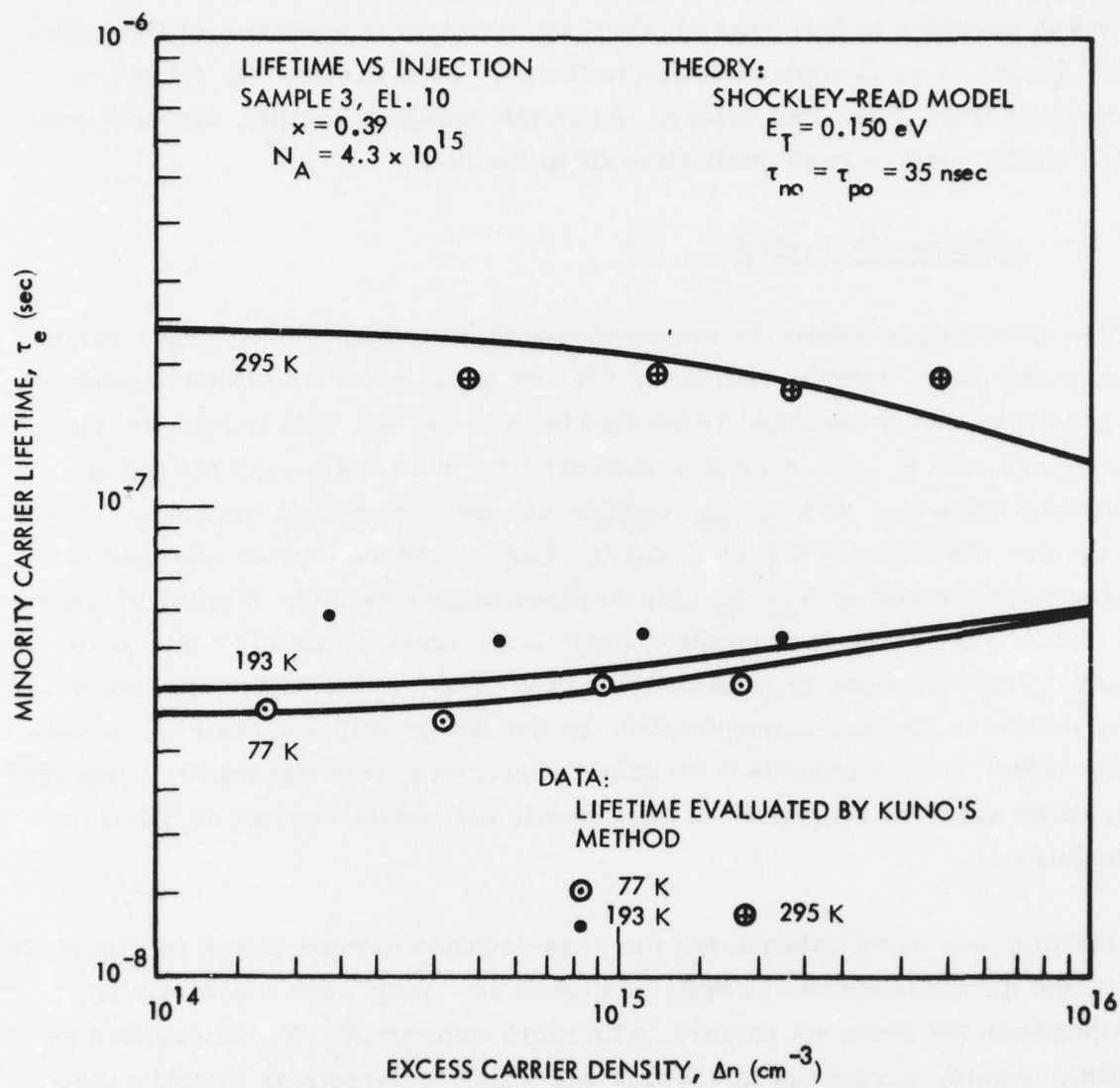


Figure 26. Minority Carrier Lifetime by Kuno's Method as a Function of Injected Carrier Density

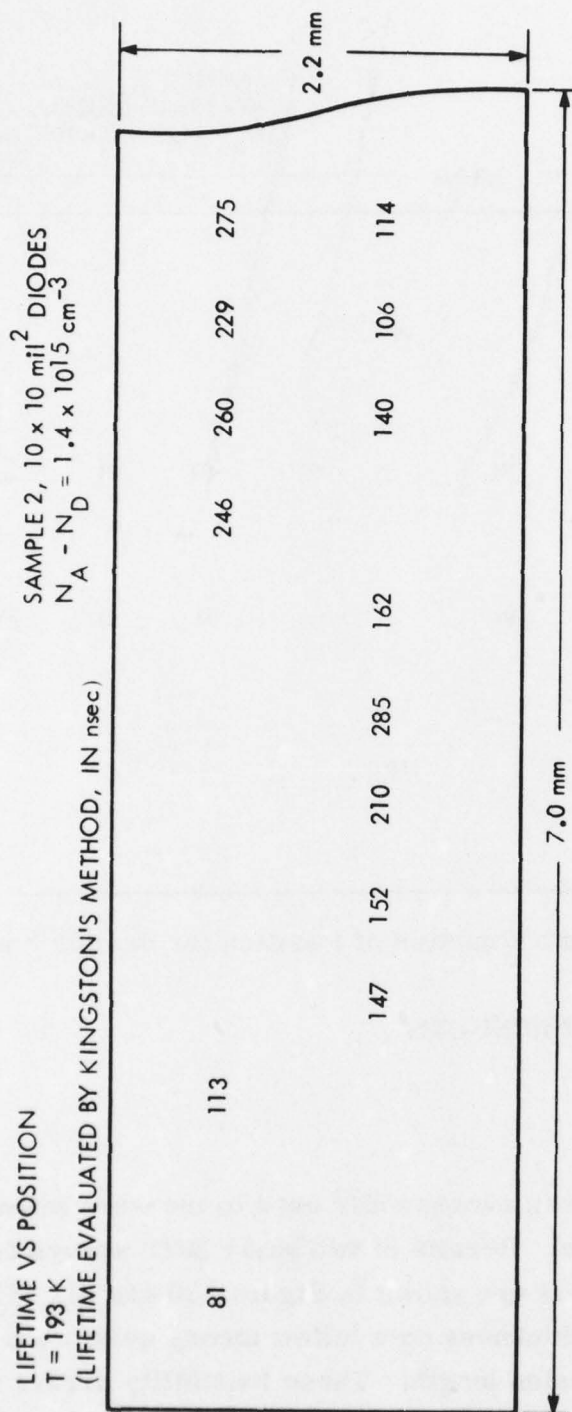


Figure 27. Lifetime as a Function of Position for Sample 2 at 193K

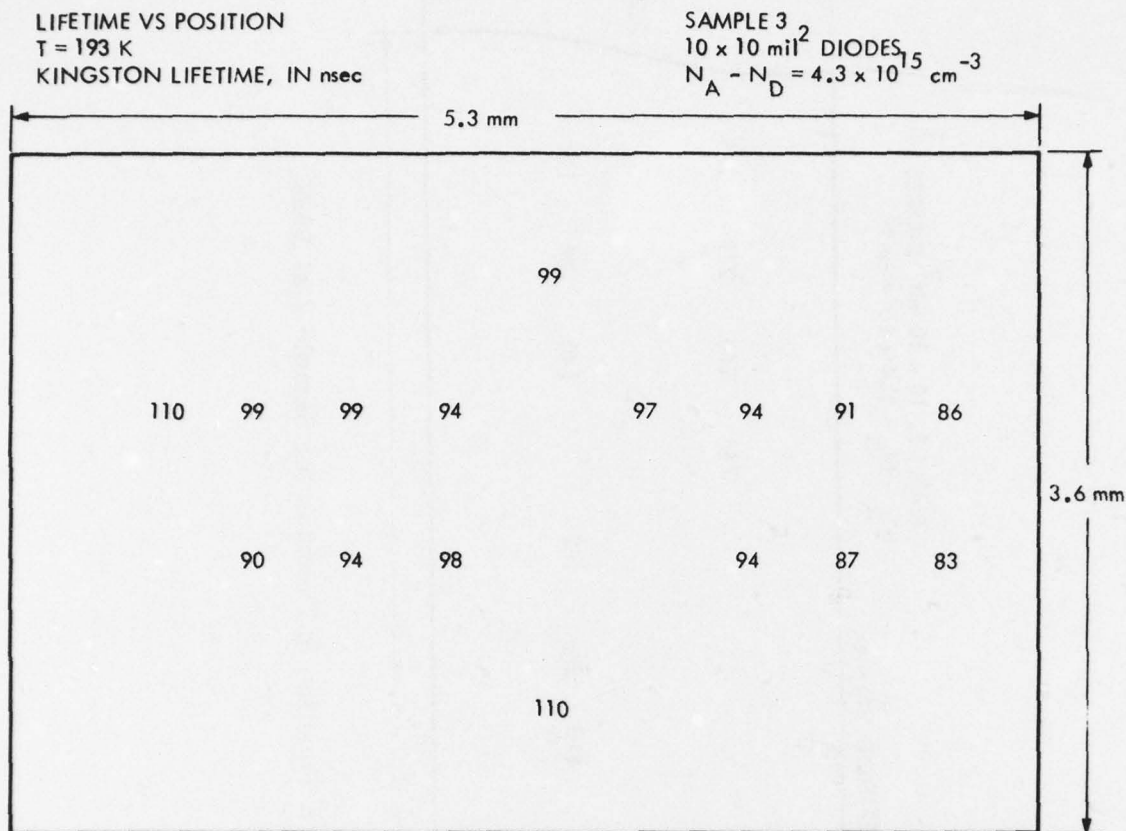


Figure 28. Lifetime as a Function of Position for Sample 3 at 193K

6.3 DIFFUSION LENGTH RESULTS

6.3.1 BITS Results

The BITS structure has been successfully used to measure minority carrier diffusion length in HgCdTe. Results of two early BITS arrays fabricated on 4- and 5- μm cutoff material are shown in Figures 30 and 31. The signal current versus material thickness data follow theory quite well, yielding reasonable values of diffusion length. These feasibility arrays were, however, of longer cutoff wavelengths than material of interest for this program, and hence not directly applicable.

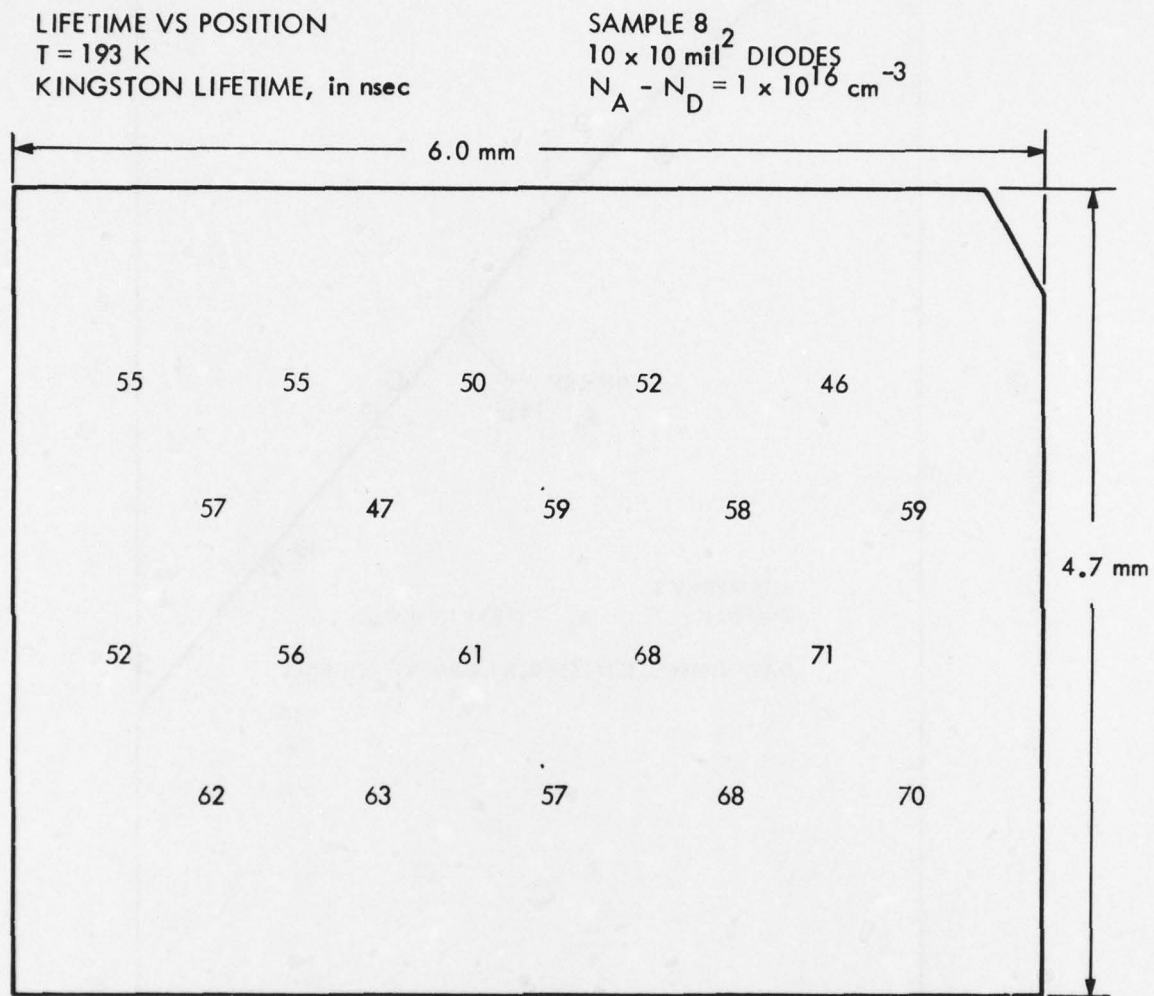


Figure 29. Lifetime as a Function of Position for Sample 8 at 193K

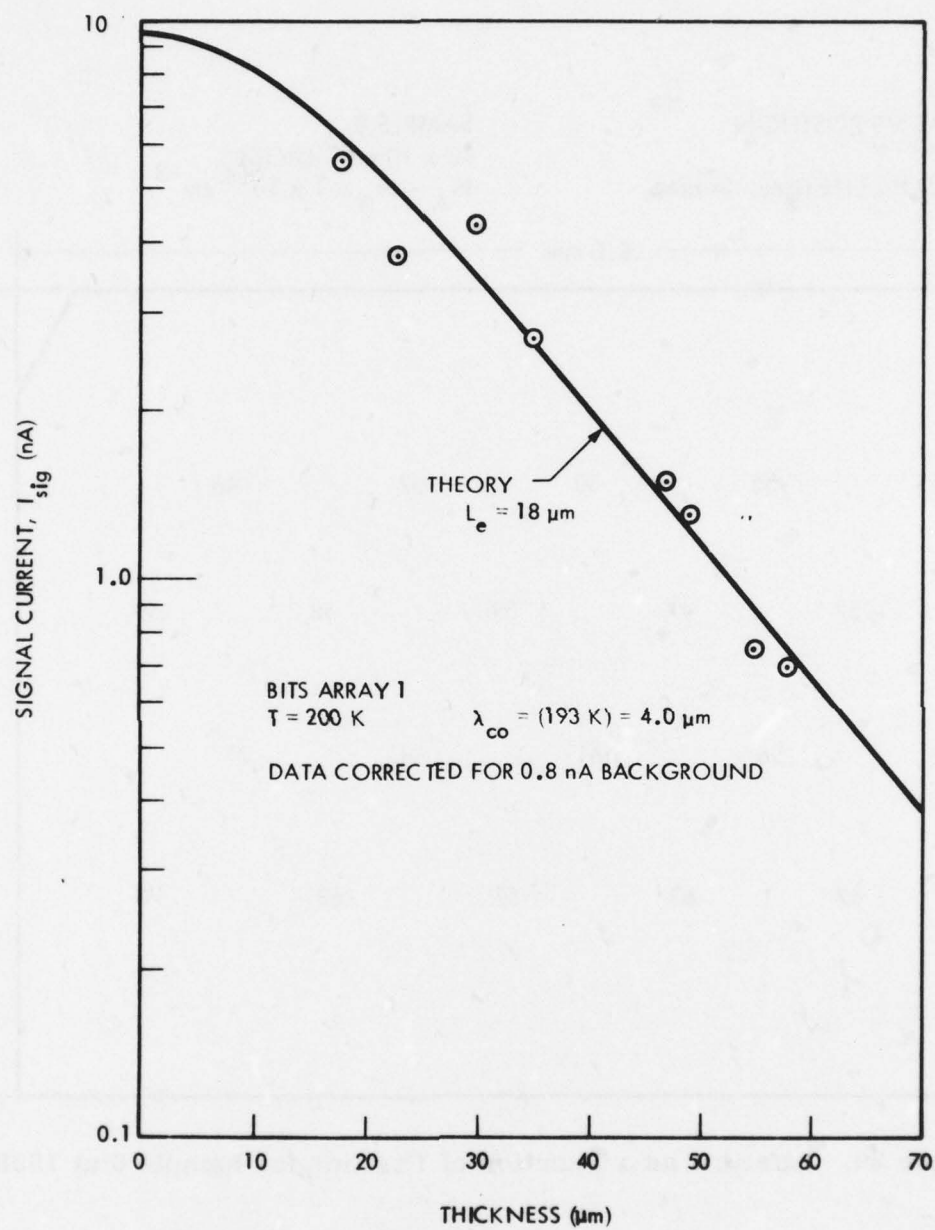


Figure 30. Thickness Dependence of Signal Current for a 4- μm Cutoff BITS Array at 200K

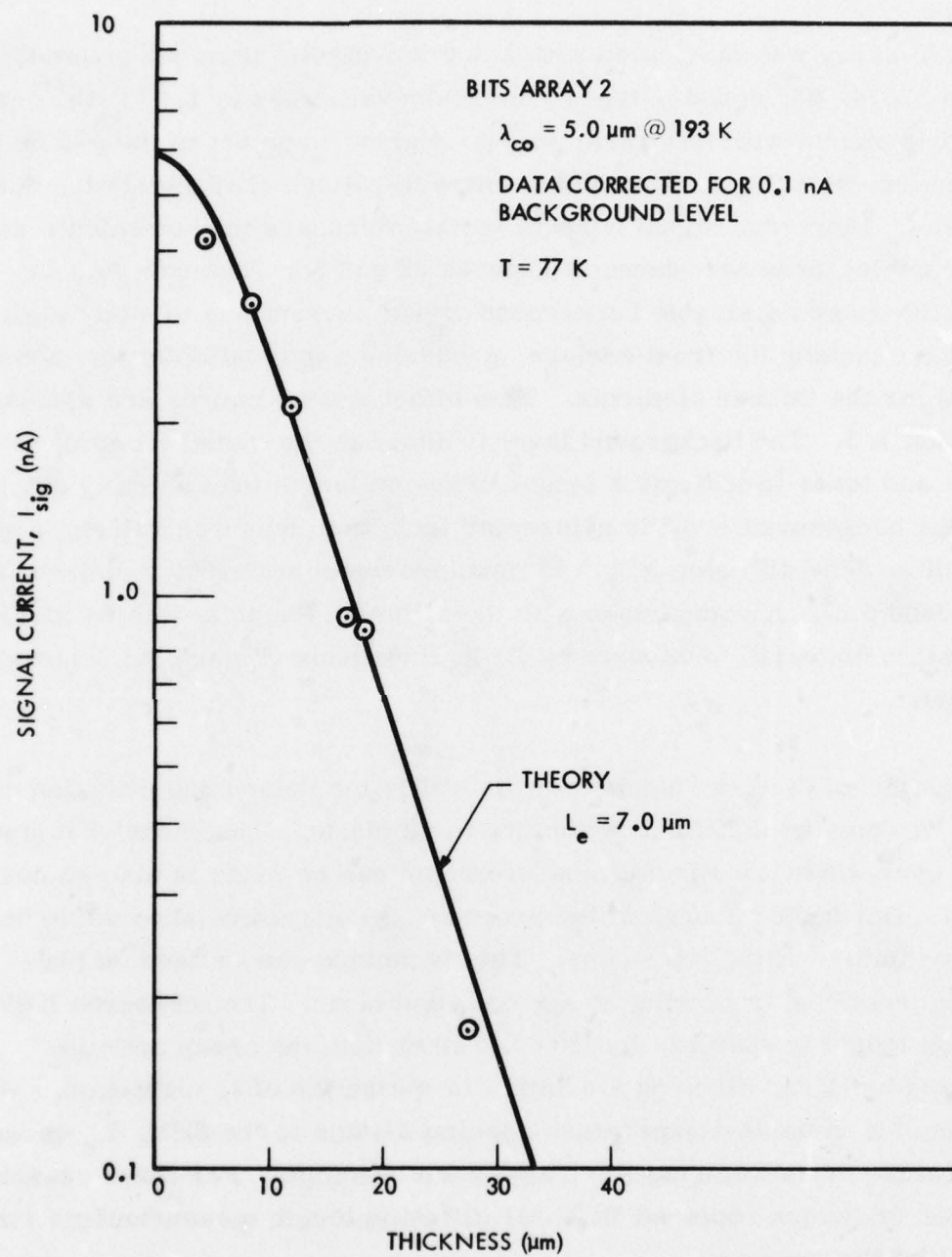


Figure 31. Thickness Dependence of Signal Current for a 5- μm Cutoff BITS Array at 77K

One BITS array was fabricated with a $3.0\text{ }\mu\text{m}$ -cutoff, from as-grown Q/A sample 52374, 02, doped p-type by mercury vacancies to $1.75 \times 10^{16}\text{ cm}^{-3}$. A major problem with this array was poor ground contact to the p-side of the junctions, leading to nonuniform current-voltage characteristics down the array. However, signal current versus thickness measurements were still possible; these are shown in Figures 32 and 33. The raw data in Figure 30 showed a sizable background signal current due to stray signal radiation reaching the front surface, producing a saturation of the measured current for the thicker elements. This effect and its causes are discussed in Section 4.3. The background level is added to the signal from all elements, and tends to indicate a longer diffusion length than actually exists. When the background level is subtracted from the measured values, Figure 33 results. The diffusion length is much more accurately determined from this second plot. A comparison with the diffusion length at this temperature for similar material, measured by EBIC line scans (Figure 36), shows good agreement.

Although the BITS array has proven its utility for measuring diffusion length, it remains a difficult structure to fabricate. The range of temperatures over which meaningful measurements can be made is also somewhat limited. During the course of the program, an attractive alternative became available: EBIC line scans. This technique can be used on pre-existing junctions, requiring no special structures. The measured EBIC diffusion length is spatially localized, rather than the array average measured by BITS, allowing a detailed investigation of L_e variation. With addition of a variable-temperature specimen stage to the SEM, L_e versus temperature measurements were also made possible. For these reasons, the EBIC technique replaced BITS for diffusion length measurements for the bulk of the program.

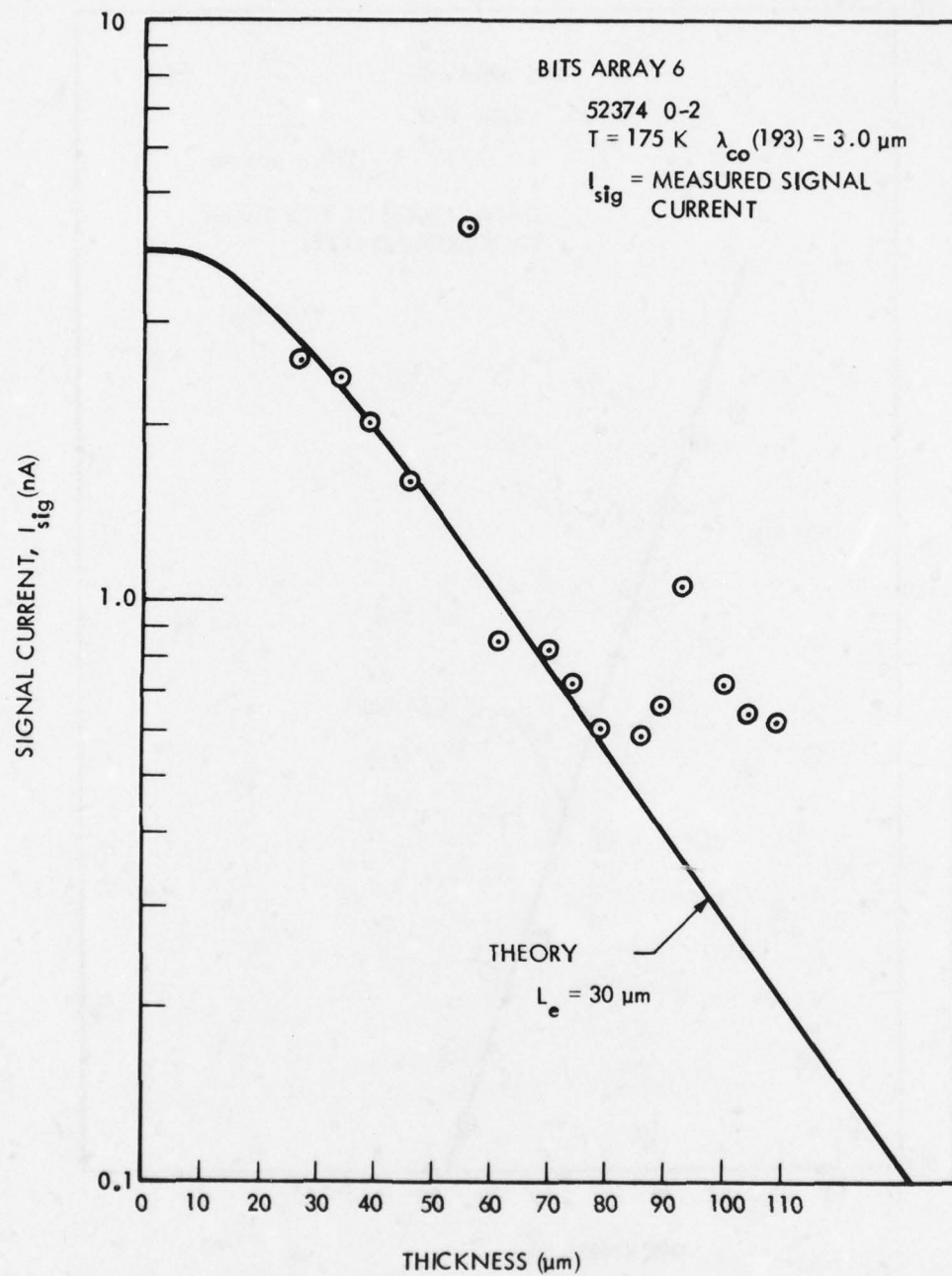


Figure 32. Thickness Dependence of Signal Current for BITS Array Number 6 from Sample 7 at 175K

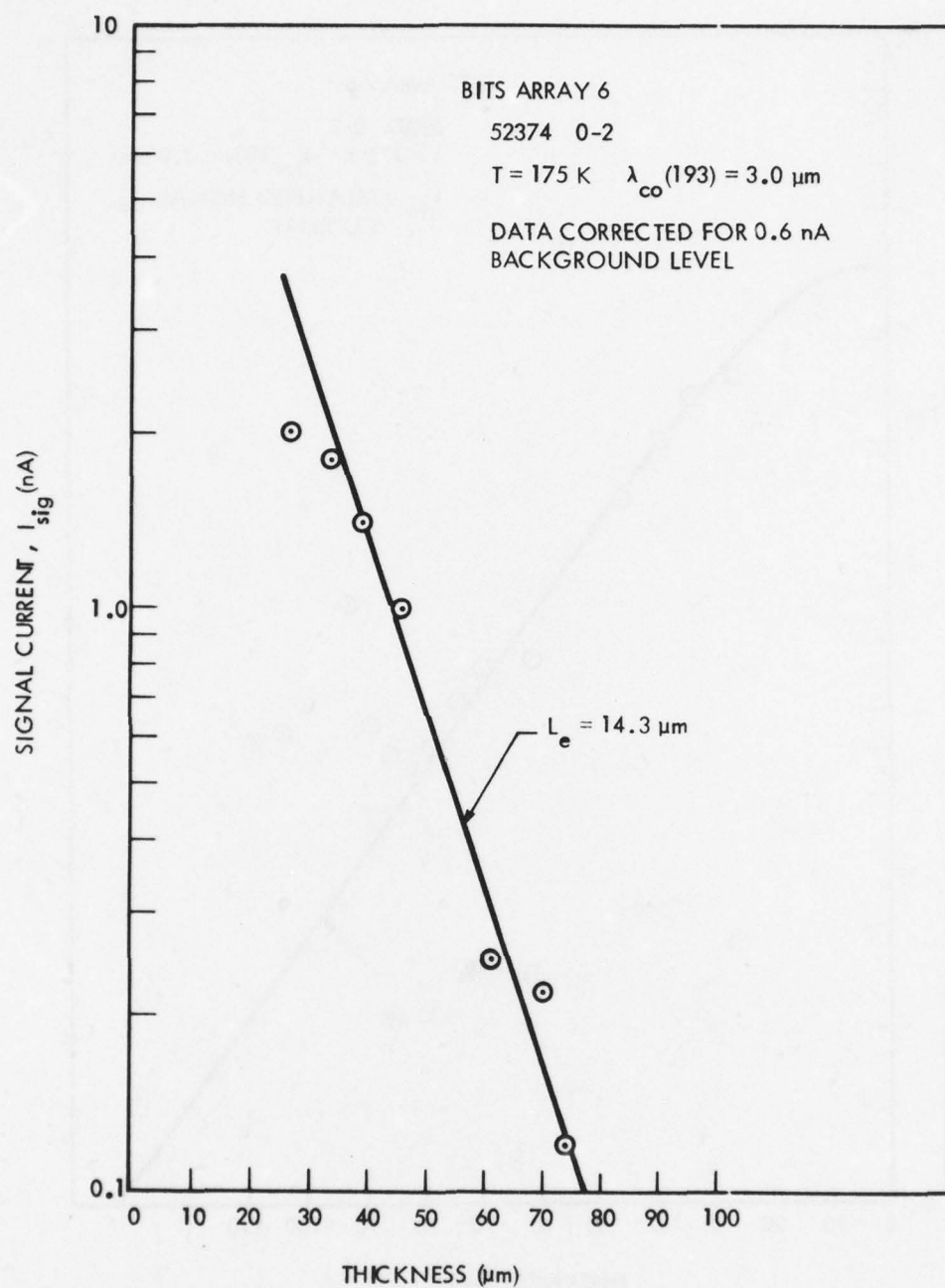


Figure 33. The Data of Figure 32 Corrected for Background Level

6.3.2 Diffusion Length versus Temperature

Using EBIC line scans, the diffusion length as a function of temperature was measured for several samples. Each scan was taken at approximately the same spot on the junction edge to minimize positional variations in L_e ; however, some movement of the scan position was unavoidable when changing magnification scales. Studies of L_e uniformity with position (Section 6.3.4) show this variation to be a minor effect.

Figures 34, 35 and 36 present L_e versus temperature data for three samples, with a range of carrier concentrations. Diffusion length generally increases with temperature due to increasing lifetime. The increase in L_e from 80K to 300K is greatest for the most lightly doped material, and least for the most heavily doped.

For the most lightly doped material, Figure 34, an anomalous decrease in L_e is seen at the highest temperatures. Ambipolar effects are responsible, as explained in Section 6.4. For low dopings and high temperatures, the intrinsic concentration becomes comparable to $N_A - N_D$, so that it is no longer simply the minority carrier electron diffusion length being measured. More heavily doped samples do not show the decrease of L_e at high temperatures, but ambipolar diffusion length must still be considered. Room temperature measurements should be interpreted as ambipolar diffusion length on the p-side, which will be less than the electron diffusion length. However, at lower temperatures, such as 80K and 195K, the ambipolar effects are negligible; true minority carrier electron diffusion length is measured.

6.3.3 Diffusion Length versus Carrier Concentration

Some data exists on diffusion length versus carrier concentration, although the small number of samples makes any conclusions only tentative. Figure

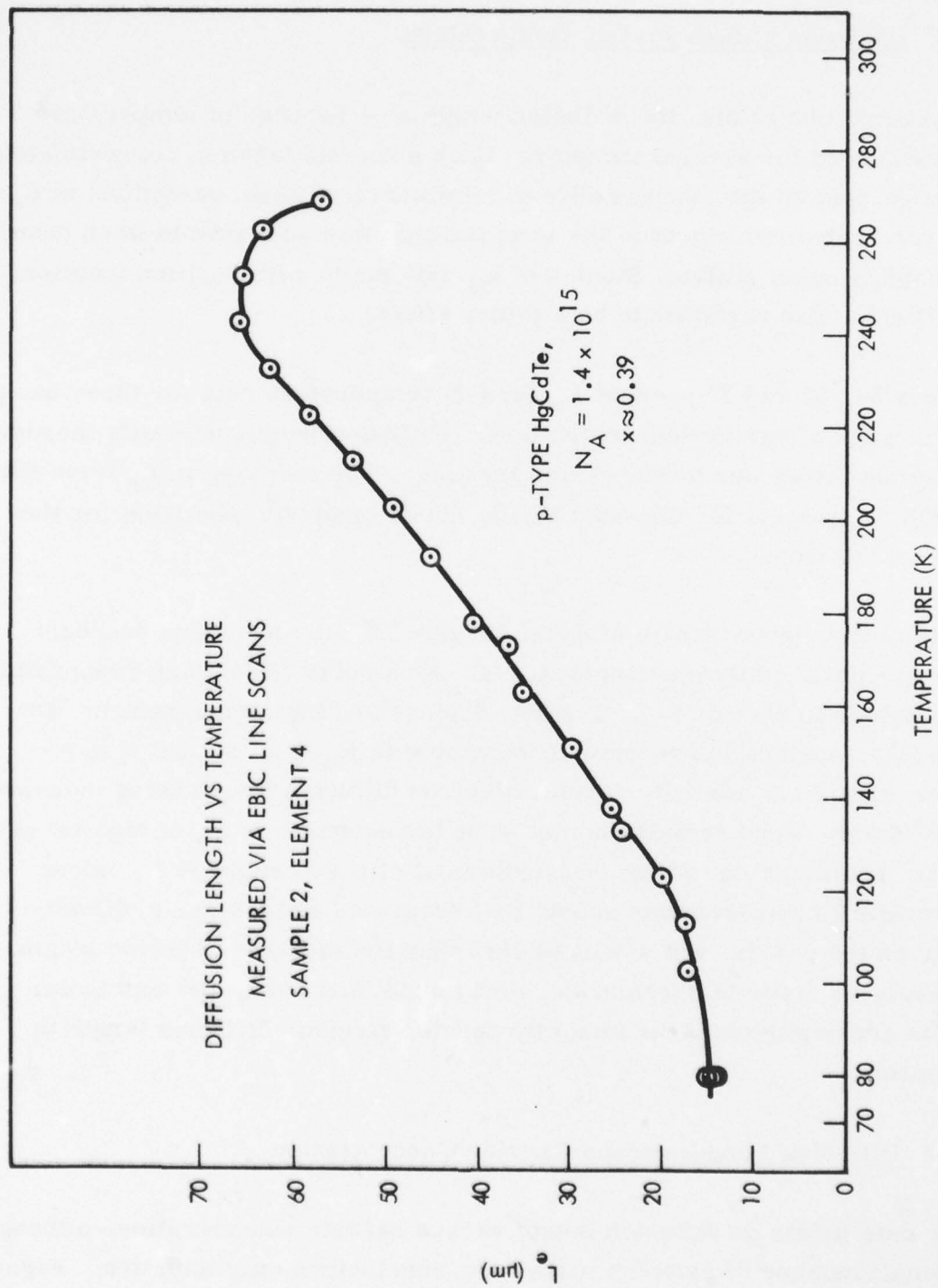


Figure 34. Temperature Dependence of Minority Carrier Diffusion Length, L_e , for Sample 2

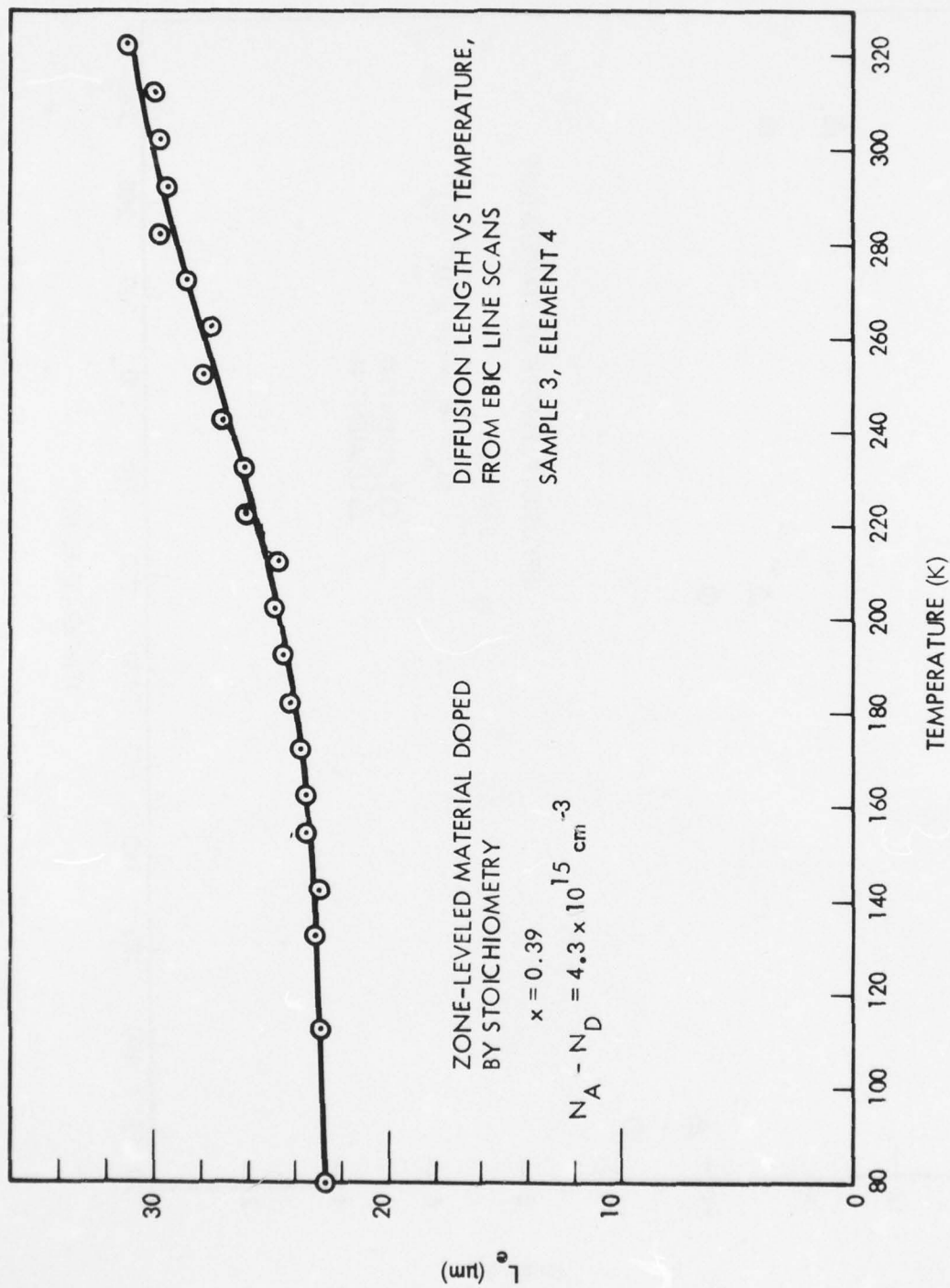


Figure 35. Temperature Dependence of L_e for Sample 3

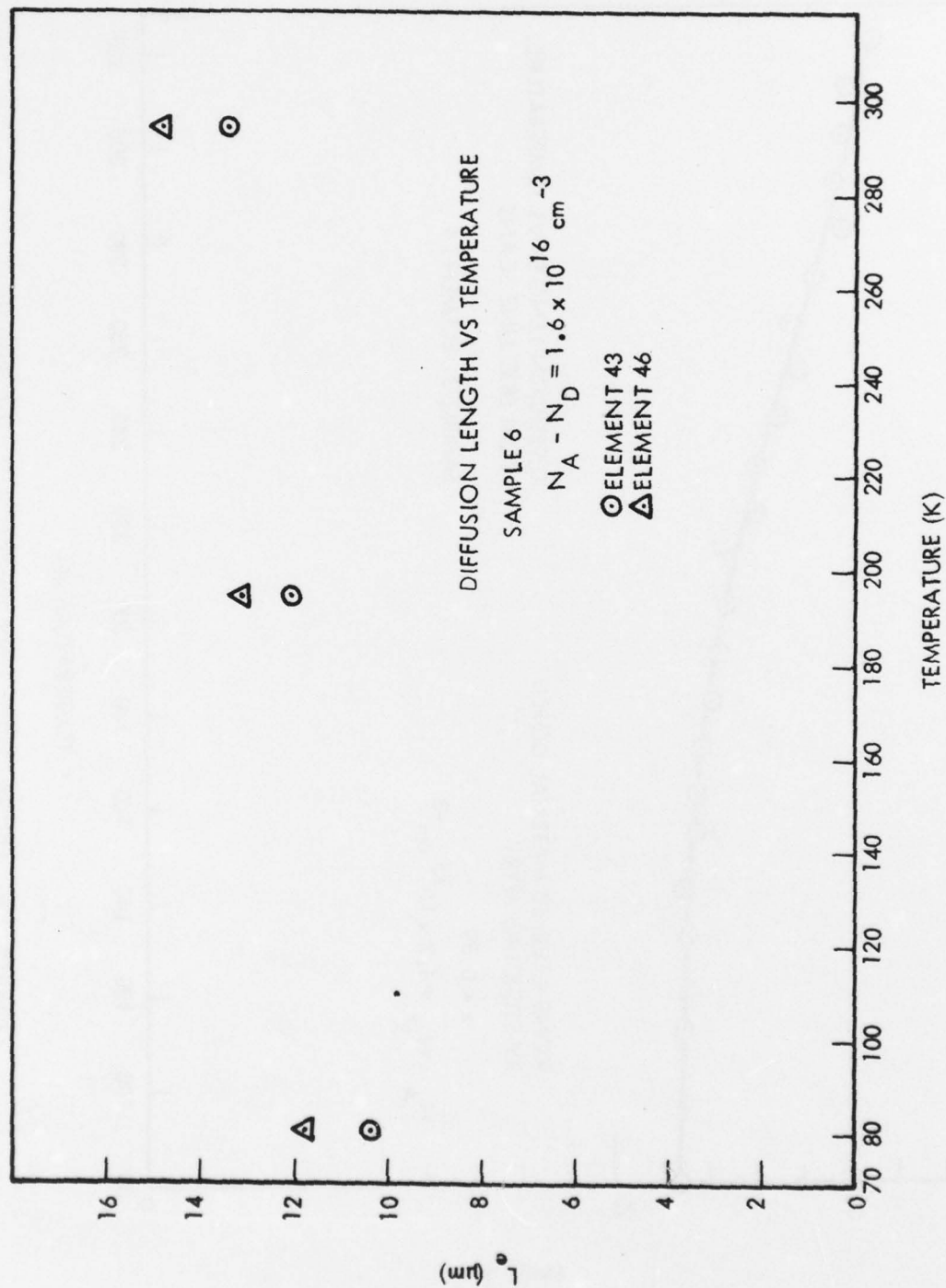


Figure 36. Temperature Dependence of L_e for Sample 6

37 plots the data at 80K and 195K. More data is available at room temperature, but because of ambipolar effects, any comparison in terms of electron diffusion length would be meaningless.

At 195K, L_e follows roughly an $(N_A - N_D)^{-1/2}$ dependence. This is expected if mobility is a weak function of $N_A - N_D$, since $L_e \propto \tau_e \mu_e$, and τ_e has an $(N_A - N_D)^{-1}$ dependence at this temperature. At 77K, the same dependence of L_e on $N_A - N_D$ holds for the more heavily doped samples, but not for the lightest one. A large number of line scans were tested for this array, yielding consistent results; we are confident in the data's correctness. Because τ_e at this temperature is in line with data from other arrays (Figure 20), it must be the mobility which is abnormally low. The reason for this low mobility at 77K is not known.

6.3.4 Uniformity of Diffusion Length

The EBIC technique allows extremely localized probing of the minority carrier diffusion length. It is, therefore, a useful tool for examining material uniformity in terms of material parameters which affect photo-diode performance. Due to the nature of the SEM cold stage used for the measurements, extended operation at a fixed temperature could be carried out only at 80K and room temperature. The uniformity data were, therefore, recorded at one of these temperatures.

Table 7 summarizes the data for several arrays. Uniformity is relatively good; in no case is the deviation from the mean L_e greater than ± 10 percent.

Figure 38 shows the variation of L_e with position on a plank of lightly doped material. MIS measurements of $N_A - N_D$ showed this to be one of the most nonuniform samples tested, in terms of carrier concentration; it is, therefore, expected to be a worst-case example of L_e variation.

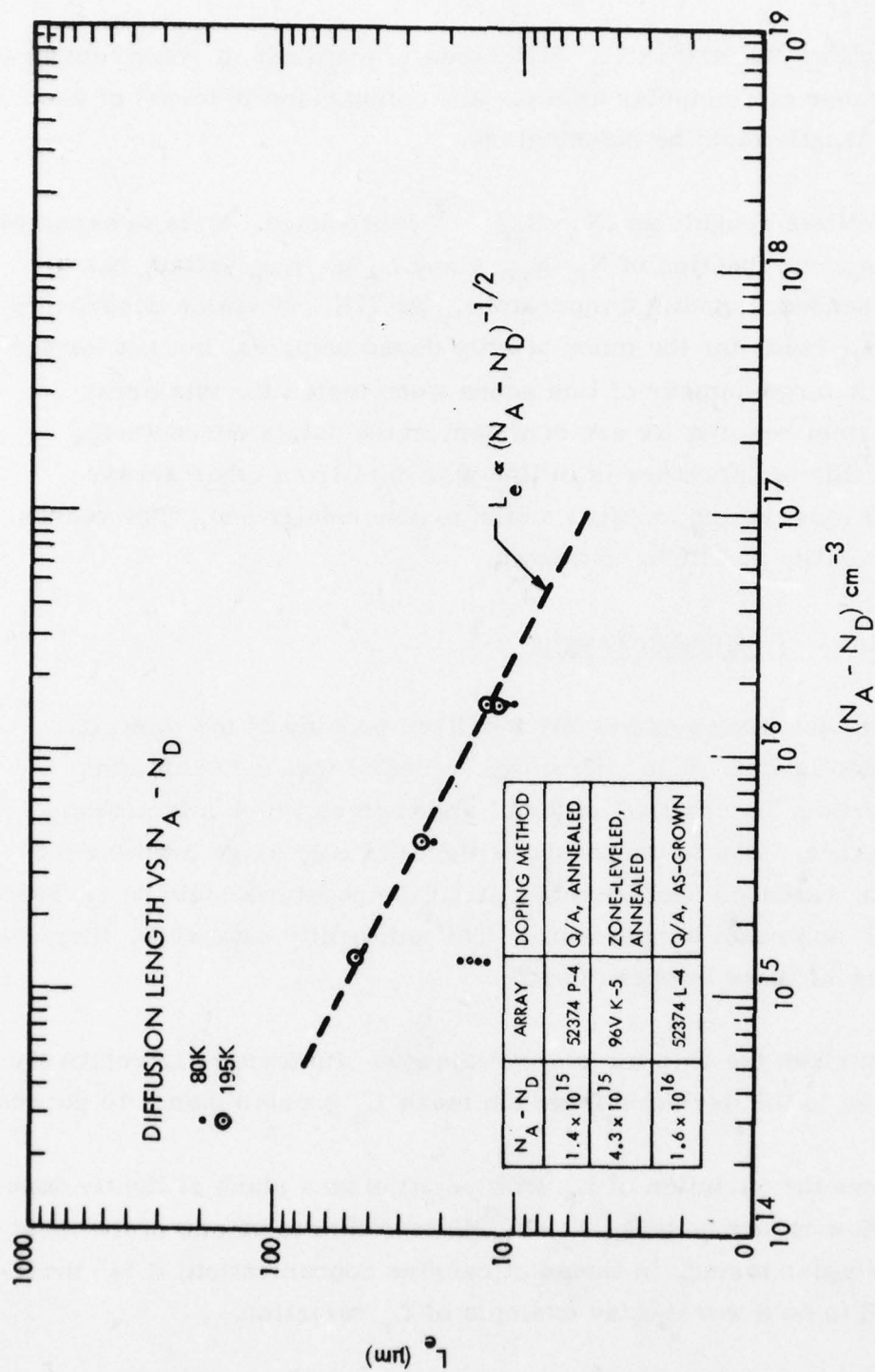


Figure 37. Dependence of L_e on Hole Concentration

Table 7. Interarray Uniformity of Measured Diffusion Length at 80 and 295K

T = 295°K				
Sample	Number of Diodes Tested	Number of Scans Made	Mean L_e (μm)	Standard Deviation (μm)
6	3	4	13.6	0.8
5	3	5	13.2	0.8
T = 80°K				
Sample	Number of Diodes Tested	Number of Scans Made	Mean L_e (μm)	Standard Deviation (μm)
2	6	12	14.7	0.7
4	3	6	22.3	1.0
6	3	3	11.2	0.7

It should be noted that scans were not taken near the junction corners, where spreading of the electric field can give artificially low values. In order to check for anisotropic diffusion length, scans were made in perpendicular directions, for several junctions. No dependence on scan direction was seen.

6.4 MINORITY CARRIER MOBILITY

From measurements of lifetime by reverse recovery and diffusion length by EBIC, minority carrier mobility has been derived, using Equation 6. One such curve, for a range of temperatures, is shown in Figure 39. The experimental curve is to be compared to another experimental curve of

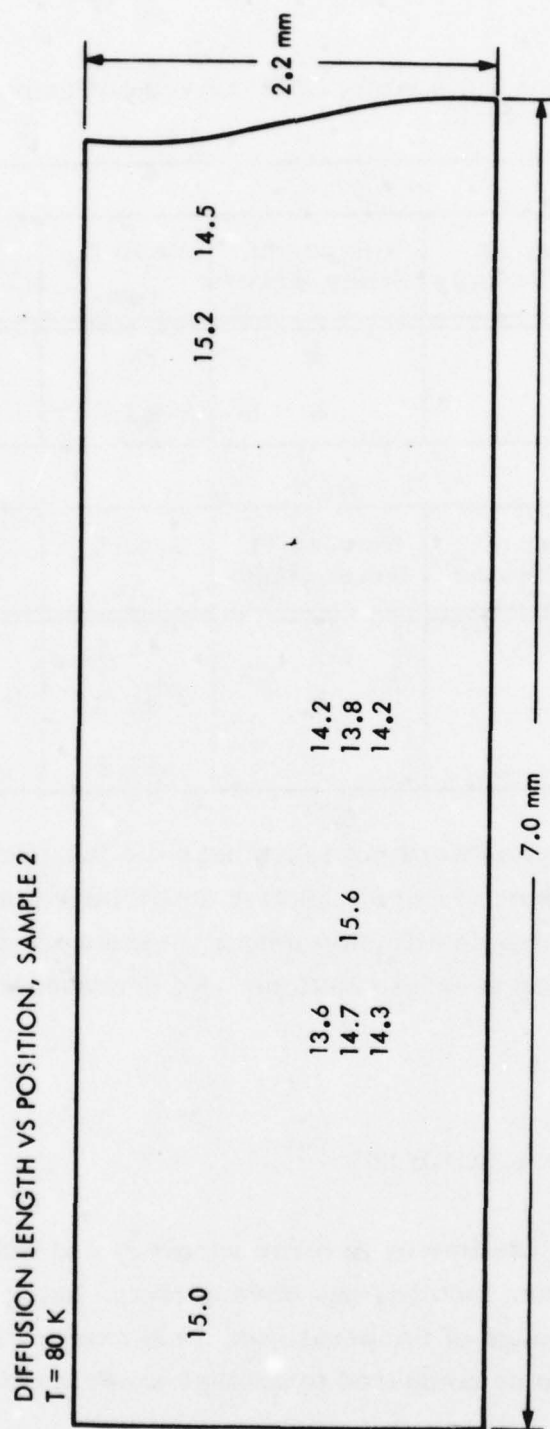


Figure 38. Diffusion Length versus Position for Sample 2 at 80K

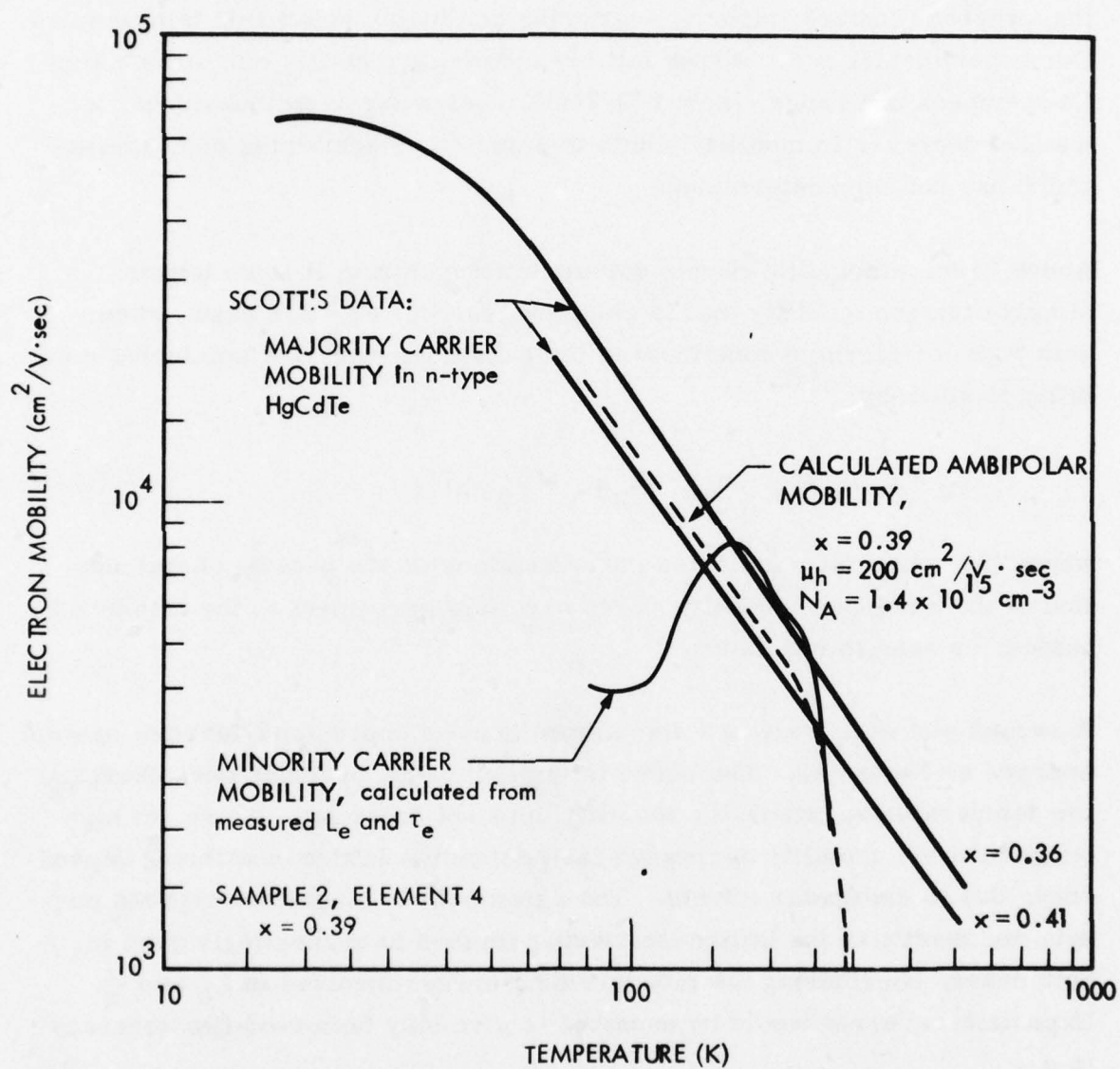


Figure 39. Temperature Dependence of Electron Mobility in n-Type $\text{Hg}_{1-x}\text{Cd}_x\text{Te}$ and p-Type Sample 2

Scott, ⁽³⁴⁾ who measured majority carrier electron mobility in high purity, low carrier concentration n-type HgCdTe, of similar composition. Scott's measurements show mobility above 50K to be determined by lattice scattering, whereas ionized impurity scattering dominates below this temperature. Our experimental curve shows lattice-scattering mobility only over a limited temperature range, from 170-240K. Below these temperatures, a marked decrease in mobility points to some other scattering mechanism, which has not been determined.

Above 240K, ambipolar effects dominate the mobility; it is no longer simply electron mobility that is being measured. For this case, when both types of carriers contribute to the p-side current, the ambipolar mobility is given by:⁽³⁵⁾

$$\mu_a = \mu_e \mu_h (p_p - n_p) / (n_p \mu_e + p_p \mu_h) \quad (53)$$

where the subscript p indicates concentrations on the p-side. A calculation of the ambipolar mobility shows excellent agreement to the measured values, as seen in the figure.

A second plot of μ_e versus T for a more heavily doped zone-levelled sample appears as Figure 40. The curve is similar to the previous one, except at low temperatures, where the mobility does not decrease. Again, at high temperatures, mobility decreases faster than the lattice-scattering dependence, due to ambipolar effects. The agreement in magnitude between our data and Scott's in the lattice-scattering regions is surprisingly good in both cases, considering the measurement errors involved in L_e and τ_e . Experimental error would be expected to give only factor-of-two accuracy in μ_e .

34. W. Scott, J. Appl. Phys. 43, 1055 (1972).

35. S. M. Sze, "Physics of Semiconductor Devices," John Wiley and Sons, New York (1969), Chapter 3, eqn. (37).

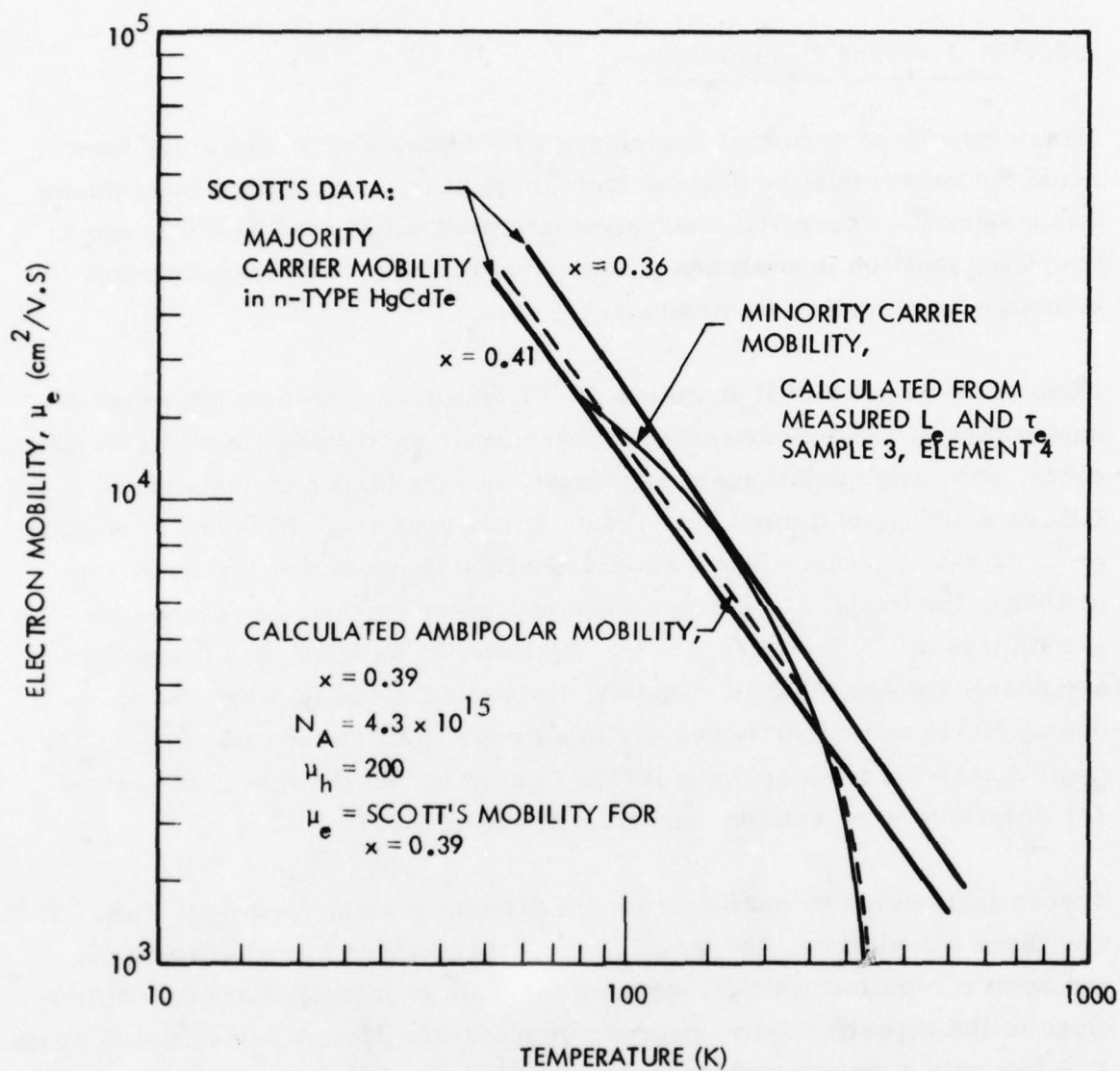


Figure 40. Temperature Dependence of Electron Mobility in n-Type $\text{Hg}_{1-x}\text{Cd}_x\text{Te}$ and p-Type Sample 3

6.5 $R_0 A$

6.5.1 $R_0 A$ versus Temperature

Measurements of zero bias resistance as a function of temperature were made for representative devices from most of the arrays fabricated during this program. Generally, measurements were made for $T > 170K$, due to very high junction impedances at low temperatures. The measurement technique is described in Section 5.5.

Figures 41-44 present $R_0 A$ versus $10^3/T$ data for devices with a range of doping levels. The temperature dependence is essentially the same in all cases, with only variations in magnitude. At the higher temperatures, $R_0 A$ follows a diffusion-limited slope, with a temperature dependence of roughly n_i^{-2} , or $\exp(E_g/kT)$. Below some transition temperature (in the vicinity of 190K), the temperature dependence is less steep, and approaches the g-r limit of n_i^{-1} , or $\exp(E_g/2kT)$. Because the x-value, and hence E_g , are nearly the same for all samples, the variations in $R_0 A$ are due to the doping levels and minority carrier properties (lifetime and mobility). The main conclusion to be drawn from the figures is that the theory of Section 2.1 describes very well the operation of actual diodes.

Theoretical curves in the figures were calculated using Equations 9 and 12. For these calculations, the temperature dependencies of radiative lifetime and Scott's reported mobility were used. This is justified because both are close to the experimentally observed temperature dependencies, and because $R_0 A$ has only a square root dependence on τ_e/μ_e . Relative magnitudes of the curves have been scaled to fit the data, and to reflect the differences between theoretical and experimental τ_e and μ_e . Note that in these figures N_D is the doping on the n-side of the junction, while N_A is really $N_A - N_D$ on the p-type side of the junction.

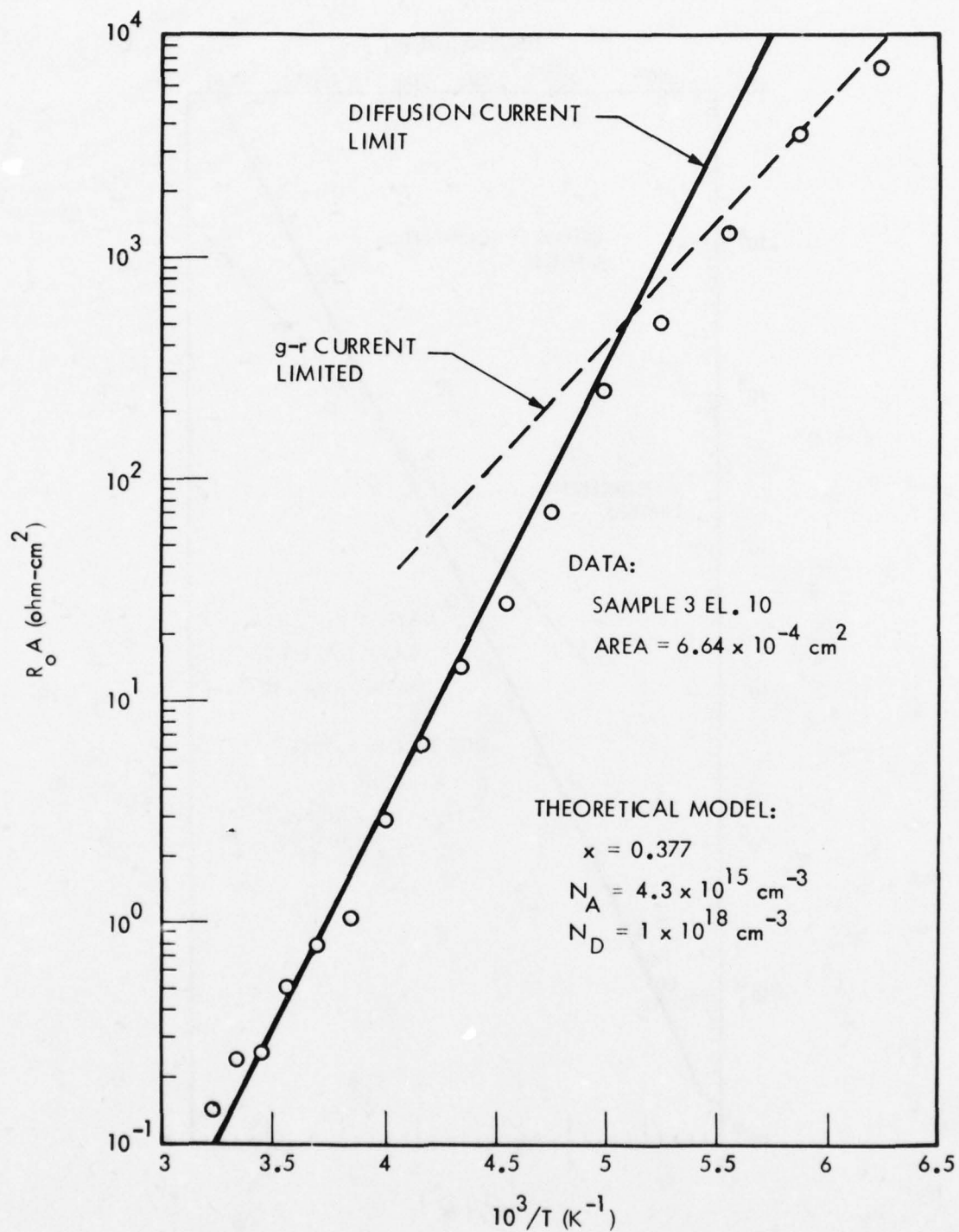


Figure 41. Temperature Dependence of $R_o A$ for Sample 3

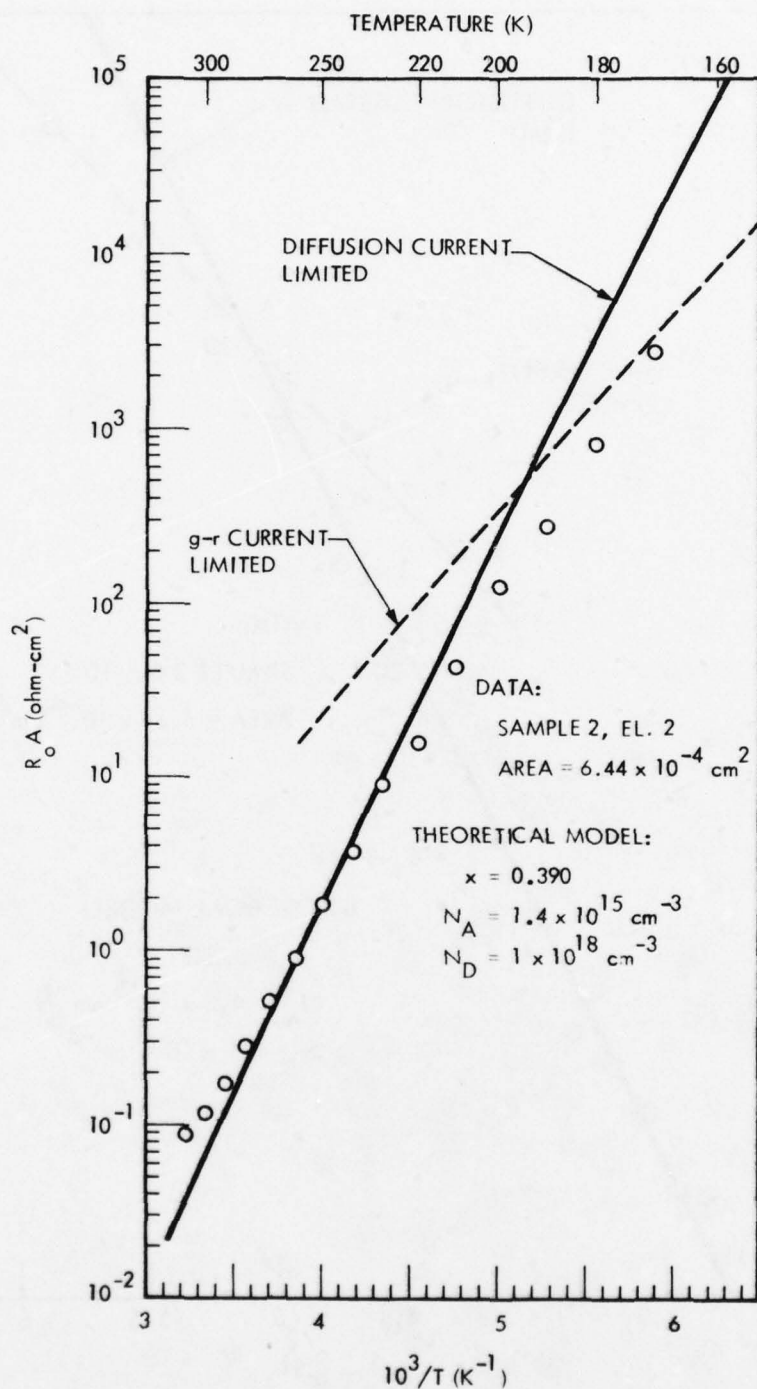


Figure 42. Temperature Dependence of $R_o A$ for Sample 2

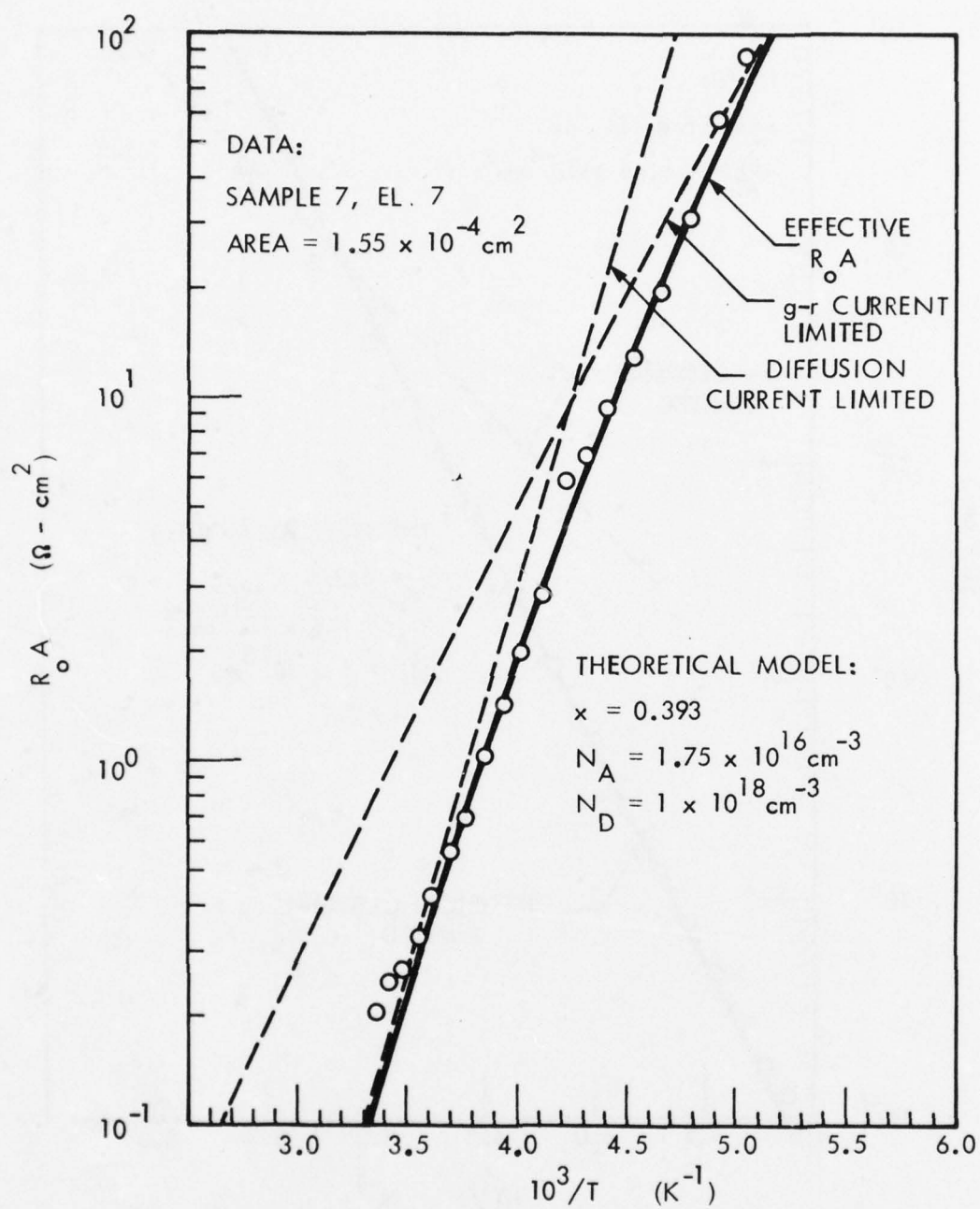


Figure 43. Temperature Dependence of $R_o A$ for Sample 7

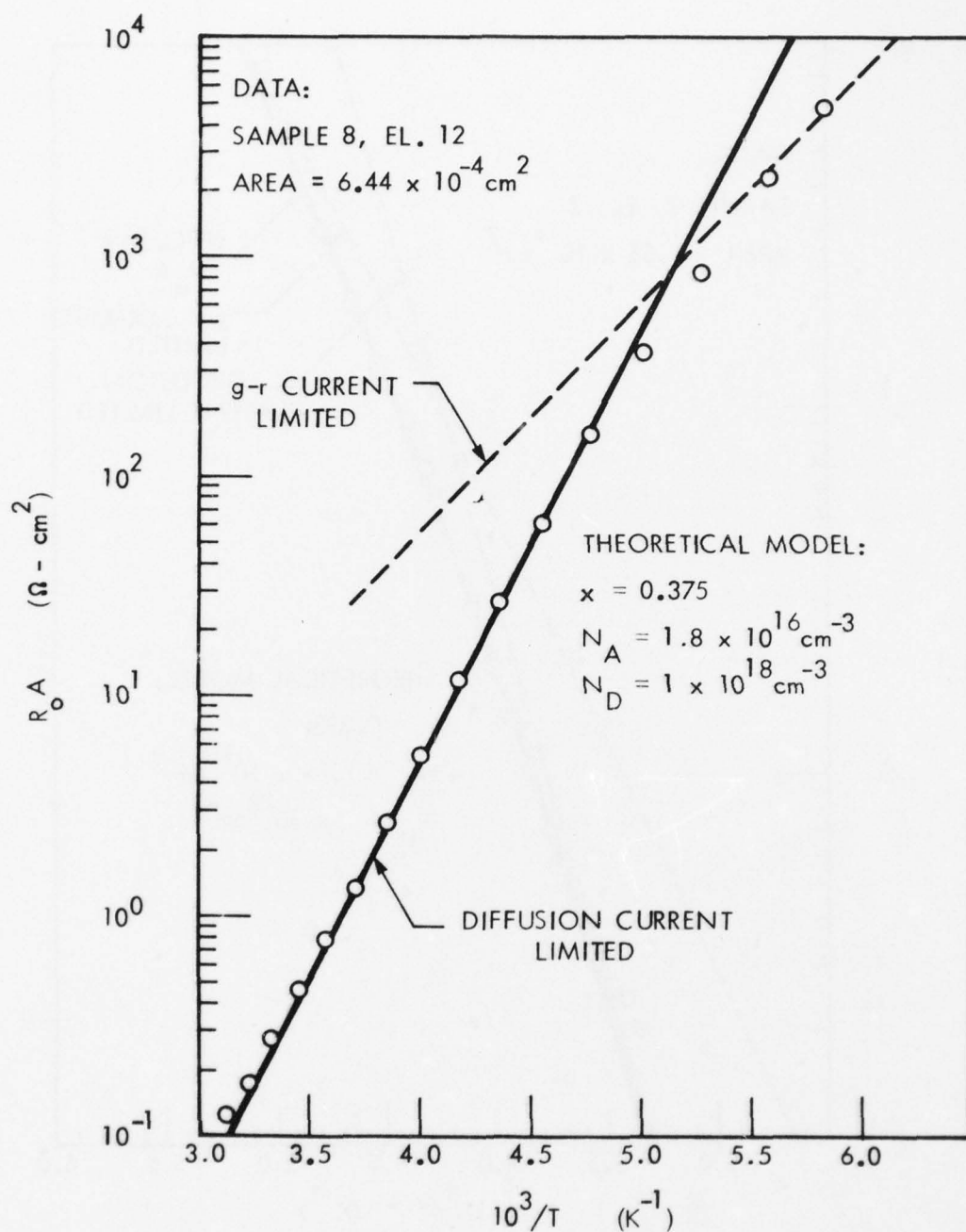


Figure 44. Temperature Dependence of $R_o A$ for Sample 8

6.5.2 $R_O A$ versus Carrier Concentration

Extensive $R_O A$ measurements were carried out at the boiling temperature of Freon 13 (193K) for material with a range of carrier concentrations. Below 193K, R_O values were 10^7 ohms and above, making measurements more difficult. $R_O A$ versus $N_A - N_D$ data at 193K are presented in Figure 45. Each error bar represents a multielement array, with the mean value indicated. Pertinent data on the arrays appear in Table 6.

At 193K, $R_O A$ increases with $N_A - N_D$ over most of the scale, following roughly an $(N_A - N_D)^{1/2}$ dependence. This is to be expected, as the diodes are generally diffusion-limited at 193K (or making the transition to g-r). For diffusion-limited operation, $R_O A \propto N_A \sqrt{\tau_e}$, and τ_e has been found to have an $(N_A - N_D)^{-1}$ dependence. For noncompensated material, we should then have $R_O A \propto N_A^{1/2}$. The major point of deviation from this curve is sample 11 (52374, K5), which was doped by copper to $\sim 2.8 \times 10^{16} \text{ cm}^{-3}$ and had $R_O A = 100 \text{ ohm cm}^2$. $R_O A$ versus temperature measurements show these devices are not entirely diffusion-limited at 193K, but have a sizable g-r component. This accounts for the lower $R_O A$ and we did not plot the point in Figure 45.

6.5.3 $R_O A$ Uniformity

The uniformity in measured $R_O A$ for several multielement arrays can be seen in Figure 45. Variations in $R_O A$ across an array can be as much as a factor of five. These differences arise from two sources. First, there are variations in N_A , τ_e , μ_e , and n_i in the material, which would cause a distribution of $R_O A$ even for perfect junction structures. Second, imperfections in the junctions themselves (surface leakage, early breakdown, implant damage, grain boundaries across the junction) can vary from element to element, causing differences in $R_O A$. The extremes in $R_O A$ seen for each array are most likely due to the latter source. However, our measurements of the material parameters also show a good deal of variation; better

control of $R_0 A$ uniformity requires both more uniform material, and better understanding of junction imperfections.

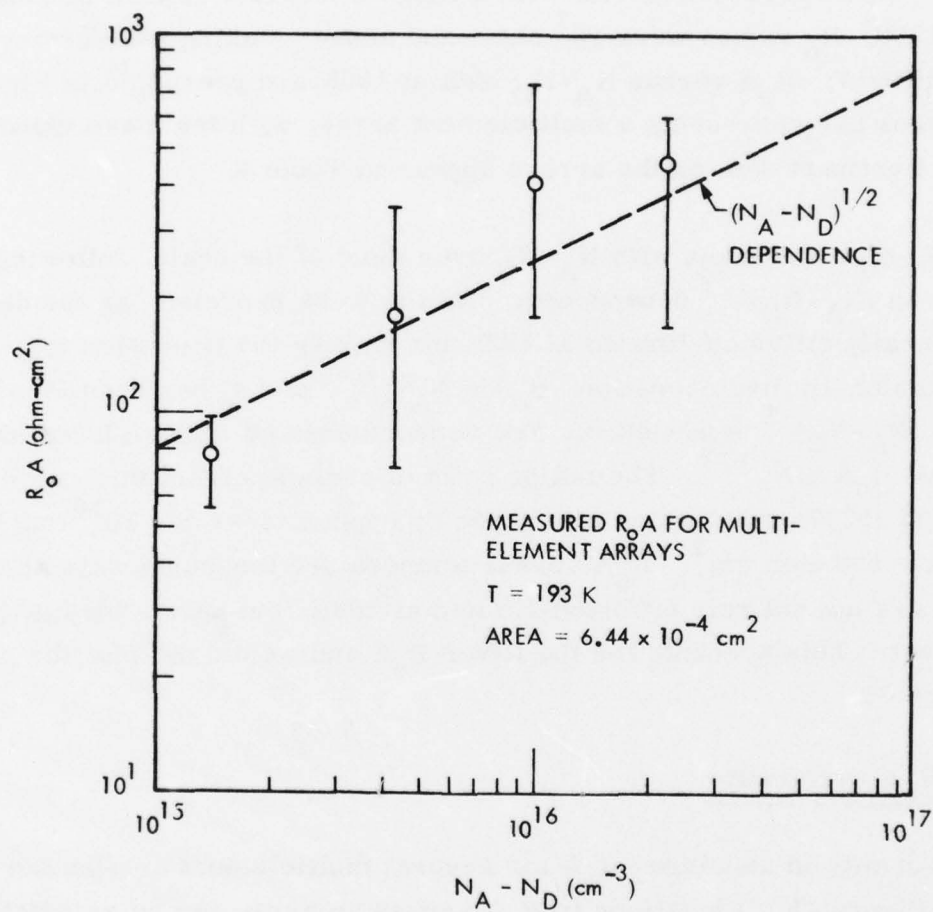


Figure 45. $R_0 A$ at 193K as a Function of Hole Concentration

SECTION 7 ANALYSIS

7.1 SHOCKLEY-READ RECOMBINATION ANALYSIS

The measurements reported in Section 6 have indicated a Shockley-Read recombination mechanism is responsible for the measured lifetimes. This conclusion was reached on the basis of magnitude of the lifetime, its temperature dependence, its doping dependence, and its dependence on injected carrier density (from Equation 22). In this section, the Shockley-Read mechanism and its implications will be examined in more detail.

7.1.1 Assumptions of the Model

The expression for Shockley-Read ⁽¹¹⁾ lifetime appeared in Section 2:

$$\tau_{S-R} = \frac{\tau_{p_0} (n_0 + n_1 + \nabla n) + \tau_{n_0} (p_0 + p_1 + \nabla n)}{(n_0 + p_0 + \nabla n)}$$

where the symbols have been previously defined. This expression is strictly valid only for a single, discrete recombination level in the forbidden gap at energy E_t . More than one discrete recombination level, or a band of levels around E_t would change the temperature and injection dependence of τ_{S-R} . The temperature dependencies shown in Section 6.2 suggest that indeed we do have a more complicated situation than the model assumes. Measured lifetimes generally show a more gradual increase with temperature than predicted by Equation 19, starting at a lower temperature. This suggests levels near (but below) E_t in the gap, which are less effective recombination centers.

Another assumption underlying Equation 22 is negligible density of recombination centers N_t , so that $N_t \ll p$ in p-type material. We cannot be sure this is the case for our samples. There is evidence that N_t is related to N_A , and hence p .

From the dependence of τ on N_A at low temperatures (Section 6.2.2), it was found that $N_t \propto N_A$. If the constant of proportionality is near or above 1, the assumption of small trap density is incorrect.

An order of magnitude estimate of N_t can be made using measured τ_{no} values. From Figure 20, we see $\tau_{no} \approx 45$ nsec, for $p = 10^{16} \text{ cm}^{-3}$. At 77K, $v_{th} = 5.91 \times 10^6 \text{ cm/s}$. Capture cross-sections σ_n are usually in the vicinity of 10^{-5} cm^2 . Then $N_t = 3.76 \times 10^{15} \text{ cm}^{-3}$, and N_t may indeed be comparable to p , depending on the value of the capture cross-section of the defect.

7.1.2 Fitting the Data

Equation 16 for Shockley-Read lifetime requires the parameters τ_{po} , τ_{no} , n_1 , and p_1 . These parameters are determined by the detailed nature of the S-R defect (capture cross-sections, trap density, and trap energy level), and can only be determined experimentally. Because these characteristics have not been measured for the S-R defect in (Hg, Cd) Te, our approach has been to treat them as variables in fitting the measured lifetime versus temperature. Figures 15, 16, and 17 illustrate the type of data and the resulting fits.

For p-type material with the trap level below midgap, τ_{po} is significant only for large values of ∇n . In the modelling done here, we are not really interested in τ_{po} , and have assumed $\tau_{po} = \tau_{no}$ for convenience. τ_{no} can be determined from the low temperature lifetime, which is essentially constant with temperature:

$$\tau_{S-R} = \tau_{no} \frac{(p_o + 2\Delta n)}{(p_o + \Delta n)} \quad (54)$$

For low-level injection, $\Delta n \ll p_o$, the measured lifetime is simply τ_{no} . The density of injected carriers Δn is known from the measurement conditions, as explained in Section 5.4. We assume, for simplicity, that Δn_o is temperature-independent; although v_{th} and probably σ_n in Equation 23 have some temperature dependence, the measured lifetimes at low temperatures are constant within experimental accuracy.

The other parameter found by fitting the data is E_t , the energy level of the S-R defect. Through p_1 in Equation 22, E_t determines the point at which the lifetime begins to increase with temperature. Therefore, the high temperature portion of the experimental τ_e versus T curve determines E_t , and the low temperature end determines τ_{no} .

In fitting the data, some degree of uncertainty is expected in the resulting τ_{no} and E_t . Δn is known only approximately, and the data do not follow exactly the Shockley-Read temperature dependence. A range of τ_{no} and E_t values then can be found to give equally reasonable fits to the data. However, these ranges are not unreasonably large. In the course of evaluating many τ_e versus T curves for 3.0- μm cutoff material, it has always been found that $E_t = 0.140 \pm .020$ eV gives the best fit. Values of τ_{no} depend on the doping level of the material, but worst case accuracy is expected to be within a factor of two of the nominal values.

7.1.3 Nature of the Defect

Shockley-Read defects in semiconductors have been found to arise from a large number of sources. They can be caused by electrically active impurity atoms, introduced either in the starting materials, the growth process, or subsequent processing. They can be caused by crystal defects of

any kind— either gross defects such as grain boundaries or dislocations, or point defects such as vacancies or interstitials. These defects may be due to the growth process or to later processing steps (such as work damage or ion implantation). In the face of all these possibilities, identifying the Shockley-Read defect is a formidable task.

Nevertheless, the results of this program allow us to make some definite conclusions about the nature of the defect. First, it cannot be due to gross crystal defects, such as grain boundaries or dislocations. Lifetimes have been found to be relatively position-independent across the wafers. Small-area devices used to measure lifetime have shown the defect must be relatively uniformly distributed in the material, down to a small scale.

It also seems unlikely that the defect is an electrically active impurity atom because of the dependence of lifetime on the acceptor concentration N_A . If an impurity were responsible, lifetime should depend on the concentration of the impurity atom, and not on the concentration of acceptors, which are assumed to be mercury vacancies produced by annealing. We would expect the lifetime to be independent of the acceptor concentration in that case.

The proportionality between N_t and N_A is the strongest clue to the identity of the Shockley-Read defect. Leaving aside the two copper-doped samples for the moment, the acceptors in these samples were all produced by annealing, and thus are stoichiometric in nature. They are thought to be singly-ionized mercury vacancies. Scott³⁶, et.al., have found the acceptor ionization energy to be about 14 meV, which is very close to the valence band edge and far removed from the S-R level at about 140 meV. (A diagram of the relevant energy levels is shown in Figure 46, for $x = 0.39$ HgCdTe at 200K.) Thus there seems to be no direct connection between the singly ionized acceptor and the defect level.

³⁶W. Scott, E.L. Stelzer, and R.J. Hager, J. Appl. Phys. 47, 1408 (1976).

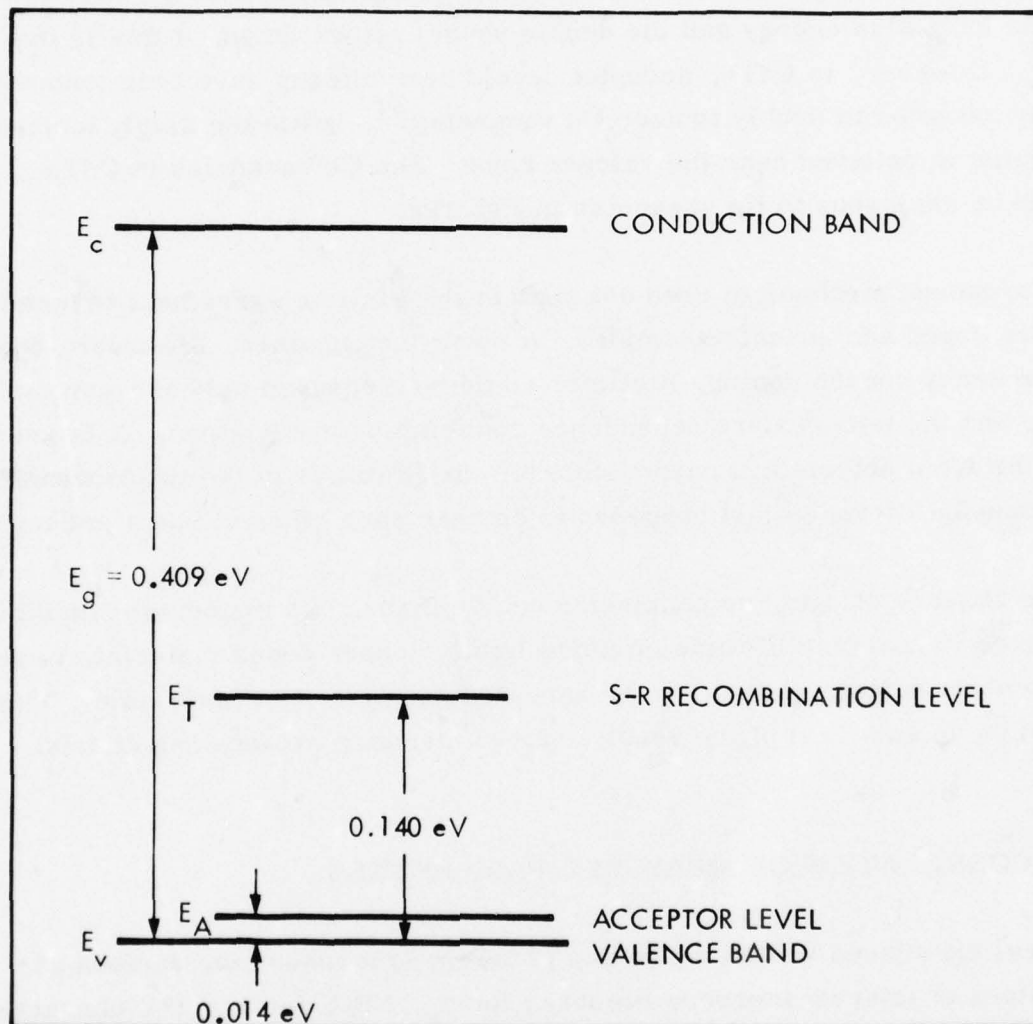


Figure 46. Schematic of the Energy Levels of $\text{Hg}_{0.61}\text{Cd}_{0.39}\text{Te}$ at 200K

However, mercury is a divalent atom, and it is possible that the doubly ionized acceptor level of the vacancy is associated with the Shockley-Read defect. This would explain the proportionality between the number of defect centers and the number of acceptors. The energy difference between the single ionization energy and the double seems rather large, if this is the case. However, in CdTe, acceptor levels near midgap have been tentatively assigned to doubly ionized Cd vacancies³⁷, while the singly ionized acceptor is believed near the valence band. The Cd vacancies in CdTe would be analogous to Hg vacancies in HgCdTe.

The proposed mechanism does not explain the lifetime agreement between copper doped and annealed samples, at room temperature. However, due to the heavy copper doping, lifetimes could be measured only at room temperature, and the temperature dependence could not be ascertained. It is possible that different defects are responsible for the lifetimes in the two materials, and that the lifetimes just happened to be near each other at room temperature.

In the absence of data, no conclusion can be made. An important experiment would be to measure lifetime on more lightly copper doped material, to see if the same defect, as that for the annealed samples, is responsible. This would be an easy test of the doubly ionized mercury vacancy hypothesis.

7.2 CORRELATION OF MEASURED PARAMETERS

Several techniques were used in this program to measure the various parameters of interest (reverse recovery for τ_e , EBIC for L_e , I-V characteristics for $R_o A$). These three parameters are not independent, but are related through equations for L_e and diffusion-limited $R_o A$:

³⁷K. Zanio, Semiconductors and Semimetals, Vol 13, ed. R.K. Willardson and A.C. Beer, Academic Press, New York (1978)

$$R_o A \text{ (diffusion)} = \frac{1}{q} \sqrt{\frac{kT}{q}} \frac{N_A}{n_i^2} \sqrt{\frac{\tau_e}{L_e}} \quad (55)$$

$$L_e = \sqrt{\frac{KT}{q}} \mu_e \tau_e \quad (56)$$

Equations 55 and 56 provide a check on the consistency of our measured values. If τ_e and L_e are truly the bulk minority carrier properties, and $R_o A$ is limited by diffusion current on the p-side, then 55 and 56 will be satisfied. Conversely, if large discrepancies (greater than experimental error) appear when the measured values are introduced in 55 and 56, then one or both of the following must be true: (a) the model for diffusion-limited $R_o A$ does not apply, or (b) the measured values for τ_e or L_e are not the bulk minority carrier lifetimes or diffusion lengths.

In practice, the measured parameters have proven to be consistent, within experimental error. For example, Figures 47 and 48 plot $R_o A$ versus temperature for two samples, comparing measured $R_o A$ with Equation 55. The values of τ_e and L_e versus temperature were experimentally determined, and appear as figures in Sections 6.1 and 6.2. The only exceptions are diffusion lengths at high temperatures (above 250K), where ambipolar effects make the measurement invalid. (See Section 6.3.) In this region, L_e was calculated from the measured lifetime, and a mobility extrapolated along the measured temperature dependence of Scott et al ⁽³⁶⁾.

The agreement between measured $R_o A$ and calculated values for diffusion-limited operation is quite good, in the temperature range above 180K. Below this temperature, the devices become g-r limited. Some deviation of the data from the calculated $R_o A$ also occurs at the high-temperature end, as series resistance in the devices becomes comparable to the rapidly-decreasing diffusion resistance. Because:

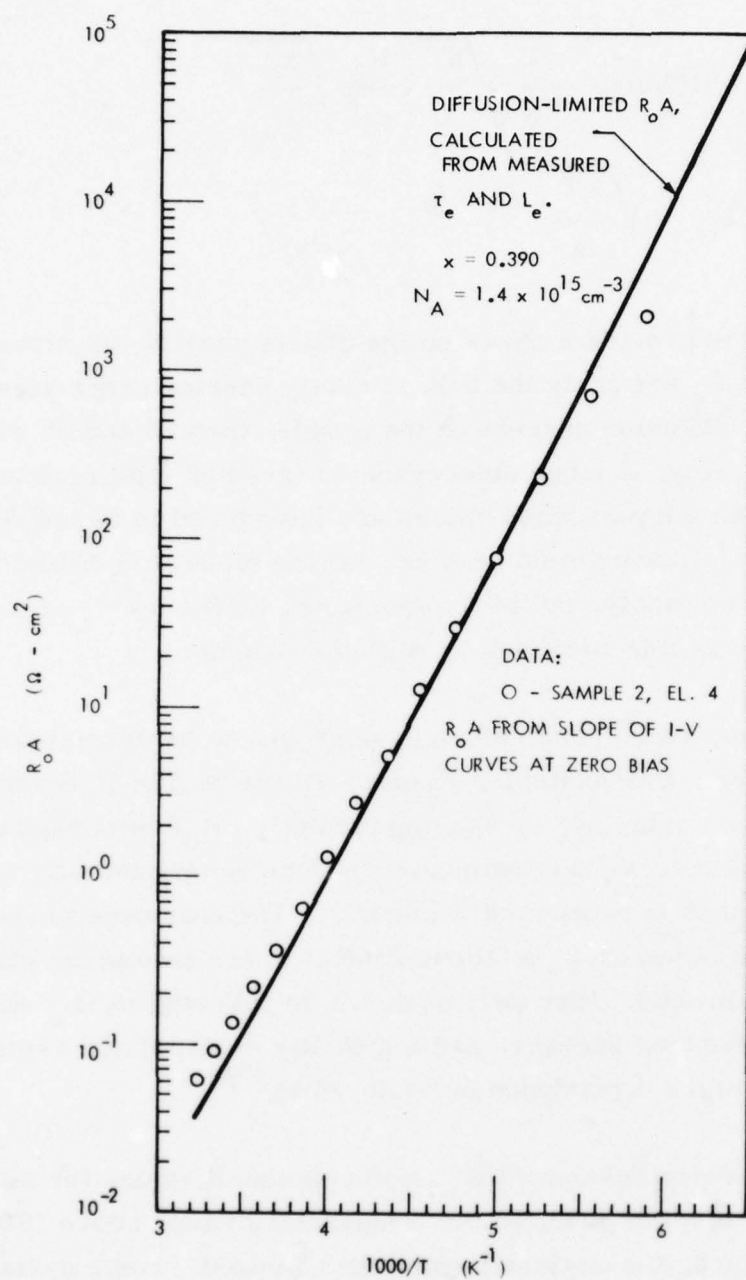


Figure 47. Temperature Dependence of R_0A of Sample 2 Compared to Diffusion-Limited R_0A Calculated From τ_e and L_e

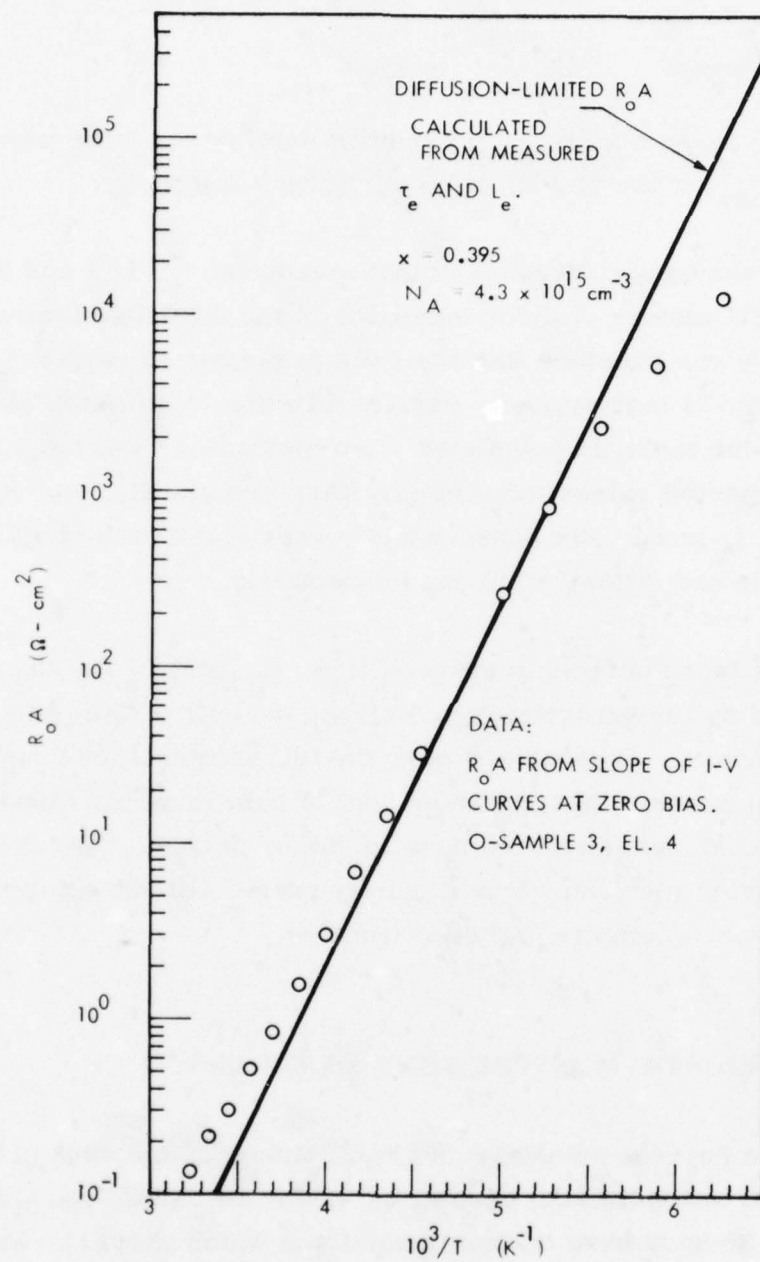


Figure 48. Temperature Dependence of $R_o A$ of Sample 3

$$R_{\text{meas}} = R_{\text{diff}} + R_{\text{series}} \quad (57)$$

The measured resistance (R_{meas}) becomes dominated by the series resistance (R_{series}) if the temperature is raised sufficiently.

Nevertheless, the important point is that measured τ_e , L_e , and $R_o A$ provide a consistent picture of diode operation in the diffusion-limited temperature range. We can conclude that the ratio of measured values τ_e/L_e is equal to the ratio of bulk minority carrier lifetime to diffusion length. Moreover, because the mobility calculated from measured τ_e and L_e is also consistent with expected values for minority carrier mobility, we can conclude that measured τ_e and L_e are independently very close to the bulk minority carrier lifetime and diffusion length, respectively.

The agreement found between measured $R_o A$, τ_e , and L_e for the devices in Figures 47 and 48 is characteristic of all the devices tested, when dominated by diffusion current. Comparison over the full temperature range was done for only a few elements, due to the amount of data involved, but spot checks at single temperatures have been done for many devices. We are, therefore, confident of having measured true minority carrier lifetime and diffusion length, for diodes which are diffusion-limited.

7.3 LIMITATIONS OF MEASUREMENT METHODS

While the diode reverse recovery and EBIC line scan methods proved to be the most useful techniques for measuring lifetimes and diffusion lengths in this program, they do have certain limitations which should be kept in mind when interpreting the results. The limitations should also be understood by potential users of these techniques.

7.3.1 Diode Reverse Recovery Technique

The reverse recovery technique does not automatically give accurate values of the minority carrier lifetime. Some care must be taken in making the measurements and interpreting the results. The following discussion is intended to illuminate some of the pitfalls.

7.3.1.1 Injected excess carrier density — The most serious limitation to interpreting measured lifetimes as the bulk minority carrier lifetime is the effect of injected carriers. Carrier lifetimes, whether radiative, Auger, or Shockley-Read, vary with the number of excess injected carriers in the material. What is usually meant by minority carrier lifetime is the lifetime for low-level injection, so that the excess carrier density ∇n is much smaller than the concentration of holes in equilibrium (in p-type material). The reverse recovery technique inherently injects a finite number of excess electrons into the p-region, when the diode is forward-biased. Whether or not the low-level conditions are satisfied depends on the measurement conditions and device being tested.

As discussed in Section 5.4, the injected carrier density is given approximately by

$$\nabla n = \frac{I_F \tau_e}{2qAL_e} \quad (58)$$

For a given piece of starting material, the two parameters which can be experimentally varied are the forward current I_F , and the junction area A . A lower limit is placed on I_F by the requirement that $I_F/I_R > 2$, to obtain good Kuno plots, and that I_R be significantly greater than the reverse saturation current. The latter requirement means I_F and I_R must be larger for higher temperatures; because τ_e/L_e also increases with temperature, injection is most important at high temperatures. The forward current also must be

high enough to ensure that the diffusion of injected carriers dominates the current flow after the bias is reversed, and not some leakage mechanism. Empirically, the forward current is lowered until the reverse recovery curves no longer show sharp, well-defined transitions at the end of the storage time t_s . In the work done here, a lower limit on I_F was typically a few milliamps.

The only other adjustable parameter is the junction area A , which should be as large as possible to minimize ∇n . Most of our devices were 9.5×10.5 mil², which proved large enough to give reasonable ∇n , and small enough to allow investigations of material uniformity. The relationship between area and ∇n is very important when interpreting data. Studies of lifetime versus junction area usually show lifetime decreasing for small-area devices; the lifetime decrease is due to increased injection, and not to any difference in the recombination physics.

Injection effects are less serious for more heavily doped material, both because $\nabla n/p$ is automatically smaller, and because τ_e/L_e will be smaller. The need for large areas and low currents is, therefore, relaxed.

Because the lifetime varies with ∇n , and hence I_F , the forward current must remain constant when making a Kuno measurement. The reverse current I_R is varied to give the necessary range of I_F/I_R values. ∇n should also remain constant when making measurements of lifetime versus temperature, but this is difficult because τ_e and L_e vary with temperature. In practice, I_F is kept constant throughout the measurement at a low value, and it is assumed that the resulting variations in ∇n will be small enough to have little effects on the results. The effect of significant ∇n on the Shockley-Read τ_e versus temperature curve is to lower the high-temperature lifetime; and raise the low-temperature end.

7.3.1.2 Range of measurable lifetimes -- The lower limit on measurable lifetimes is determined by the rise and fall times of the pulse generator and oscilloscope used in the measurement. For our equipment, this limit is about 25 nsec. More elaborate equipment could be used to extend the range. There is no real upper limit on the measurable lifetimes.

7.3.1.3 Limitations on diode current-voltage characteristics -- In general, diodes with poor I-V characteristics will give poor reverse recovery curves and unreliable lifetime results. Junction breakdown voltage should be large enough that the device can sustain the applied reverse voltage without significant leakage current. It is also important that the diode be dominated by bulk diffusion current or generation-recombination in the space charge region, and not by leakage currents in the surface or bulk. A high series resistance can also adversely affect the reverse recovery curves, by introducing an RC decay at the forward-to-reverse transition. For short lifetime material, this can completely hide the expected reverse recovery curve.

7.3.1.4 Surface effects -- We have seen no evidence that our measurements are affected by surface, as opposed to bulk, recombination. Correlations of measured lifetime, diffusion length, $R_0 A$, and mobility are consistent with bulk properties (see Section 7.2). Surface effects would be important if the surface recombination velocity s were comparable to the ratio of L_e / τ_e . Typical values for this ratio are $\frac{2 \times 10^{-3} \text{ cm}}{10^{-7} \text{ sec}} = 2 \times 10^4 \text{ cm/sec}$.

Surface recombination velocities measured by MIS transient techniques, however, are typically in the range of 10^1 - 10^3 cm/sec. Therefore, surface recombination should not limit the lifetime.

7.3.1.5 Absolute accuracy of measured lifetimes -- There are several factors which limit the absolute accuracy of the measurements. One is the injected carrier density, explained earlier in this subsection. Assuming we

have satisfied low-level injection conditions, other inaccuracies arise because we do not have an ideal abrupt junction (Kuno versus Kingston methods). This was discussed at length in Section 5.4, with the conclusion that numbers resulting from Kuno's treatment are expected to be more accurate than from Kingston's, but the experimental discrepancy between the two does not exceed a factor of two. Experimental errors are also introduced in reading I_F , I_R , and t_s from the scope traces, and in taking slopes from Kuno plots. However, the consistent results we have obtained in computing $R_0 A$ and mobility from measured lifetimes indicate that these lifetimes are not far removed from the actual values. A reasonable estimate of the reliability of the measurements is a factor-of-two accuracy for lifetimes evaluated by Kuno's method. Kingston lifetimes typically over-estimate Kuno's by up to a factor of two.

7.3.2 EBIC Line Scan Technique

7.3.2.1 Surface recombination -- The line scan technique is particularly vulnerable to surface recombination effects, as the carrier-generating electron beam is scanned directly along the surface. In silicon, where the surface recombination velocity is relatively high, this is a major effect. Consequently, other techniques have been developed, such as varying the electron energy to vary the penetration depth beneath the junction, instead of along the surface. (Our SEM does not have the range of electron energies necessary to use this technique.) However, in $\text{Hg}_{1-x}\text{Cd}_x\text{Te}$, surface recombination velocities can be shown to be relatively insignificant on passivated surfaces (see preceding subsection). Surface recombination is, therefore, not expected to influence the measured diffusion length.

We have some experimental evidence that this is the case. On one sample, EBIC scans were made using a 25 KeV beam voltage (our standard value), and then 15 KeV. The 15-KeV electrons are absorbed nearer the device

surface, and would be expected to give a shorter diffusion length if surface recombination is significant. In fact, the observed difference in L_e was only a few percent, well within experimental error. The second indication that surface recombination is not important comes from the agreement between EBIC and BITS results for diffusion length. BITS measures diffusion length in the bulk, and is not affected by surface recombination. BITS measurements on sample 7 ($N_A - N_D = 1.75 \times 10^{16} \text{ cm}^{-3}$) gave $L_e \approx 14 \mu\text{m}$ at 175K. EBIC measurements on similar material, sample 6 ($N_A - N_D = 1.6 \times 10^{16} \text{ cm}^{-3}$), gave $L_e = 12-13 \mu\text{m}$ at this temperature. The discrepancy is within the experimental error for either technique. We conclude that surface recombination does not significantly affect our L_e measurements.

7.3.2.2 Temperature limitations -- Temperature limitations on the EBIC technique come in two forms: those imposed by the temperature-controlling equipment, and those imposed by the validity of the measurement. With the present system, extended measurements at a stable temperature can be made at 80K and room temperature. This limits studies of L_e uniformity to one of these temperatures. Between these temperatures, the temperature can be raised slowly enough to accurately obtain L_e versus temperature data on a given element, but not on several elements. The variable-temperature measurements take up a considerable amount of time as the system is warming.

The measurement itself runs into trouble above about 250K, as the material approaches an intrinsic condition, and ambipolar effects become important. The measured diffusion length starts to decrease with temperature, instead of increasing. This means that L_e measurements are not valid in terms of the electron diffusion length at room temperature, and that the device must be cooled to obtain valid results. Quick testing of diffusion lengths is, therefore, not possible.

7.4 COMPARISON WITH RESULTS FOR OTHER $\text{Hg}_{1-x}\text{Cd}_x\text{Te}$ COMPOSITIONS

7.4.1 Shockley-Read versus Radiative

Reverse recovery lifetime measurements at the Electro-Optics Center have invariably shown the lifetime mechanism to be Shockley-Read. Measurements have been made on $x = 0.2$ to 0.4 material, corresponding to cutoff wavelengths from 11 to $3\text{ }\mu\text{m}$. Measured lifetimes are less than the calculated radiative lifetimes, and the temperature dependence is that of a Shockley-Read mechanism. It has been noted that the measured lifetimes are closer to the radiative limit for small x -value material than for large x -value. This is opposite of what one would expect: that a larger bandgap would lead to a longer lifetime. Thus, the low-temperature lifetime τ_{no} will be larger for $x = 0.2$ than for $x = 0.4$ material. Either the capture cross-section for electrons or the number of S-R defects must be higher for higher x -value material.

7.4.2 Energy Level of S-R Defect

The energy E_t of the defect is not the same for all compositions, but rather varies with the bandgap. Typical values found for E_t from lifetime versus temperature data are 140 meV for $x = 0.39$ ($E_g \approx 0.41\text{ eV}$), 110 meV for $x = 0.30$ ($E_g \approx 0.28\text{ eV}$), and 50 meV for $x = 0.20$ ($E_g \approx 0.12\text{ eV}$). Lifetime versus temperature data for $x = 0.326$ diodes are shown in Figure 49. The energy level maintains its relative position in the gap, between one-third and one-half of E_g above the valence band. The energy level is always found to be below midgap.

Some preliminary data from DLTS measurements of an $x = 0.326$ diode have shown agreement with our values of the defect energy level. Figure 50 shows the data, which indicates some type of electron traps at 200 and 160

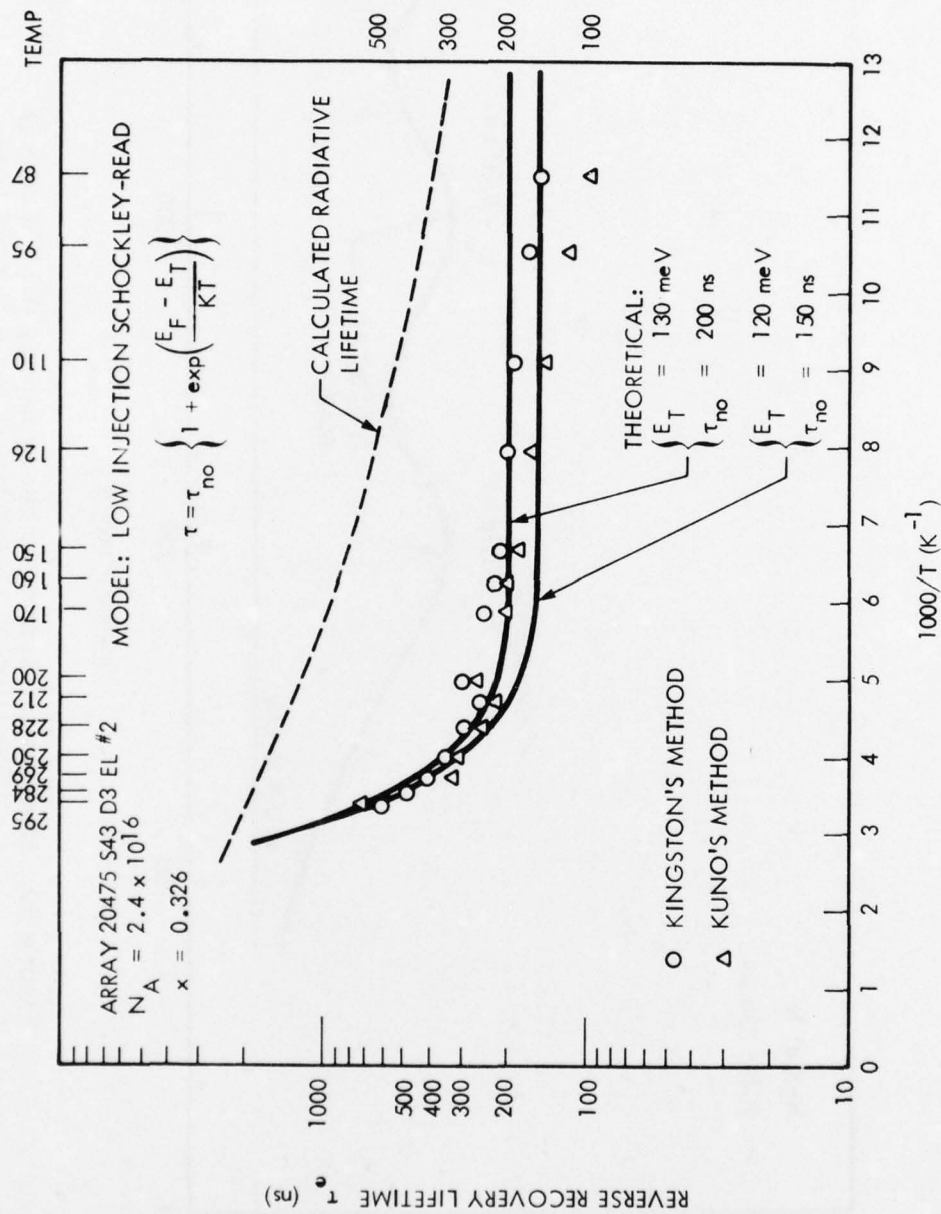


Figure 49. Temperature Dependence of Minority Carrier Lifetime of a Sample of Hg_{0.674}Cd_{0.326} Te by Kingston's and Kuno's Methods

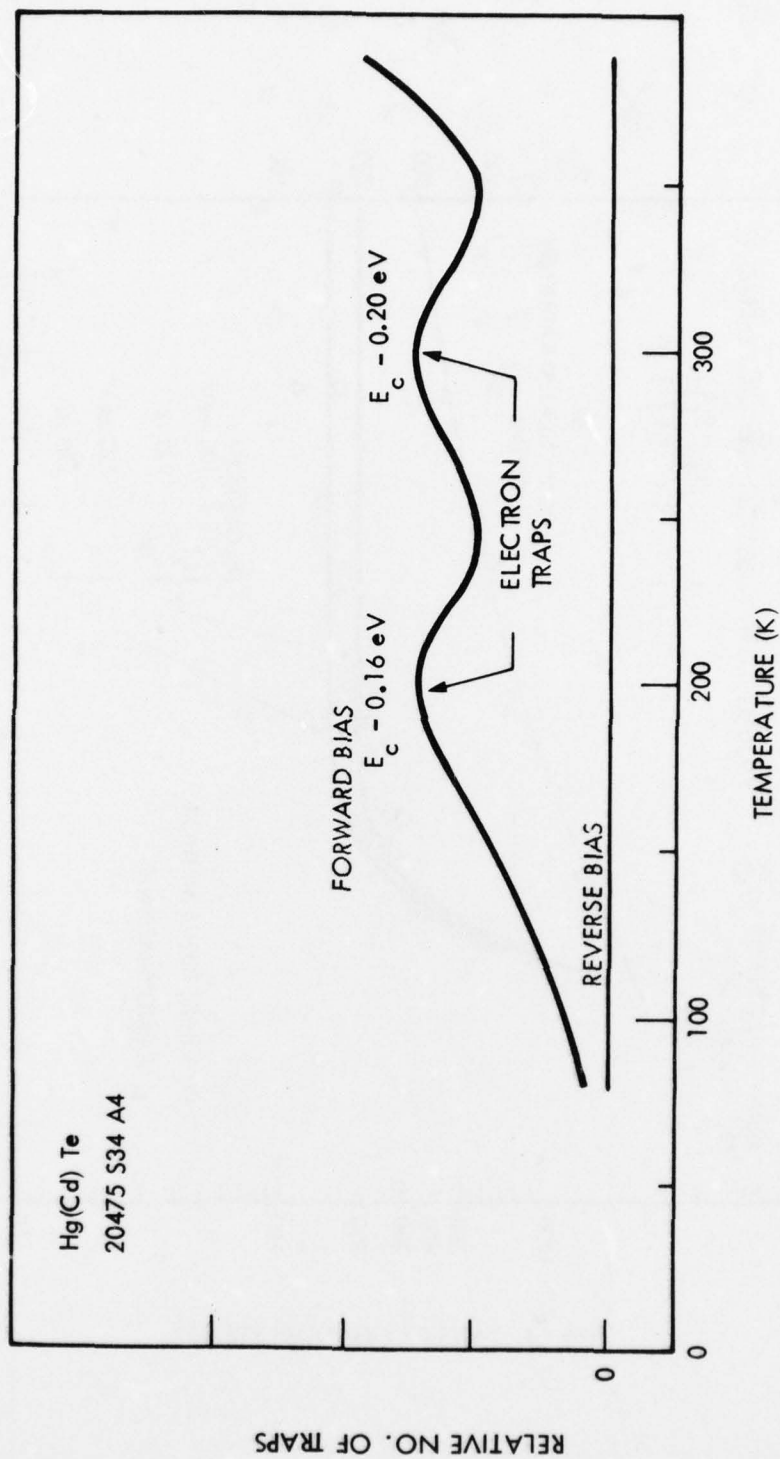


Figure 50. Deep Level Transient Spectroscopy (DLTS) Signal as a Function of Temperature for a Sample From Crystal 20475

meV below the conduction band or 120 and 160 meV respectively above the valence band. Lifetime versus temperature data on diodes from material of the same crystal indicated an E_t between 120 and 130 meV above the valence band. Figure 51 sketches the positions of the levels in the gap. It should be remarked that the DLTS results presented here are more qualitative than quantitative, and that further measurements and analysis are necessary to determine the trap parameters accurately. However, the agreement seen between the two dissimilar techniques is encouraging.

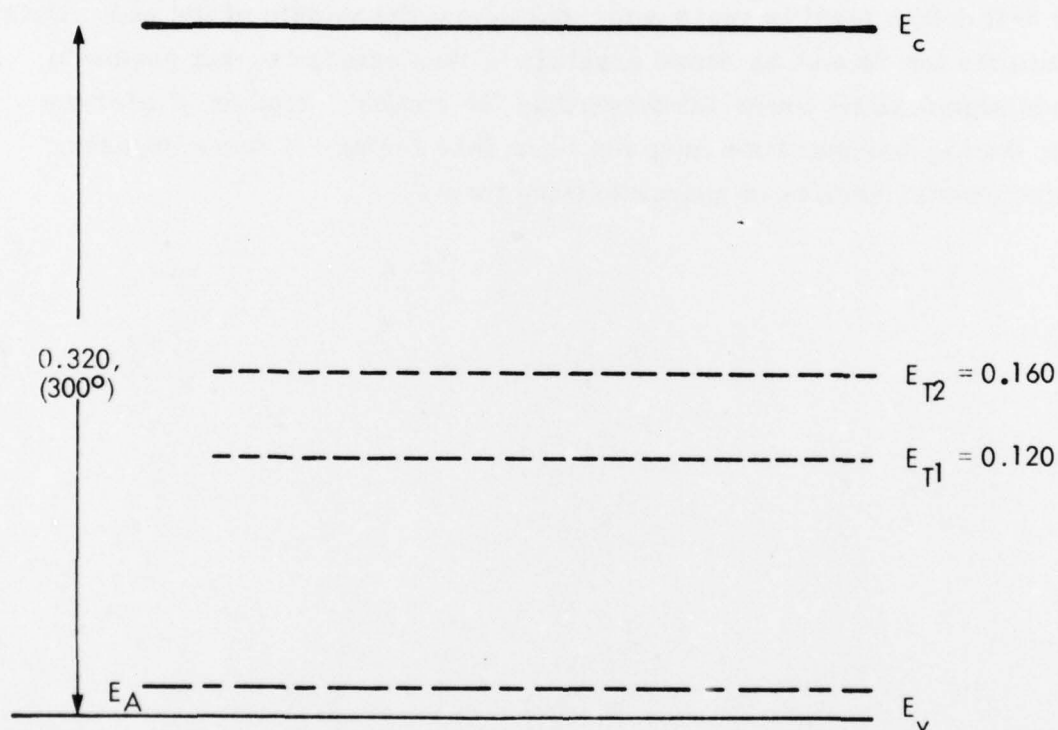


Figure 51. Schematic of the DLTS Energy Levels in the Bandgap of Crystal 20475

7.4.3 Other Dopants

While most of the measurements have been made on material doped by annealing, some lifetime data exist for material doped in the melt by acceptor impurity atoms. Copper-doped crystals have been grown for $x = 0.2$ and $x = 0.3$, and represent most of the impurity-doped material. Lifetime versus temperature data show a Shockley-Read dependence, with values of lifetime roughly comparable to the material doped by annealing. The location of the S-R defect level is again near, but below, the middle of the gap. Data on lifetimes for Sb and As doped crystals is less extensive, but seems to indicate significantly lower lifetimes than for copper. Studies of lifetime versus doping concentration have not been done for any of these dopants, and much work remains in characterizing them.

SECTION 8
CONCLUSIONS AND RECOMMENDATIONS FOR
DEVICE DESIGN AND FUTURE WORK

8.1 CONCLUSIONS

The major conclusions of this work are the following:

- (1) The recombination mechanism in p-type $\text{Hg}_{0.61}\text{Cd}_{0.39}\text{Te}$ is Shockley-Read, not radiative. This is demonstrated by the magnitude of the lifetime, and its dependencies on temperature, carrier concentration, and injected carrier density.
- (2) The number of Shockley-Read recombination centers is proportional to the number of acceptors for material doped p-type by stoichiometry.
- (3) The energy level of the recombination center is approximately 140 meV above the valence band edge.
- (4) At temperatures up to about 200K, lifetime depends on the acceptor concentration as $\tau_e \propto N_A^{-1}$. This holds for both quench/anneal and zone-levelled material. At higher temperatures, the dependence approaches $\tau_e \propto N_A^{-2}$.
- (5) Below 200K, diffusion length depends on the acceptor concentration as $L_e \propto N_A^{-1/2}$ for both Q/A and zone-levelled materials.
- (6) In all but the most compensated samples, τ_e and L_e are quite uniform (± 10 percent).
- (7) Electron mobility (μ_e) in p-type $\text{Hg}_{0.61}\text{Cd}_{0.39}\text{Te}$ equals μ_e in n-type material, within experimental error.

- (8) At 193K, R_0A depends on p-side doping as $R_0A \propto (N_A - N_D)^{1/2}$, up to at least $N_A - N_D = 2 \times 10^{16} \text{ cm}^{-3}$. Diodes are generally diffusion-limited at this temperature.
- (9) Diode reverse recovery is a powerful method for measuring minority carrier electron lifetime using n^+ -on-p junctions. EBIC line scans can be used to determine electron diffusion lengths in p-type $\text{Hg}_{0.61}\text{Cd}_{0.39}\text{Te}$. Both methods have the advantage of being directly applicable to existing junctions—no special device structures are needed.

8.2 RECOMMENDATIONS FOR DEVICE DESIGN AND FUTURE WORK

Three conclusions of this program directly affect device design: the dependence of R_0A on doping; the fact that lifetimes are limited by Shockley-Read, rather than radiative recombination; and the connection of the S-R defect with the stoichiometric acceptor concentration. The first of these implies that more heavily doped p-type material should be used for n^+ -on-p diodes to achieve the highest R_0A . At 193K, an improvement in R_0A was obtained for $N_A - N_D$ up to $2 \times 10^{16} \text{ cm}^{-3}$; above this level, the diodes were not diffusion-limited, so that no definite conclusion is possible. At high enough doping levels, R_0A will begin to decrease due to junction leakage, caused by tunneling or avalanche mechanisms; an optimum doping level then exists for highest R_0A . This level has yet to be determined.

Identification of the lifetime mechanism as Shockley-Read rather than radiative means R_0A improvement is possible through elimination of the S-R defect. For $x = 0.39$ material, R_0A can be improved by a factor of 4 or 5 by achieving radiative lifetimes. The implication for device design is straightforward: to achieve higher R_0A , we must have starting material with longer lifetimes.

There are several ways to go about improving the lifetime. The first is to stop doping the material by stoichiometric anneals, since the number of S-R recombination centers has been shown to be proportional to the number of stoichiometric acceptors.

The formation of vacancies and other lattice defects, which might be expected to act as recombination sites, is known to be enhanced at high temperatures; therefore, such processing should be avoided. Instead, more effort should be put into doping by acceptor impurity atoms. Several atoms which act as acceptors in $\text{Hg}_{1-x}\text{Cd}_x\text{Te}$ have already been identified^(13, 38) (Cu, As, Li, P). Their effects on lifetime, however, have not been determined adequately. Studies like this one, looking at lifetime as a function of temperature and doping, need to be done for the various acceptor dopants. Dopants may be found which do not introduce deep Shockley-Read levels into the energy gap, allowing the lifetime to be determined by radiative recombinations. Of course, other defects or impurities, less effective than the one now limiting lifetime, may be uncovered. The first step, however, is to eliminate the defect we have some knowledge of.

A second approach to improving the lifetime is to utilize alternate growth methods to the Q/A and zone-levelling techniques. LPE holds particular promise here. By growing films at low temperatures, the formation of vacancies and other lattice defects is greatly reduced. The material is doped in the melt with acceptor impurities, and stoichiometric doping is avoided. Research into the effect of various dopants on lifetime will still be needed, however.

In order to independently verify the existence of the Shockley-Read level, and determine parameters of the defect such as capture cross-section,

(38) E. S. Johnson and J. L. Schmit, J. Electronic Materials, 6, 25 (1977).

number of traps, and trap energy, other measurement techniques are needed. In particular, Deep Level Transient Spectroscopy (DLTS) seems promising as a means to further investigate the deep recombination level(s) in (Hg, Cd)Te. This will be particularly useful if various acceptor dopants are examined for their effects on lifetime. Then measured lifetimes can be related directly to properties of the recombination centers.

APPENDIX A

METHODS FOR EXTRACTING LIFETIME FROM REVERSE RECOVERY DATA

Table A1 lists 14 papers dealing with the determination of lifetime using diode reverse recovery data. Comments on the validity of each technique are included. In this report we have used mainly the methods of Kingston and of Kuno as detailed in Section 5.4.

Table A1. Methods for Extracting Lifetime from Reverse Recovery Data

Ref.	Author(s)	Junction Type	Base Width	Comments
A1.	Kingston (1954)	Abrupt	Very large	Original Paper
A2.	Lax, Neustadter (1954)	Abrupt	Very large	More rigorous treatment
A3.	Byczkowski, Madigan (1957)	Abrupt	Arbitrary	Infinite series expression
A4.	Ko (1961)	Abrupt	Narrow	Uses wrong boundary condition, derives Kingston's result.
A5.	Grove, Sah (1964)	Abrupt	Very Narrow	Approximations for $W \ll L_e$
A6.	Davidson (1966)	Abrupt	Arbitrary	Approximate expression
A7.	deSmet, vanOverstraeten (1975)	Abrupt	Arbitrary	Approximate expressions
A8.	Lewis (1975)	Abrupt	Narrow	Error analysis of various expressions
A9.	Moll, Krakauer, Shen (1962)	Graded	Narrow	Results do not fit our data
A10.	Muto, Wang (1962)	Graded	Very Narrow	Neglects recombination; cannot find lifetime
A11.	Moll, Hamilton (1969)	p-i-n	Not Specified	Results do not fit our data
A12.	Kennedy (1962)	Whole Range	Arbitrary	Complete mathematical treatment; need computer.
A13.	Kuno (1964)	Whole Range	Arbitrary	Assumes " τ_R " constant; easily applied.
A14.	Dean, Nuese (1971)	Whole Range	Arbitrary	Approximations of questionable usefulness.

REFERENCES

1. D. Long, "Photovoltaic and Photoconductive Infrared Detectors," in Topics in Applied Physics, Volume 19: Optical and Infrared Detectors, pp 101-147 (Springer-Verlag, Berlin Heidelberg, 1977); the p⁺ - p⁻ backside contact is discussed on pp. 110-112.
2. "Detection of Long Wavelength Infrared at Moderate Temperatures," Final technical report, NASA Johnson Space Center Contract NAS9-14180, Mod. 5S, April, 1977 in particular, see Section 2.3.
3. D. Long, T.J. Fredwell and J.R. Woodfill, "Detectivity vs Temperature in Infrared Photo Detectors," Proceedings of the Joint Meeting of the IRIS Specialty Groups on Infrared Detectors and Imaging-Volume 1; 13-15 June, 1978, pp. 387-400.
4. C.T. Sah, R.N. Noyce and W. Shockley, "Carrier Generation and Recombination in P-N Junctions and P-N Junction Characteristics," Proc. IRE 45, 1228 (1957); see Equation 28, p. 1234.
5. P.E. Petersen, "Auger Recombination in Hg_{1-x}Cd_xTe," J. Appl. Phys. 41, 3465 (1970).
6. M.A. Kinch, M.J. Brau and A. Simmons, "Recombination Mechanisms in 8-14 μ m HgCdTe," J. Appl. Phys. 44, 1649 (1973).
7. P.E. Petersen, Final Report, AFOSR Contract F49620-77-C-0028, Feb. 1979.
8. Blakemore, J.S., Semiconductor Statistics, Pergamon Press, Oxford (1962) Chapter 6.
9. W. vanRoosbroeck and W. Shockley, "Photon-Radiative Recombination of Electrons and Holes in Germanium," Phys. Rev 94, 1558 (1954).
10. R.N. Hall, Proc. Inst. Electr. Eng. B Suppl. 106, 923 (1959).
11. W. Shockley and W. F. Read, Jr., "Statistics of the Recombinations of Holes and Electrons," Phys. Rev. 87, 835 (1952).
12. J.C. Ayache and Y. Marfaing, Compt. Rend. Acad. Sci. B265, 568 (1967).
13. J.L. Schmit and E.S. Johnson, "Exploratory Development on Hg_{1-x}Cd_xTe Improvement" Phase II, March 1977, AFML-TR-77-21.

31. J. L. Moll, S. Krakauer and R. Shen, Proc. IRE 50, 43 (1962).
 32. J. L. Moll and S.A. Hamilton, Proc. IEEE 57, 1250 (1969).
 33. W. H. Hackett, Jr., R.H. Saul, R.W. Dixon, G.W. Kammlott, J. Appl. Phys. 43, 2857 (1972).
 34. W. Scott, J. Appl. Phys. 43, 1055 (1972).
 35. S.M. Sze, Physics of Semiconductor Devices, John Wiley and Sons, New York (1969), Chapter 3, eqn. (37).
 36. W. Scott, E. L. Stelzer, and R.J. Hager, J. Appl. Phys. 47, 1408 (1976).
 37. K. Zanio, "Semiconductors and Semimetals," Vol 13, ed. R.K. Willardson and A.C. Beer, Academic Press, New York (1978).
 38. E.S. Johnson and J.L. Schmit, J. Electronic Mater. 6, 25 (1977).
-
- A1 R.H. Kingston, Proc. IRE 42, 829 (1954).
 - A2 B. Lax and S.F. Neustadter, J. Appl. Phys. 25, 1148 (1954).
 - A3 M. Byczkowski and J.R. Madigan, J. Appl. Phys. 28, 878 (1957).
 - A4 W.H. Ko, IRE Trans. on El. Dev., ED 8, 123 (1961).
 - A5 A.S. Grove and C. F. Sah, Solid St. Elec. 7, 107 (1964).
 - A6 L.A. Davidson, Solid St. Elec. 9, 1145 (1966).
 - A7 L. deSmet and R. vanOverstraeten, Solid St. Elec. 18, 557 (1975).
 - A8 D.C. Lewis, Solid St. Elec. 18, 87 (1975).
 - A9 J.L. Moll, S. Krakauer and R. Shen, Proc. IRE 50, 43 (1962).
 - A10 S.Y. Muto and S. Wang, IRE Trans. on El. Dev., ED 9, 183 (1962).
 - A11 J.L. Moll and S.A. Hamilton, Proc. IEEE 57, 1250 (1969).
 - A12 D.P. Kennedy, IRE Trans. on El. Dev., ED 9, 174 (1962).
 - A13 H.J. Kuno, IEEE Trans. on El. Dev., ED 11, 8 (1964).
 - A14 R.H. Dean and C.J. Nuese, IEEE Trans. on El. Dev., ED 18, 151 (1971).

14. J. L. Schmit and E. L. Stelzer, J. Electronic Mater. 7, 65 (1978).
15. J.D. Beck, R.M. Broudy, and R.W. Bechdolt, "Metal-Insulator-Semiconductor Results in 3 to 5 Micrometer (Hg, Cd) Te," Proc. IRIS Detector Specialty Group Meeting, 1977.
16. R.W. Bechdolt, "A Metal-Insulator-Semiconductor Study of the Bulk and Surface Properties of (Hg, Cd)Te," Master's Thesis, Department of Electrical Engineering and Computer Science, Massachusetts Institute of Technology, May, 1977.
17. J.D. Beck and R.W. Bechdolt, "Exploratory Development of (Hg, Cd)Te: Trapping and Surface Processing," First Interim Technical Report, AFML Contract F33615-76-C-5070, January-October 1976.
18. Coppertech, Inc., 9th and Greenleaf St., Allentown, PA 18102.
19. E. H. Putley, The Hall Effect and Related Phenomena, Butterworths, London (1960).
20. J. L. Schmit, J. Appl. Phys. 41, 2876 (1970).
21. E. L. Stelzer and J. L. Schmit, "Exploratory Development on $\text{Hg}_{1-x}\text{Cd}_x$ Te Improvement, Phase II," Interim Report under F33615-74-C-5041, January 1975.
22. J.C. Woolley and B. Ray, J. Phys. Chem. Solids 13, 151 (1960).
23. R.R. Galazka, Acta Phys. Polon. 24, 791 (1963).
24. J. Blair and R. Newnham, Conference on the Metallurgy at Elemental and Compound Semiconductors, Boston, 1960, Interscience, New York p. 393 (1961).
25. D. Long and J. L. Schmit, Semiconductors and Semimetals, Vol. 5, Chap. 5, Academic Press, New York, p. 243, (1970).
26. J. L. Schmit and E. L. Stelzer, J. Appl. Phys. 40, 4865 (1969).
27. "FREON" E5, Fluorinated Ether, E.I. Dupont Co., Wilmington DE 19898.
28. R.H. Kingston, Proc. IRE 42, 829 (1954).
29. B. Lax and S.F. Neustadter, J. Appl. Phys. 25, 1148 (1954).
30. H.J. Kuno, IEEE Trans. on Electron Dev., ED11, 8 (1964).